Numerical approaches to investigate small bodies' properties in their structure and surface with case studies

by

Yaeji Kim

A dissertation submitted to the Graduate Faculty of
Auburn University
in partial fulfillment of the
requirements for the Degree of
Doctor of Philosophy

Auburn, Alabama
May 6, 2023

Keywords: Planetary science, Small bodies, Asteroids, Kuiper Belt objects, Numerical simulation, Surface, Interior, Structure

Approved by

Masatoshi Hirabayashi, Chair, Assistant Professor of Aerospace Engineering
Dennis Bodewits, Associate Professor of Physics
Marina Brozović, Navigational Engineer of Jet Propulsion Laboratory/California Institute of Technology
Davide Guzzetti, Assistant Professor of Aerospace Engineering
Ehsan Taheri, Assistant Professor of Aerospace Engineering

Abstract

Asteroids, comets, and Kuiper-belt objects (aka. Small bodies) can tell us essential information to understand their evolutionary history and advance the history of our solar system. Since the currently available data on small bodies mostly come from ground-based observations and a few space exploration missions, it is a necessary process to infer small bodies' properties based on limited data. In terms of scientific importance, this dissertation mainly focuses on developing numerical models to characterize small bodies' properties on the surface and structure based on their complex dynamics and suggests diverse case studies showing how the numerical models are applied to asteroids and Kuiper-belt objects.

To explain the optical discrepancy between S- and Q-type asteroids, the tidal effect during a close planetary encounter has been considered one of the contributors, but this phenomenon has never been detected. To explore this hypothsis, the numerical model is developed, which can provide the stability of an asteroid's surface condition under the tidal effect. This model is applied to triaxial ellipsoids with different elongations to discuss a potential correlation between asteroids' shape and its surface sensitivity. This study indicates that an asteroid's shape elongation controls surface slope variations, enhanced by rotation, during a planetary encounter, and thus the more elongated shape is easily susceptible to tidal resurfacing. As an advanced project, the actual case of the planetary encounter – (99942) Apophis's 2029 Earth encounter – is explored. The original model is extended to investigate surface grain movement given the tidal effect. The key conclusion here is that Apophis's encounter orientation would be a factor in predicting the certain area showing a strong signal for the tidal resurfacing phenomenon.

For analyzing small bodies' structure conditions, the finite element model (FEM) is implemented with the goal of investigating time-varying stress fields of an irregularly shaped body, given its dynamical state. The FEM is applied to three different small bodies. First, 1998 KY26, a target of the Hayabusa2's extended mission, is tested using the FEM to investigate its strength level given its tiny size (20 – 40 m) and rapid spin period ($\sim$10 mins). The measured

strength level is less than 20 Pa, which indicates that 1998 KY26 is still eligible to sustain the current shape regardless of a monolith structure or a rubble-pile system. The second case study targets (16) Psyche, the largest metal-rich asteroid in the main asteroid belt. Given the assumption that Psyche could have a differentiated structure (the inner iron core with the outer silicate-rich layer), the inverse problem algorithm is designed to constrain its interior layout distribution. The FEM is adopted to determine the pressure regime of the inside of the object with different interior layout distributions. The key results of this study support that Psyche is still eligible to expose the metallic components in crater-like regions via an impact cratering process or experience ferrovolcanism in localized regions. The third case study selects (486958) Arrokoth, which is a cold classic Kuiper Belt Object explored by NASA New Horizon. The question of how the bilobated Arrokoth responded to the structural disturbances generated by the sky crater impact located in the small lobe is examined using the FEM. The original FEM is extended to calculate the time-varying cohesive strength of Arrokoth based on viscoelastic deformation. The maximum strength variation reaches up to a few kilopascals ($\sim$15 kPa), significantly higher than other small bodies. This result indicates that Arrokoth could experience structure disturbances such as a neck breakup in the past, although it is still possible that KBOs might have a higher strength regime than other small bodies. As a final note, these numerical approaches can be extended in variety to target other small bodies and appropriately use mission or observation data to study small bodies further.

Acknowledgments

I want to acknowledge that all the projects described in my dissertation would only be completed successfully with the support of colleagues, my people, and financial funding (NASA/New Frontiers Data Analysis Program, Zonta Amelia Earhart Fellowship, LSSTC Data Science Fellowship Program, and Auburn University).

Above all, I would first like to thank my advisor, Toshi Hirabayashi, for his unconditional support and encouragement that eventually let me go through my Ph.D. journey. I am very impressed by his passion for keeping working hard for research and constantly being curious about diverse topics not only limited to small bodies. His serious attitude as a researcher motivates me to work hard and eventually leads me to think about how I can be a good researcher.

Of course, I sincerely appreciate the support of my outstanding committee members. Although there should be limitations from different time zones and locations, Dr. Marina always keeps responding to me earlier than anyone else so that I could not feel any inconvenience when communicating with her. She always supports my Apophis project, and thus I could successfully complete the first round of this project. I look forward to future beneficial discussions when Apophis passes the Earth in 2029. Additionally, I would like to point out the endless support from Dennis. My second office at Leach Science Center allowed me to refresh myself and refocus on my work whenever I got distracted. Since I will extend my work to the field of comets, I hope to collaborate with Dennis and AMO people sooner during my postdoc. Also, I appreciate the support of other committees from Aerospace Engineering – Dr. Guzzetti and Dr. Taheri. Since our fields are not perfectly matched, all your comments and suggestions on my work let me think about my work from new/different view.

Lastly, I would like to say 'thank you and love you' to my people – STAR lab mates, my friends, and my family. I am sure I could not go through this long journey without your love, friendship, and time spent together. Thank you for being my people.

Table of Contents

List of Figures

List of Tables

Chapter 1

Introduction

Small bodies define small solar system bodies such as asteroids, comets, and Kuiper-belt objects not included in large planetary objects such as the Sun and major planets. They are legacy objects in space, which can tell us essential information to understand their evolutionary history and advance the history of our solar system. In the past, ground observations were the only major data source for small bodies. With the advent of space technology, some space missions have been employed and support acquiring detailed data such as high-resolution images. For a better understanding of small bodies, one essential way is developing a numerical model that properly uses the obtained data from ground observations and space exploration missions. The data can be used to be a piece of input information for the numerical model. Furthermore, the data can also be used for validating the results derived by numerical modeling.

The dissertation mainly focuses on research projects inferring physical properties on the surface and structure of small bodies, and thus the main section of the manuscript has twofold: surface and structure analysis. For surface analysis, we visit a science question on how Earth-crossing objects interact with our planet. When the object closely passes the planet, it is affected by the Earth's gravity field. Theoretically, when the object is under the tidal effect, it can induce the movement of grains on the surface. This phenomenon has never been directly observed in the past, but it has long been considered one of the contributors to resurfacing near-Earth asteroids (NEAs). Especially this effect could be a potential explanation for the spectral discrepancy of NEAs between S- and Q-type asteroids, although they have matching compositions. In Chapter 2, we describe the project on exploring the hypothesis that the tidal

effect during distant planetary encounters causes the fresher surface observed in Q-type asteroids. In Section 2.1, we introduce a fundamental numerical model that computes the tidal effect acting on the surface of asteroids based on the distance of the closest encounter and rotation period and analyzes the stability of the surface condition. In Section 2.2, we adopt the developed numerical model to the real Earth encounter event of (99942) Apophis. The case study of Apophis' 2029 Earth encounter event uses the extended fundamental numerical model to investigate the actual dynamical interactions between Apophis and Earth during the close encounter, and further explore how the measured tidal effect acts on surface grains using the discrete element method [1].

For structure analysis, we develop a numerical model that can provide the cohesive strength level given a targeted object's physical and geophysical properties and conduct case studies to understand the object's evolutionary history using this model. The main numerical tool is developed based on the finite element method, which is used for solving our structural equation given as a second-order differential equation. The Finite Element Model (FEM) computes stress fields of the entire object structure, which is eventually used for determining the cohesive strength level of the small body. We adopt this model to four different target bodies by extending the fundamental model depending on the science question that each targeted body has. We first adopt the FEM to 1998 KY26, which is a target of Hayabusa2's extended mission (Section 3.2). Since 1998 KY26 is a tiny object having a fast spin period, it has long been considered a monolithic structure. Using the FEM, we constrain the minimum cohesive strength required for 1998 KY26 to avoid any structural disruptions and discuss whether it is still possible to be a rubble-pile asteroid. Second, we introduce a project that explores the largest M-type asteroid, (16) Psyche (Section 3.3). The main question about Psyche is where the significant amount of metals on its surface comes from. The answer could be either the internal or external sources of the Psyche. In this case study, we consider the hypothesis that the metal came from the internal source of the Psyche, given that it is a differentiated object (the inner metallic core and the outer silicate crust). Here, the original FEM is extended to infer the internal structure

[1]The Apophis case study is a collaboration work. The discrete element modeling is done by Joe DeMartini from the University of Maryland.

layout of Psyche, and we use the result to discuss whether the measured interior structure layouts are compatible with potential scenarios (i.e., impact cratering and ferrovolcanic surface eruption) to explain the metals observable on the Psyche's surface. At last, we visit the most well-known Kuiper-belt object, (486958) Arrokoth, using the FEM (Section 3.4). The image taken by the New Horizons Long Range Reconnaissance Imager (LORRI) shows that Arrokoth has an extremely contact binary shape (two lobes connected with a narrow area). One noticeable geological feature is that a relatively smaller lobe has the largest crater-like region named 'sky.' Given Arrokoth's bilobated structure and the significant size of the crater, we speculate that Arrokoth might be subject to strong structural disturbances in the past. To explore this question, we extend the original FEM to investigate the time-varying strength of the bilobated Arrokoth after the sky crater impact occurred.

As shown in the conducted research projects, numerical modeling is a crucial method to explore questions we have in planetary science. However, the current numerical models further need to validate the obtained result. In the conclusion section, we propose potential works to support the validation process of the numerical models by connecting the numerical result to observational or mission data.

Chapter 2

Surface analysis

We visit one of the hypotheses in planetary science: can the tidal effect generated by a planetary encounter be a contributor to resurfacing NEAs' surface? To explore this hypothesis, we develop a numerical model that investigates an asteroid's surface slope evolution when it closely passes the terrestrial planet – Earth in this study. We first apply this model to discuss how asteroid elongation affects its surface sensitivity during a planetary encounter (Section 2.1). We then advance this model to study the actual case, Apophis's Earth encounter event in 2029 (Section 2.2).

2.1 Tidal resurfacing of rubble-pile asteroids during a planetary encounter

2.1.1 Research background

S- and Q-type asteroids exhibit the compositional features of ordinary chondrites, while their spectral slope and absorption band are slightly different. S-type asteroids have steeper spectral slopes, weaker absorption bands near wavelengths between 1 μm and 2 μm, and lower albedos than Q-type asteroids [10, 11, 12, 13]. Space weathering driven by ion implantation and micrometeorite bombardments cause optical variations in material compositions [11, 14]. For S- and Q-type asteroids, space weathering is considered to redden their surface materials. The timescale of space weathering may range between 10 ka and 1 Ma in the inner Solar System [15, 16]. For near-Earth asteroids (NEAs), the dynamical lifetime is 2 Ma [17] and thus longer than the space weathering timescale. Without additional processes, Q-type asteroids should be

altered to S-type asteroids and depleted continuously. However, this contradicts the high fraction of Q-type asteroids among NEAs ($\sim 25\%$). One possible hypothesis is that redder S-type asteroids are resurfaced to become bluer Q-type asteroids [e.g., [10, 18])].

Possible resurfacing mechanisms include 1) planetary encounters with terrestrial planets [10, 19, 20, 21, 22, 18], 2) thermal fatigue by cyclic diurnal temperature variations [23, 24, 25], and 3) rotational instability driven by the Yarkovsky-O'Keefe-Radzievskii-Paddack (YORP) effect [26]. Among these mechanisms, the tidal effect may be a critical driver that resurfaces rubble-pile asteroids. The distribution of Q-type asteroids correlates with the perihelion distance and the minimum orbit intersection distance, suggesting that encounters with massive planets may resurface asteroids enough to change their surface spectral properties [10, 21, 18]. [18] proposed that Q-type asteroids may be resurfaced if the close encounter is within ~ 5 planetary radii, thus outside the Roche limit (~ 3.4 planetary radii for an asteroid with a bulk density of 2.0 g cm^{-3}). These studies statistically showed that the resurfacing process of S-type asteroids is possibly related to their distant planetary encounters. However, the resurfacing mechanism is still not well understood.

Numerical studies have been reported for investigations of the tidal effects on rubble-pile asteroids during planetary encounters. They are in general divided in two categories; catastrophic, where an object is destroyed by the tides, and non-catastrophic, where either shape or surface or both are altered. For catastrophic disruptions, research has shown how small bodies that closely encounter planetary bodies are broken up due to strong tidal forces. The breakup conditions depend on small bodies' mechanical strength, material compositions, and orbital parameters (e.g, [27, 28, 29, 30]). In 1994, comet Shoemaker-Levy 9 encountered Jupiter and was broken into approximately 20 similar-sized fragments [31]. [32] and [33] modeled this event to better quantify catastrophic disruption processes during close tidal encounters.

Tidal processes during distant encounters outside the Roche limit have also been studied in the literature. [34, 35] applied the theory of hill slope stability to evaluate the stability of asteroid regolith during the distant planetary flyby. They had two conclusions: rapidly rotating asteroids are highly likely to experience resurfacing, and the resurfacing process on asteroids may occur at larger flyby distance ($\sim$10 Earth Radii) than the previous estimation ($\sim$5 Earth

Radii). In this paper, we extend their works to gain a more comprehensive understanding of resurfacing by adding an element that had not been discussed in the earlier works: an asteroid's elongation. We finally note that studies have shown limited changes in the shape and surface conditions of Apophis, which is going to closely flyby the Earth within 6 Earth radii [36, 37, 38]. Our study will give further insight into the mechanism of mild tidal effects on a rubble-pile asteroid during a distant planetary encounter, which may be a critical source of Q-type asteroids.

In this study, we investigate the influence of a rubble-pile asteroid's elongation on surface sensitivity to tidal effects when it approaches the Earth outside the Roche limit by parameterizing the elongation with different planetary encounter conditions. We first demonstrate the resurfacing mechanism by considering the surface slope and its variation in Section 2.1.1.1. Our investigation and simulation settings are described in Sections 2.1.2 and 2.1.3.1. In Section 2.1.3.2, the results of all conducted simulations are presented. We discuss our findings, potential issues of the current numerical model, and future work in Section 2.1.4.

2.1.1.1 Resurfacing mechanism during a distant planetary encounter

Resurfacing processes remove a space-weathered, redder surface layer on S-type asteroids by exposing fresh materials beneath it. In situ observations by spacecraft revealed that the space weathered layer is likely very thin and correlated with the surface topography. Despite limited knowledge of space weathering on S-type asteroids, the sampled particles from NEA (25143) Itokawa suggested that the weathered thickness is only ~ 80 nm [39, 40], indicating that only a very-thin top surface layer had been affected by space weathering. We thus speculate that even mass movements at a tiny scale can induce color variations in top surfaces. Furthermore, [41, 42] reported on bluer, likely unweathered regions around the pole regions and the equatorial ridges of NEA (162171) Ryugu (C-type asteroid), although the space weathering mechanism may be different from that on S- and Q-type asteroids [43].

We use two geophysical parameters to describe the surface sensitivity to possible granular flows: the surface slope and its variation. The surface slope describes how the surface element is tilted from the direction of its total acceleration combined with local gravity, the tidal effect,

and the rotational effect on each surface element. The slope variation shows how the surface is affected by time-varying acceleration during the encounter. Using these parameters, we estimate the locations of where granular flows can occur. When the surface slope reaches its critical slope, i.e., the angle of repose, which is 35° for a typical geological material without cohesion [44], granular flows may start to occur [45, 46]. Furthermore, if the slope variation is high enough to cause surface mobility, granular flows may occur for sub-critical slopes. [47] showed this mechanism operating on the surface of the Martian moon Phobos, leading to the resurfacing process; however, this mechanism may not be proper for the planetary encounter resurfacing because it is a non-periodic event. In our analysis, we use the slope variation to see how sensitive surfaces become during the distant planetary encounter.

Mass movements in and on asteroids may be influenced by many different elements. Electrostatic forces may induce mass mobility [48]. Particle ejection may also occur by thermal fatigue [49]. Impact cratering can excavate fresh materials. Granular convection such as the Brazil-nut effect can transport fresh materials from the interior [50, 51]. Seismic wave propagation may enhance resurfacing [52, 53]. The consideration of these effects on mass movements is beyond our scope. Instead, we focus on surface flows driven by the tidal force, as well as the gravitational force and the centrifugal force to better understand how an asteroid's elongation affects the tidally induced resurfacing mechanism.

2.1.2 Modeling

Our model computes the surface slope (θ) by using the following equation,

$$\theta = \arccos\left(\frac{-\vec{n_f}\cdot\vec{a_g}}{\|\vec{n}\|\|\vec{a_g}\|}\right). \tag{2.1}$$

where $\vec{a_g}$ is the net acceleration vector, and $\vec{n_f}$ is a normal vector to a surface element. A schematic diagram visualizing $\vec{a_g}$ is shown in Figure 2.2. The surface slope variation ($\delta\theta$) is the angle difference of a given element between the maximum surface slope during the flyby and the initial slope before the flyby. This quantity was used to analyze resurfacing on the martian moon, Phobos [47].

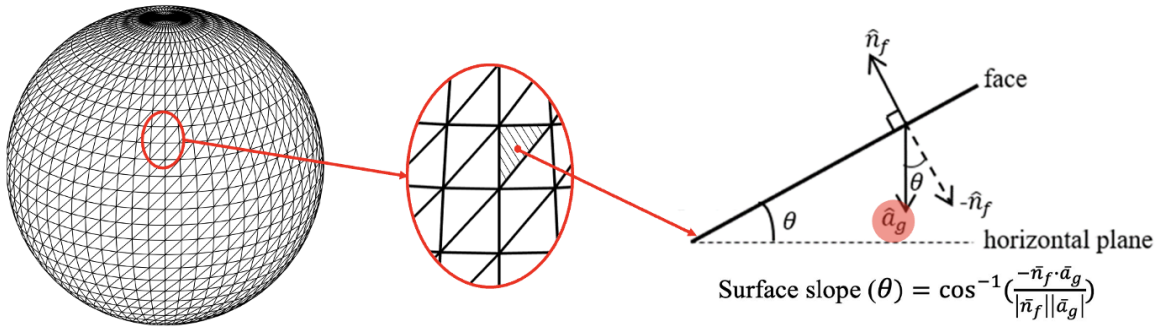

Figure 2.1: A schematic diagram showing how to define a surface slope given $\vec{n_f}$ and $\vec{a_g}$. Here, the left-side panel is a surface mesh representing an asteroid. The middle-side panel shows the zoomed part of the mesh, while the right-side panel depicts the surface slope. As shown in the schematic, the Surface slope on Apophis is determined as the angle between the normal direction of a facet and the direction of the total force acting on the facet. A schematic showing $\vec{a_g}$ is described in Figure 2.2.

Next, we discuss the net acceleration vector, $\vec{a_g}$, during a planetary encounter. Since we focus on the onset of the grain motion on an asteroid surface, particles are assumed to rest initially. The assumption yields $\dot{\vec{r}} = 0$ and thus excludes the Coriolis effect. This setting may provide a conservative condition for the occurrence of resurfacing. $\vec{a_g}$ is given as

$$\vec{a}_g = -G\rho_A \int_{V_A} \frac{\vec{r}}{r^3} dV_A - \frac{GM_E}{{R_c}^3}(\vec{r} - \frac{3(\vec{R}_c + \vec{r}) \cdot \vec{r}}{R_c^2}\vec{R}_c) - \dot{\vec{\omega}} \times \vec{r} - \vec{\omega} \times (\vec{\omega} \times \vec{r}). \tag{2.2}$$

In this equation, G is the gravitational constant, ρ_A is the asteroid's bulk density, V_A is the asteroid's volume, $\vec{r}$ is the position of a surface element relative to the center of mass (COM) of the asteroid, M_E is the mass of the planet, $\vec{R_c}$ is the position of the COM of the asteroid relative to that of the planet, $\vec{\omega}$ is the asteroid's angular velocity vector, and $\dot{\vec{\omega}}$ is the asteroid's angular acceleration vector. The first term is the acceleration by self-gravity, the second term describes the tidal acceleration, and the third and fourth terms represent the rotational effect. For self-gravity, we use an elliptical integral for computing the gravity field around a biaxial ellipsoid [54].

For the rotational motion, we solve the following equation:

$$[I]\dot{\vec{\omega}} + \vec{\omega} \times [I]\vec{\omega} = \frac{3GM_E}{R_c^5}\vec{R}_c \times [I]\vec{R}_c. \tag{2.3}$$

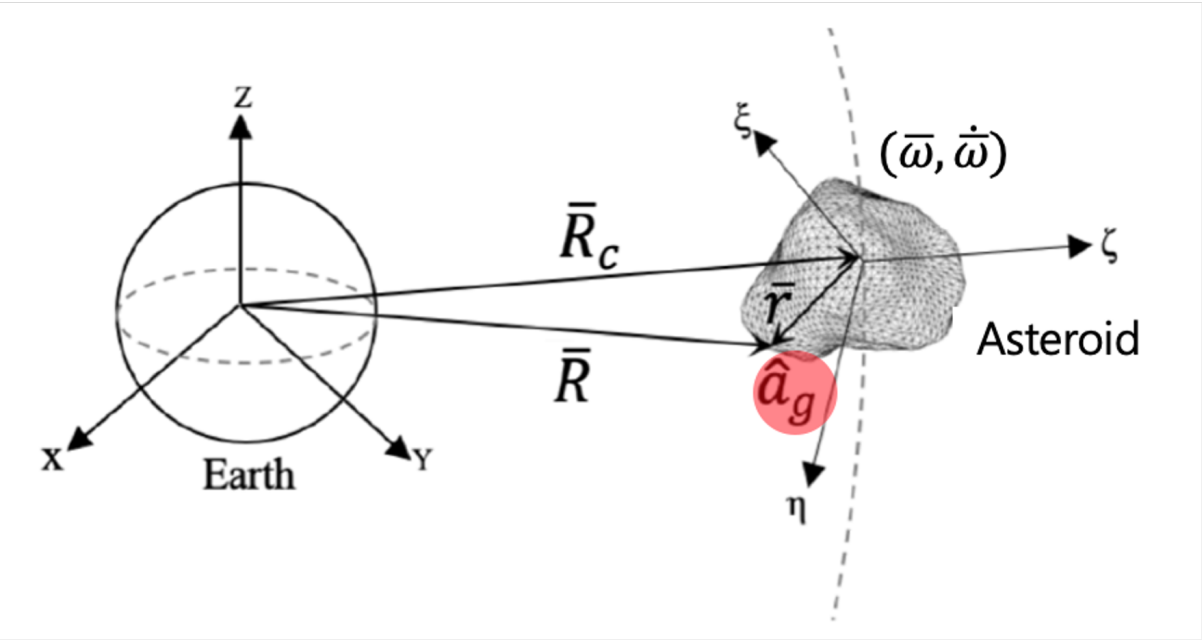

Figure 2.2: A schematic diagram showing the close Earth flyby. The Earth and asteroid are represented as a sphere and an irregular rigid body, respectively. The frame [X, Y, Z] defines the reference frame, while the frame $[\eta, \zeta, \xi]$ represents the rotating frame fixed to the asteroid body. Here, $\vec{a_g}$ is the net acceleration vector computed as a combination of self-gravity, tidal acceleration, and rotational effect. Other symbols are defined in Section 2.1.2.

where $[I]$ is the moment of inertia matrix and computed by [55]. We also note the changes in the asteroid's orientation during the encounter. The transformation matrix, $[A]$, is given as

$$[\dot{A}] = -[\tilde{\omega}][A]. \tag{2.4}$$

The initial condition of [A] is fixed as an identity matrix. The evolution of [A] is eventually used to convert $\vec{R_c}$, which is a vector in the planet-centered inertia reference frame, to the one in the body-fixed frame in Equation (2.1.2). Here, $[\tilde{\omega}]$ is the skew matrix of $\vec{\omega}$, which is given as

$$\tilde{\omega} = \begin{bmatrix} 0 & -\omega_3 & \omega_2 \\ \omega_3 & 0 & -\omega_1 \\ -\omega_2 & \omega_1 & 0 \end{bmatrix} \tag{2.5}$$

We use a Runge-Kutta 4th order integrator with a constant time-step to propagate $\vec{\omega}$ and $[A]$ over a considered time frame. $\vec{R_c}$ is described in the body-fixed frame centered at the

COM of the planetary body, where the axes are aligned with the asteroid's moment of inertia axes. To determine $\vec{R}_c$, we design a hyperbolic trajectory with a given periapsis and a constant encounter velocity and obtain a list of $\vec{R}_c$ within a considered time span with a proper time step (see Section 2.1.3.1). This list is incorporated into the integrator that solves Equations (2.1.2) and (2.1.2) to describe the rotational motion. At last, all computed parameters are applied to Equation (2.1.2) to obtain $\vec{a}_g$ of each element on the asteroid. We developed a MATLAB program package for this simulation process.

2.1.3 Preliminary results using the tidal resurfacing model

2.1.3.1 Simulation settings

Table 2.1: Physical parameters and shape model information used in our simulations.

Parameter	Values
Earth-like planet mass (M_E)	$5.97 \times 10^{24}\ kg$
Asteroid's volume (V_A)	$1.98 \times 10^{7}\ m^3$
Asteroid's bulk density (ρ_A)	$2.0\ g\ cm^{-3}$
Simulation length	$\leq 20\ EarthRadii$
Simulation time step	$5\ sec$
Encounter speed	$15\ km\ s^{-1}$
Angle of repose of top surface layers	35°
Number of facets	10440
Mean facet size	$35\ m^3$ ($\sim$0.01% of the entire surface)

We focus on the slope variation on uniformly rotating biaxial ellipsoids with different aspect ratios (AR). Here, AR is defined as a ratio of the major axis to the minor axis. The volume of the shape models is set identical to that of a sphere having an equivalent diameter of 340 m, which is a typical size of rubble pile asteroids. A bulk density is assumed to be a constant value of 2.0 g cm^{-3}, which is consistent with that of Itokawa (S-type) [56]. In each hyperbolic trajectory, the initial and final points of a test asteroid are 20 Earth-like planet radii ($\sim$6371 km for one Earth-like planet radius) away from the planet center, and thus the tidal effect is negligible at those points. The encounter speed is set to 15 km s^{-1} for all the cases [57], while we consider three hyperbolic trajectories with different periapses in the range of plausible resurfacing distances (3.5, 5, and 10 planet radii) [34]. The total length of simulation

is approximately 4.5 hours with a time step of 5 seconds. In all test cases, the body is set to rotate along their maximum moment of inertia axes, and its spin axis is perpendicular to the orbital plane. The angle of the repose is set to be 35°.

2.1.3.2 Results

We introduce the nomenclature used in this session. To characterize the area affected by high slope variation ($\delta\theta$), we introduce two characteristic regions: Regions I and II. Region I is an area whose surface slope is higher than the angle of repose of 35° before the encounter. Region II, on the other hand, is an area that has the slope exceeding the angle of repose during the encounter. We also use the area difference between Regions I and II to indicate the surface regions that reach above the angle of repose due to the tidal effect. A total of 33 simulations are performed to analyze how $\delta\theta$ is affected by the asteroid elongation during distant encounters.

We consider three cases of the spin periods, 1.5, 2.8, and 3.1 hr. These spin periods are selected to demonstrate high $\delta\theta$ variations around the spin barrier, where gravitational aggregates may fall apart if they do not have tensile strength [58]. Given the spin periods defined, the test body may have high slopes even before a tidal encounter (i.e., Region I) in some cases. The 1.5 hr spin period case causes all the AR cases to have Region I across the entire surface. Highly elongated shapes with lower ARs have Region I at even longer spin periods. At a spin period of 2.8 hr (see Figure 2.3), shapes with $AR = 0.8$ and $AR = 0.57$ have Region I at middle latitudes around the longest axis. At a spin period of 3.1 hr, the $AR = 0.57$ shape still has Region I, which would be sensitive to granular flow. We emphasize that the reason for this selection is to illustrate the mechanisms of the slope variation due to the elongation and show its transition around the spin barrier. Thus, these conditions allow for visualizing how shape elongation controls surface slope variations, enhanced by rotation, during a distant encounter.

To show how the elongation affects $\delta\theta$, Figure 2.3 illustrates sample cases in which asteroids with ARs of 1.0, 0.8, and 0.57 reach 5 Earth radii with a spin period of 2.8 hr. The results show that $\delta\theta$ becomes higher as AR is lower. When the asteroid has $AR = 1$, high $\delta\theta$ occurs at a latitude of $\sim$18 deg. The high $\delta\theta$ regions always face the planet because of its axisymmetric

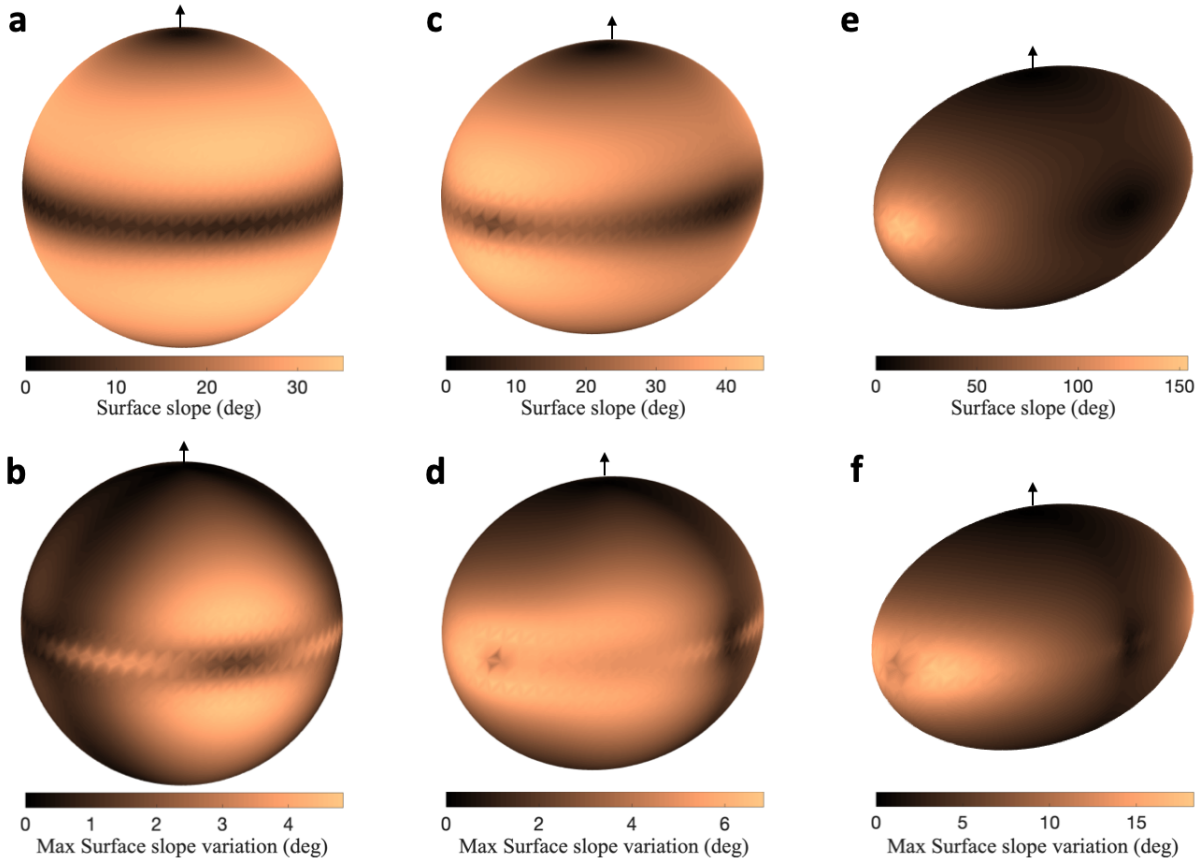

Figure 2.3: Maximum surface slope and slope variations for each shape. The top panels (a, c, and e) show the surface slopes, which are affected by the tidal effect, during the planetary encounter with the periapsis of 5 Earth radii and the spin period of 2.8 hr. The bottom panels (b, d, and f) illustrate the maximum surface slope variation during this encounter. The aspect ratio of each column is 1, 0.8, and 0.57, respectively. All plots are projected from a longitude of 130° and a latitude of 15°. The black arrows denote the spin axes.

shape. When $AR = 0.8$, high $\delta\theta$ regions tend to be distributed widely around the edges along the longest axis. When $AR = 0.57$, higher $\delta\theta$ concentrates on the edges.

Table 2.2 shows the results of the cases simulations. We first discuss the cases of 1.5 hr and 3.1 hr. When the spin period is 1.5 hr, since the centrifugal force is already dominant, Region I spreads over the almost entire regions for any shapes. This extreme condition does not cause the slope to change significantly. When the spin period is 3.1 hr, self-gravity starts to be dominant, and tidal acceleration does not influence the slope variation remarkably. The $AR = 0.57$ case still shows non-zero area difference between Region II and Region I at the asteroid's edge along the longest axis, where self-gravitational acceleration and rotational acceleration are comparable.

When the spin period is 2.8 hr, rotational acceleration becomes comparable to self gravitational acceleration while some locations on elongated shapes may still be dominantly influenced by centrifugal forces. We show more simulation cases for this spin period case in Table 2.2, compared to other spin periods, to examine the slope variation depending on the elongation. Region II becomes wider than Region I, strongly depending on the elongation. With the decrease of AR, the area difference between Region II and Region I (see the Increase Rate in Table 2.2) increases in the range of AR from 1 to $\sim$0.8 but decreases from $\sim$0.8 to 0.57. Consider when the periapsis is 3.5 Earth radii. For $AR = 1$, Region II is $\sim$23% broader than Region I. The area difference becomes $\sim$37% for $AR = 0.8$ and then gradually decreases to $\sim$30% for $AR = 0.57$, which is still higher than the spherical case. This similar trend is observed when the periapsis is 5 and 10 planet radii. The decrease of the area difference from $AR = 0.8$ to $AR = 0.57$ results from the fact that a more elongated shape has a limited region in which a high slope variation occurs because of its narrower edge. As the periapsis becomes distant, tidal acceleration becomes smaller, leading to the decrease of the slope variation.

Our results are consistent with [34, 35, 38] in terms of the influence of the spin period and orbit on $\delta\theta$. Importantly, we newly address how the elongation impacts the slope variation during distant encounters. If the shape is moderately elongated, broader areas may have reasonable slope variations, which may cause the surface slope to reach the angle of repose. If the shape is highly elongated, the slope variation becomes higher although the affected area may be limited. While our parameter analysis is still coarse, the 2.8 hr case implies that $AR = 0.8$ has the most noticeable change between Regions II and I because the total acceleration of rotation and self-gravity becomes small across the broader regions, the tidal acceleration can easily change their slope conditions.

2.1.4 Discussion

We numerically showed how the shape elongation affects the slope variations and the location of sensitive regions during distant encounters. We observed two critical features. First, the shape elongation enhances the slope variation. High slope variations are observed when the shape is elongated. When an asteroid spins at a spin period at which centrifugal and gravity

acceleration are comparable, tidal acceleration can dramatically change the surface slope. Thus, an elongated body tends to be more exposed to such a dramatic change. Second, the increase of the area whose surface slope exceeds 35° during a distant encounter (Region II - Region I) depends on shape elongation. As the shape is more elongated from the spherical condition, the area that reaches the angle of repose of 35° increases. However, after the shape reaches a certain elongation (in our simulation, it was $\sim$0.8), the area difference, Region II - Region I, starts decreasing due to the limited area of high slope variations. This trend is reasonable because the slope condition on a highly elongated body is clearly separated into gravitational and centrifugal acceleration-dominant regions along the longest axis, causing "fewer" areas to have high slope variations. From these two trends, we conclude that elongation is a strong contributor to the surface slope variation during a distant encounter.

The shape elongation of NEAs has been reported by observational investigations. The statistical characterizations of light-curve amplitudes by [59] showed that the shape elongation of NEAs may be between 0.6 and 0.8 if the objects are assumed to be a population of prolate spheroids. Furthermore, there is an apparent excess of fast rotators in the NEAs with D $>$ 200 m near the spin barrier. Our study implies that if the fast spinning asteroids experience distant encounters, high slope variations may occur, and their elongation may control the affected area. This interpretation is consistent with the arguments of earlier works [e.g., [35]], and we emphasize that our study newly analyzes the influence of the elongation on slope variations.

We point out potential issues with our current numerical model. First, this model does not take into account cohesion, which may prevent resurfacing at fast spin but enhance its magnitude if resurfacing occurs. However, the surface slope without cohesion is still a meaningful parameter based on recent observations [e.g., [41, 47, 56, 60]] that thin top-surface layers of an asteroid may be covered with weak, cohesionless materials. Second, the shape of an asteroid is assumed to be rigid in our model; in other words, its deformation is ignored. If deformation occurs, the location of resurfaced regions and the magnitude of resurfacing are likely to change due to the variation of $[I]$ and $\vec{r}$. Third, in the performed simulations, we did not parameterize the asteroid's spin orientation. Depending the direction of the spin axis, the tidal effect may affect the rotational motion differently [61], causing variations in surface acceleration. Thus,

the slope distribution may evolve differently due to the rotational conditions during distant encounters. Fourth, we only considered biaxial ellipsoids for our asteroid shapes, which only represent an approximate subset of true shapes of NEAs. Lastly, this study only estimated incipient conditions when surface regolith could be set in motion but did not give the magnitude of the surface mobility. We leave these issues as critical elements to be solved in future work.

2.2 Case study: (99942) Apophis

2.2.1 Research background

(99942) Apophis is a potentially hazardous asteroid that will pass the Earth within a perigee distance of 5.96 Earth radii on 2029 April 13[1]. The 2029 Apophis-Earth encounter event is considered a golden opportunity to directly observe how Earth-crossing objects interact with the Earth's gravity field, offering a natural experiment which could allows us to better understand potentially hazardous objects and support the science of planetary defense [62]. As a result of the unique opportunities for science that this object's passage provides, NASA has recently announced that Apophis has been selected as the target of the OSIRIS-REx extended mission—OSIRIS-APEX [63].

The perigee distance of Apophis from Earth during the 2029 close encounter is outside the canonical Roche limit ($\sim$3.4 Earth radii, given a bulk density of $\sim$2 g cm^{-3} for an Sq-type asteroid like Itokawa [64]) that induces catastrophic disruptions of unconsolidated material [28, 65]. Note that Apophis is intermediate between S- and Q-type asteroids [66]. During the 2029 Earth encounter, Apophis will have a definite change in its orbit and rotational properties in response to Earth's tidal torques [37, 67, 68, 69, 36, 70]. These orbital and rotational changes will likely occur with magnitudes sufficient to be detectable by ground-based telescopes. Furthermore, we anticipate that the perigee distance of 5.96 Earth radii may be close enough to subject Apophis to some influences from Earth's tidal forces: surface refreshing [38, 71], small-scale structure modifications and seismic vibrations [36], and stress variation around Apophis's concave

[1]The perigee distance is the minimum possible close-approach distance between the 3-sigma Earth target-plane error ellipse and the Earth's surface, retrieved from the Center for Near-Earth Object Studies server (`https://cneos.jpl.nasa.gov/ca/`).

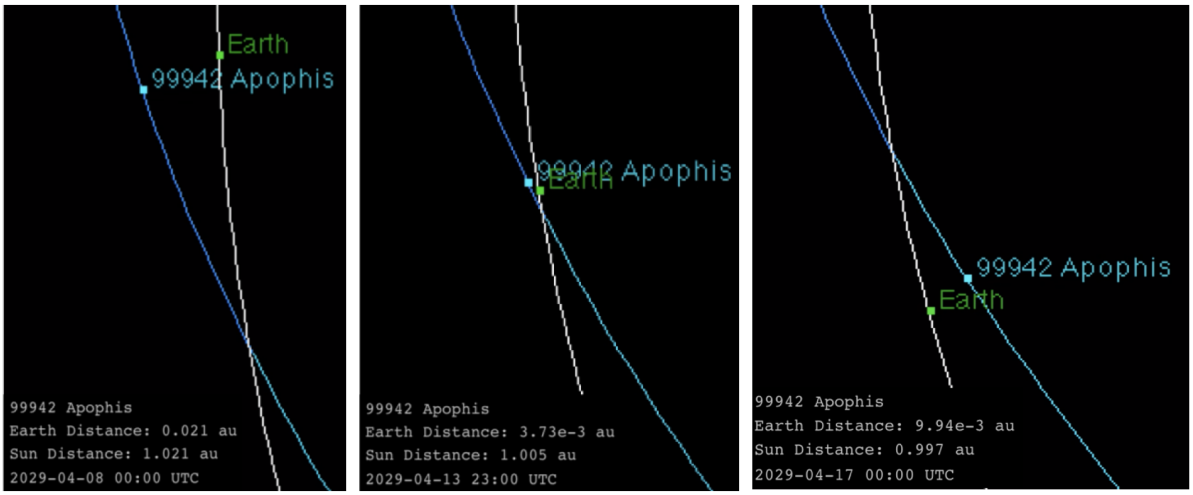

Figure 2.4: The time sequence screenshots of Apophis's nine-day trajectory during the 2029 flyby. The screenshots are retrieved from the orbital diagram archived in the JPL Horizons online solar system data (https://ssd.jpl.nasa.gov/horizons/). The closest distance between Earth's and Apophis's center of mass will be 5.96 Earth radii.

region [72]. Among the potential consequences of the tidal encounter, we particularly note surface refreshing, which may be detectable during the 2029 Apophis-Earth encounter and which is the primary focus of this study.

In general, asteroid surfaces are affected by the competing processes of space weathering and mechanical resurfacing, creating variations in their surface colors. Space weathering reddens or darkens surface materials as a result of solar wind irradiation or micrometeorite impacts, and has been commonly observed in S-type asteroids [12, 14, 73, 74]. Resurfacing is an opposing mechanism that exposes fresh materials beneath the weathered asteroid surface. The interplay between weathering and resurfacing resulting in a variegated surface can be seen on the S-type asteroid Itokawa [56, 75, 76] and the Martian moon Phobos [77, 47], which appear to have dark/redder surfaces with some bright/bluer regions. Although there are other potential mechanisms (e.g., thermal fatigue [23], YORP (Yarkovsky–O'Keefe–Radzievskii–Paddack) spin-up [26], and impact-induced seismic shaking [78]), surface refreshing as a result of planetary encounters is one possible contributor to the inferred resurfacing in near-Earth asteroids (NEAs).

In the taxonomic classification of NEAs, S- and Q-types show different absorption features and spectral slopes [79, 11] although both represent the same compositions as ordinary chondrites. S-types show more reddened surfaces indicative of space weathering, while Q-types have bluer surfaces indicating relatively fresh surface materials. To resolve this inconsistency, [22] suggest that the relatively unweathered surfaces of Q-types result from surface regolith motion during tidal encounters. Many subsequent studies (e.g., [21, 10, 18, 20]) support this hypothesis by statistically showing that the distribution of Q-type asteroid orbital parameters correlates with low perihelion distances and low minimum orbit intersection distances (MOID) with the terrestrial planets Earth, Mars, and Venus; [21] found that Q-types have lower perihelion distances than S-types using a data set of spectroscopic observations of NEAs and Mars-crossing asteroids. [10] used a sample of 95 Earth- and Mars-crossing asteroids (including 20 Q-types) and revealed that Q-types more frequently experienced an Earth encounter with a limiting distance inside $\sim$15 Earth radii in the past few hundred thousand years. [20] then used a larger data set of NEAs (including 64 Q-types) and identified that all sampled Q-types have low MOID values allowing either Earth or Mars encounters. A plausible mechanism for planetary encounters resurfacing weathered asteroid exteriors is that the tidal forces on the surfaces during the encounters fluidize the surface regolith, causing granular flows (i.e., landslides), which can move weathered materials and expose fresher subsurface materials. Based on this mechanism, [34] implemented a resurfacing model that evaluates the stability of asteroid regolith during distant planetary flybys using the theory of hillslope stability. The study set two free parameters, spin period and periapsis, and found that rapidly rotating asteroids are more likely to have surface conditions susceptible to resurfacing and that the limiting distance of resurfacing is less than 10 planetary radii. The asteroid was modeled as a triaxial ellipsoid with an arbitrarily defined density and a friction angle of 45°. [80] extended this work to investigate how an asteroid's shape affects resurfacing and found that a more elongated shape tends to have unstable surface conditions to granular flows during a distant planetary encounter. All previous work has investigated tidal resurfacing from theoretical considerations; however, a direct observation of this phenomenon has never been made. The 2029 Apophis-Earth close encounter could mark the first observations that provide evidence of tidal resurfacing.

In this study, we visit the scientific question of whether tidal resurfacing will occur on Apophis's surface during its close Earth encounter. We use a tidal resurfacing model, which is a joint approach of dynamics [80] and discrete-element method (DEM) modeling [38, 36] to numerically investigate the motion of surface grains driven by the tidal forces on Apophis during the Earth encounter. The dynamics model determines time-varying accelerations felt by each surface patch on Apophis, and the DEM model tracks the specific motion of grains on the given surface patch in the dynamical state. The results of this study could support an investigation of albedo changes after the Apophis close encounter or identify regions of interest to look for evidence of surface grain motion for potential missions to Apophis, including OSIRIS-APEX. Furthermore, understanding the tidal resurfacing processes on Apophis may provide key information about how resurfacing counteracts the expected space weathering timescale on small bodies, and could thus help resolve the long-standing puzzle of the spectral difference of NEAs between S- and Q-types despite their matching compositions [81, 79].

This section for the case study is organized as follows. In Section 2.2.2, we describe the tidal resurfacing model in detail by splitting it into two parts: dynamics and DEM modeling. Section 2.2.3 then shows our simulation results using the tidal resurfacing model. In Section 2.2.4, we discuss the key findings to support potential ground-based observations and in-situ missions for the upcoming 2029 Apophis-Earth encounter event. Lastly, we summarize our conclusions, list areas of uncertainty in the current tidal resurfacing model, and suggest future work in Section 2.2.5.

2.2.2 Advanced tidal resurfacing model

We introduce a numerical model (hereafter 'tidal resurfacing model') used for investigating surface grain motions driven by Earth-induced tides during Apophis's 2029 Earth flyby. In the following subsections, we split the numerical approach into two parts: dynamics and DEM modeling. The dynamics model simulates the orbital and spin evolution of Apophis during a period spanning 3 h before to 3 h after the closest encounter with Earth. By considering the local topographic features, the dynamics model converts the acceleration data into surface slope profiles, including an initial surface slope and slope variation, and then hands off the

time-varying accelerations acting on each surface facet during the encounter to use in the DEM models. For the second stage of the simulations, we use DEM modeling to track the specific motion of grains on surface patches. We apply the time-varying acceleration data derived from the dynamics model uniformly across a number of surface patches filled with discrete regolith particles. The grain motion that we see from the discrete modeling forms the basis of our resurfacing analysis, detailed in Section 2.2.3.

2.2.2.1 Dynamics model

To investigate tidal refreshing during the Apophis-Earth close encounter, our dynamics model computes the acceleration vectors acting on surface facets of Apophis at each time step. We use the radar-derived, concave polyhedral shape model, consisting of 3,996 facets and 2000 vertices, by [1] (see Figure 2.5). This model was derived using the radar observations during the 2012–2013 apparition at Goldstone radar telescope facility in California (aka. Goldstone) in addition to the pre-existing lightcurve-derived convex shape by [82]. The current shape model still has some uncertainties, which are unlikely to be improved by using the recently obtained 2020–2021 apparition data [83], but indicates that Apophis may likely be a contact binary. The net surface acceleration on each surface patch can be computed as the combination of self-gravity, tidal, and rotational accelerations. The detailed equations and propagation for each term are described in Section 2.1.2. We consider a time span of 6 h: 3 h before to 3 h after the closest Earth encounter, when the tidal effects are sufficient to induce variations in the total acceleration, including the fixed self-gravity and rotational accelerations. Outside of this time span, the tides are unlikely to induce any significant force variations because the distance of Apophis from the Earth's center, which exceeds 10 Earth radii, is far enough to neglect the tidal effect. We retrieve Apophis's trajectory using the JPL/NAIF SPICE tool [84, 85] for the 6 h encounter with a timestep of 0.1 s. As a final note, Apophis is a tumbling object undergoing short-axis-mode non-principal-axis rotation. Given the slow spin period of 30.6 h [82, 1] and the short (6 h) time span considered in our simulations for tidal resurfacing, the effect resulting from the tumbling motion of the body is likely negligible in the acceleration variation. Thus we propagate the rotation term assuming Apophis is in the simpler principal-axis rotation mode.

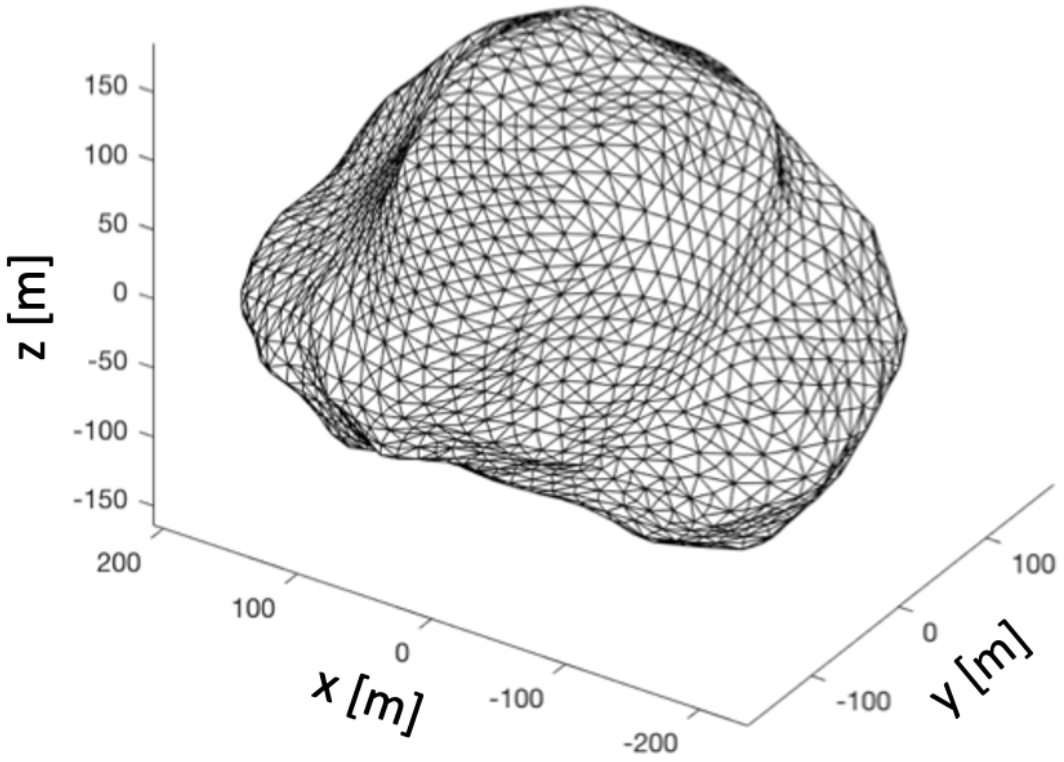

Figure 2.5: Apophis radar-derived shape model [1]. This surface mesh consists of 3,996 facets and 2000 vertices.

As a next step, we convert the generated surface acceleration data into surface slope profile data that includes the initial surface slopes and slope variations for all of the facets on the shape model. We output the total surface acceleration vector for each patch at 60 s intervals to use in the DEM modeling (see Sec. 2.2.2.2.1). Figure 2.6 shows a screenshot of the simulation using the dynamics model simulation. We later combine the surface slope profile data with the measured grain motions in an equivalent surface patch in DEM simulations to gain insight into motions across the entire surface (see Sec. 2.2.3). The surface slope is defined as the angle between the normal direction of the surface facet and the corresponding surface acceleration vector accounting for self-gravity plus any other accelerations under consideration, such as those due to rotation and tides. The slope variation is computed by subtracting the initial surface slope from the surface slope at a given time during the simulation, and thus can take on positive or negative values. Figure 2.7 defines 2 cases with positive and negative slope variations from facets with the same initial surface slope. Depending on where a nearby planetary body (here, Earth) is located, the additional force from the tidal effect can increase the slope (Fig. 2.7 (a)) or decrease it (Fig. 2.7 (b)). The left panels of Fig. 2.8 show examples of the surface slope evolution over time in our models, corresponding to positive (upper left) or negative (lower left) slope variations.

2.2.2.2 DEM model

For the DEM portion of the modeling, we use the parallel N-body gravity tree code *pkdgrav* [86, 87]. With *pkdgrav*, we model individual grains in a single surface patch on Apophis as discrete spherical particles that feel interparticle gravitational and contact forces, as well as forces from a uniform gravity field. Particle contacts, including interparticle friction, are modeled with a soft-sphere discrete element method (SSDEM) [88, 89]. SSDEM allows neighboring particles to slightly interpenetrate at the point of contact as a proxy for surface deformation, with the degree of interpenetration mediated by a Hooke's law restoring spring force in the *pkdgrav* implementation, with a linear spring constant representing a material stiffness akin to a Young's modulus [36] in the normal direction, plus an equivalent tangential spring component as part of the full spring-dashpot model [90]. The SSDEM approach takes user-provided coefficients to

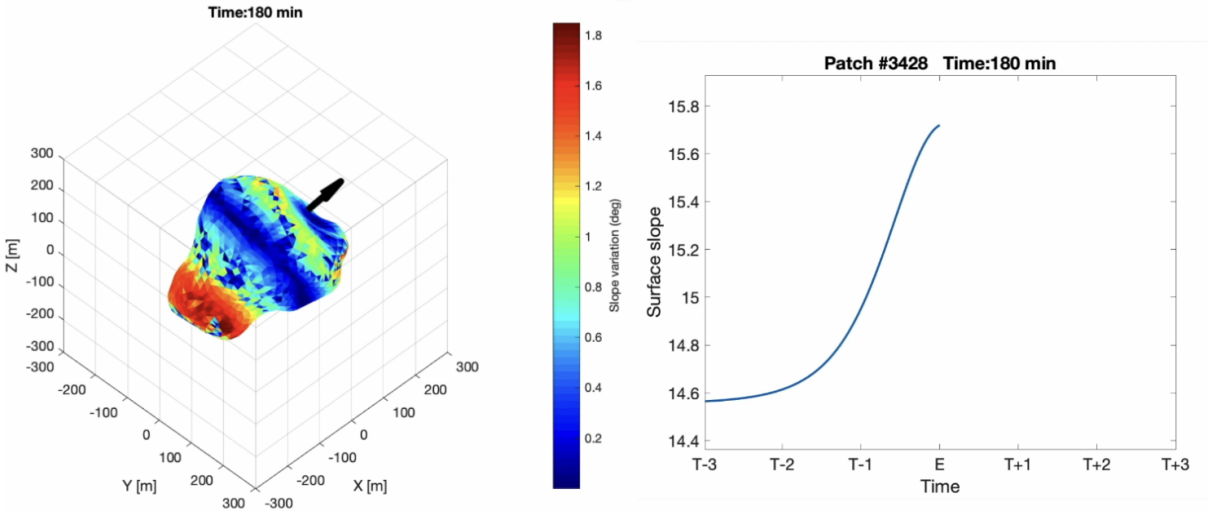

Figure 2.6: A screenshot of the dynamics model simulation. The left-side panel shows how much the surface slope variation occurs on the entire surface of Apophis. The black arrow is heading to the Earth. The right-side graph shows how the surface slope evolves at a single patch. We randomly picked the patch to see the time-varying surface slope. The result is when Apophis has the closest approach during the 6-h encounter simulation.

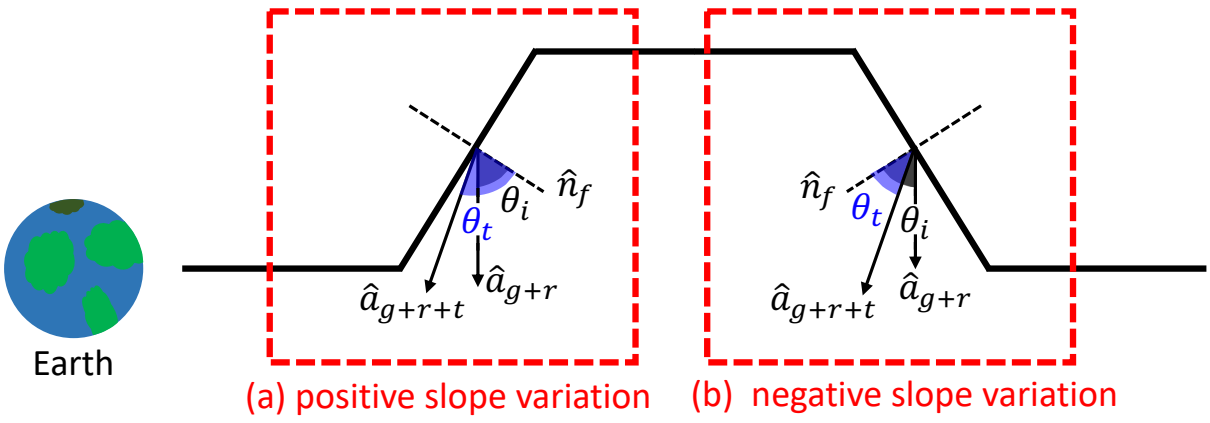

Figure 2.7: The same initial surface slope has either positive or negative slope variation depending on where the Earth is located in the patch frame. Here, the vectors $\hat{n}_f$, $\hat{a}_{g+r}$, and $\hat{a}_{g+r+t}$ are the surface normal, the combined self-gravity and rotational acceleration, and the combined $\hat{a}_{g+r}$ and tidally induced acceleration, respectively. The angles θ_i and θ_t are the surface slope at the initial and at a specific time, respectively. The positive slope variation is when θ_t is greater than θ_i (a), while the opposite case, where θ_t is smaller than θ_i, is the negative slope variation (b).

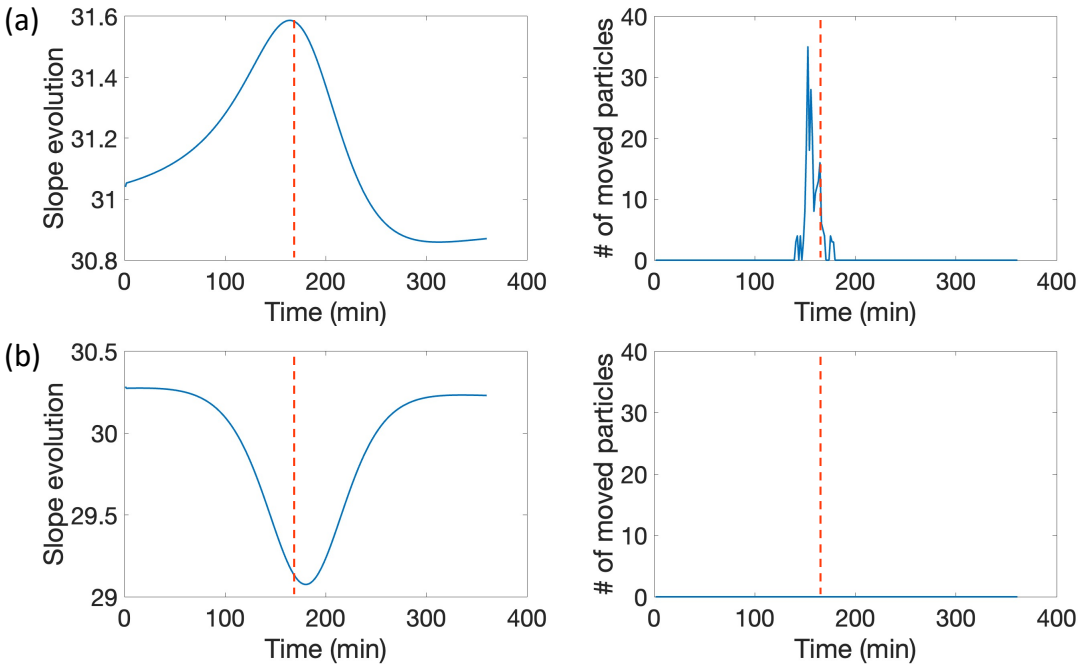

Figure 2.8: Surface slope evolution and the corresponding particle movements for two patches with similar initial slopes. (a) shows the positive slope variation case when subtracting the peak/trough surface slope from the initial slope for a facet has a positive value, while (b) shows the negative slope variation case. The left panels show how the surface slope changes over the 6 h Apophis-Earth encounter. The red dotted line marks the time of closest approach. The number of particles exhibiting significant motion is measured at each time step, plotted, and shown in the right-most panels. Note that in the negative slope evolution case (b) no particles move, while the positive slope evolution case (a) does show particle motion.

account for normal (ε_n) and tangential (ε_t) damping, plus rolling (μ_r), twisting (μ_t), sliding and static (μ_s) friction, and includes a 'shape parameter' (β) to represent grain angularity in rolling interactions [88, 90]. This approach has been validated through comparisons with laboratory experiments [91] and has been used previously by [38] and [36] to study potential surface avalanching and bulk reshaping during the Apophis tidal encounter with the Earth.

2.2.2.2.1 DEM Simulation Parameters The typical facet from the shape model used in the dynamics simulations has mean surface area of 48$\pm$35 m^2 (1-σ). For the SSDEM modeling, we create a single patch with dimensions $(8 \times 8 \times 3)$ m^3 in volume, which has a surface area of 64 m^2, slightly larger than the mean facet surface area from the shape model but still representative. To create the desired patch of particles for the SSDEM modeling, we settle just over $11,000$ spherical particles in free space under the influence of only interparticle self gravity, with particle radii (R_p) ranging from 5.96 to 17.86 cm and with a size-frequency distribution following a power law with slope $\alpha = -3$, roughly matching the size-frequency distributions of decimeter-scale regolith on Bennu's Nightingale Crater [92] and boulders on Itokawa [93, 94]. Figure 2.9 shows the simulated DEM patch for a single surface mesh. Once the initial cloud of particles has settled into a roughly spherical rubble pile, we carve out a region with periodic lateral boundaries $(8 \times 8 \times 3)$ m^3 in volume. We use the same rectangular patch as the initial condition for all of our SSDEM models, as the subsequent tilting stage (described below) provides sufficient randomness in initial particle positions, especially in concert with varying the initial slope and orientation of the patch at the time of encounter from the dynamics models. Throughout the SSDEM modeling, we use friction parameters such that our particle assembly has a friction angle of $\phi = 35.1^\circ$ (see Table 2.3) [44, 90], which results in a typical initial patch packing to a bulk density of 2.2 g cm^{-3}. In the SSDEM models presented in this study, we do not include the effects of interparticle cohesion, although we aim to investigate this in future work (see Section 2.2.5 for details).

We continue to prepare the SSDEM patch for each individual encounter by placing an infinite plane below the particles for them to rest on and applying a uniform acceleration normal to the plane surface with magnitude equivalent to the initial pre-encounter acceleration on the

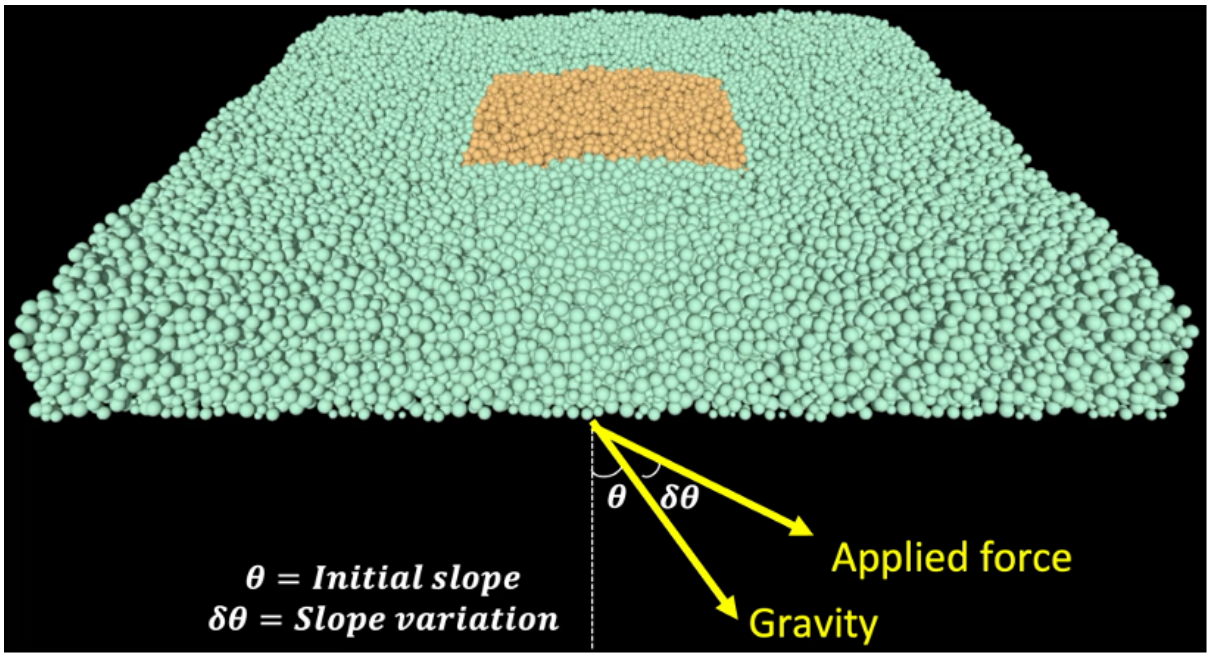

Figure 2.9: The simulated DEM patch. The single patch size is $(8 \times 8 \times 3)$ m^3 in volume, and $11,000$ spherical particles ranging from 5.96 to 17.86 cm are packed. The initial setting of the patch is given when gravity is set as the initial total acceleration from the dynamics model. The time-varying applied forces act on the DEM patch depending on the surface slope variation.

given patch from the dynamics model. We choose our patch depth of 3 m such that particles in the upper layers, where resurfacing may occur, will be physically independent of the underlying plane. Over the course of 4 h of simulated time, we rotate the uniform acceleration vector from the normal direction to the actual initial orientation of the acceleration on the patch from the dynamics model. Slowly rotating the uniform acceleration vector is equivalent to quasi-statically tilting the patch to the same initial slope and orientation as used in the dynamics model; we call this the 'tilting stage' and we rotate the acceleration vector rather than the particles so that we can remain in the frame of the patch for ease of modeling and visualization. We include an additional 2 h of simulated time after the initial acceleration vector has rotated to its final orientation so that the particles in the patch that have shifted slightly during the tilting stage can reach their equilibrium resting positions.

After we have settled a surface patch at the orientation and initial surface acceleration that one of the patches in the dynamics models would feel, we can simulate the full encounter for that patch. We use the tilted and equilibrated patch discussed above and smoothly rotate and change the magnitude of the ambient, uniform acceleration vector in the SSDEM simulations

to match the accelerations ($\vec{a}_g$ in Section 2.1.2) felt by the analogous patch from the dynamics model, interpolated between intervals of 60 s. These simulations last for the same 6 simulated hours as the dynamics models; the particles in the patch uniformly experience the dynamics model accelerations in addition to non-uniform interparticle gravitational and contact accelerations from the other particles. We track particle positions and velocities over time to determine particle motion in the patch and consider each particle that moves by more than half of its radius to exhibit 'significant' motion.

2.2.2.2.2 Resurfacing Estimation For each particle that has moved significantly in our DEM models, we estimate the amount of revealed unweathered surface area with the following assumptions: 1) each particle exhibits perfect rolling motion directly from its initial to its final position along a straight-line path with no sliding; 2) the half of the particle's surface uncovered from above in the patch frame at the beginning of the encounter is 'weathered,' while the remaining half is 'unweathered;' 3) the full area initially underneath a moved particle is 'unweathered;' and 4) only particle motion in the upper 56 cm (3 times the largest R_p) of the particle bed contributes to the patch's resurfacing. We show a sample result from one of our models in Fig. 2.10, where grains exhibiting significant motion are colored green and violet in their initial (left panel) and final (center panel) positions, respectively, with Fig. 2.10 (c) showing the final positions (purple) overlaid on the initial patch (green and gold) to help visualize the downslope motion.

For a single sphere under the above assumptions, we calculate the total revealed unweathered surface area as the sum of the area of the lens of the sphere's revealed unweathered surface (Equation (2.6)) plus the fraction of the revealed cross section initially underneath the sphere (Equation (2.7)):

$$A_{sph} = \frac{\pi}{2} R_p^2 \big(1 - \cos\varphi\big), \tag{2.6}$$

$$A_u = \pi R_p^2 \times \begin{cases} 1, & \frac{d}{2R_p} \geq 1 \\ \frac{d}{2R_p}, & \frac{d}{2R_p} < 1 \end{cases}, \tag{2.7}$$

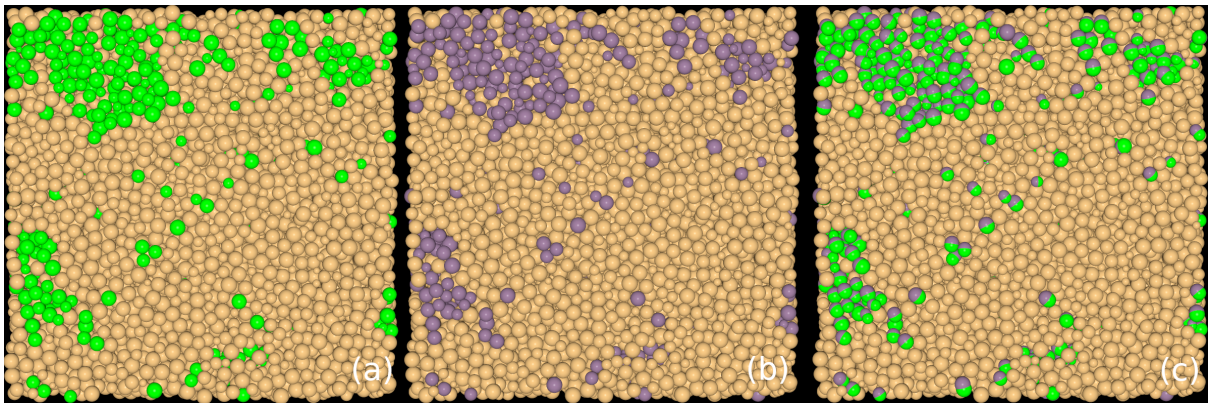

Figure 2.10: A depiction of grain motion in a surface patch in the DEM simulations. (a) shows the initial positions of the grains in this patch, with particles that will exhibit 'significant motion' (a displacement of more than 1 particle radius) colored green. (b) shows the final positions of particles in the patch, with particles exhibiting significant motion in violet. (c) shows the initial state of the patch, just as in (a), overlaid with the final positions of significantly moved particles, to show downslope motion (from green to violet) toward the upper-left side of the frame.

where φ is the angular displacement of the sphere (assuming perfect rolling motion) and d is the linear displacement of the particle during the simulation. A schematic of this motion is shown in Figs. 2.11 (a) and (b), where the central sphere in (a) moves along the green arrow in (b): the revealed unweathered surface area of the sphere (A_{sph}) is colored purple, and the cross section of revealed area initially underneath the sphere (A_u) is colored black.

Under these conditions, a spherical particle with final position exactly one diameter away from its initial position would contribute twice its cross section to the total 'resurfaced' area: the full unweathered cross section of the sphere itself plus the full circular cross-sectional area that was initially below the sphere. The total revealed unweathered area in the patch is then calculated as the sum of the area revealed by each sphere, still applying the above assumptions:

$$A_{tot} = \sum_{i=0}^{N} A_{sph,i} + A_{u,i}. \tag{2.8}$$

The possibility of one sphere covering an area of surface revealed by another sphere is accounted for by subtracting the area of a lens from the 'revealed' area underneath of a sphere based on the initial and final positions of the particles and their relative radii. This scenario is illustrated in Fig. 2.11 (c), where another moving sphere covers the black 'revealed' area in the center, indicating that we no longer include the newly covered fractional area in A_u.

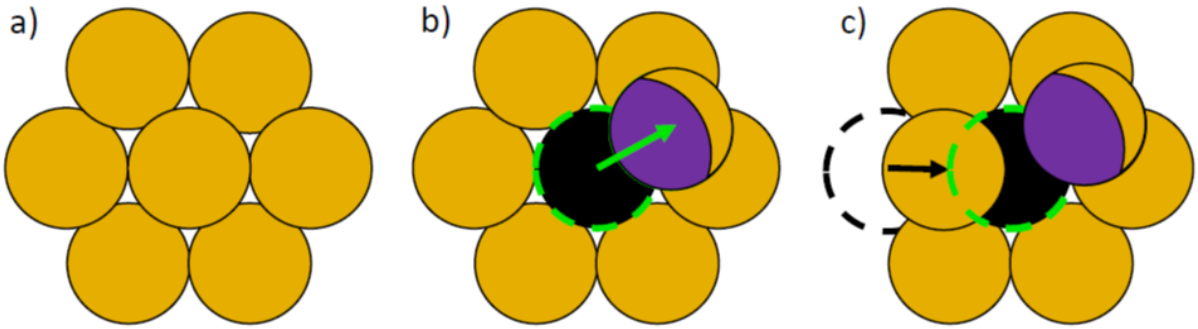

Figure 2.11: A schematic diagram indicating how we account for the amount of revealed unweathered area when a particle in the system moves. (a) shows the initial configuration of some particles in the patch. (b) indicates motion of the central particle along the green arrow. The black area with the green dashed outline indicates the revealed unweathered area initially below the moved sphere (A_u), while the purple fraction of the moved sphere indicates the revealed area of its surface, which is initially unweathered (A_{sph}). (c) indicates another particle moving at a later time, along the path of the black arrow, and covering some of the area that initially counted toward A_u from the central particle's motion. Since some of the black circle has been covered, we no longer count the covered portion toward A_u.

2.2.3 Results

Using the tidal resurfacing model, we select 655 surface patches—enough to densely sample the full range of slope variations and initial slopes below the 35° friction angle—and measure the number of grains that exhibit significant motion, as defined above. We sort the simulated patches given their surface slope profiles (initial surface slope and slope variation) and compile the grain motion predictions estimated in the resurfacing estimation phase of the DEM models (Section. 2.2.2.2.2). We then find the correlation between the grain motions and surface slope profiles to constrain the tidal resurfacing across the entire surface (Section 2.2.3.1). In Section 2.2.3.2, we create global surface maps to show the expected resurfaced areas after 3 representative encounter orientations and then demonstrate how the expected resurfaced locations differ depending on the orientation of Apophis at the time of encounter.

2.2.3.1 Correlation between surface slope profiles and constrained grain motions

To discover how the grain motion in a patch correlates with its surface slope profile, we conduct a simple statistical analysis. We first bin the selected 655 surface patches in 2 dimensions: initial slope and slope variation. Here, the bin sizes of initial slope and slope variation are set in

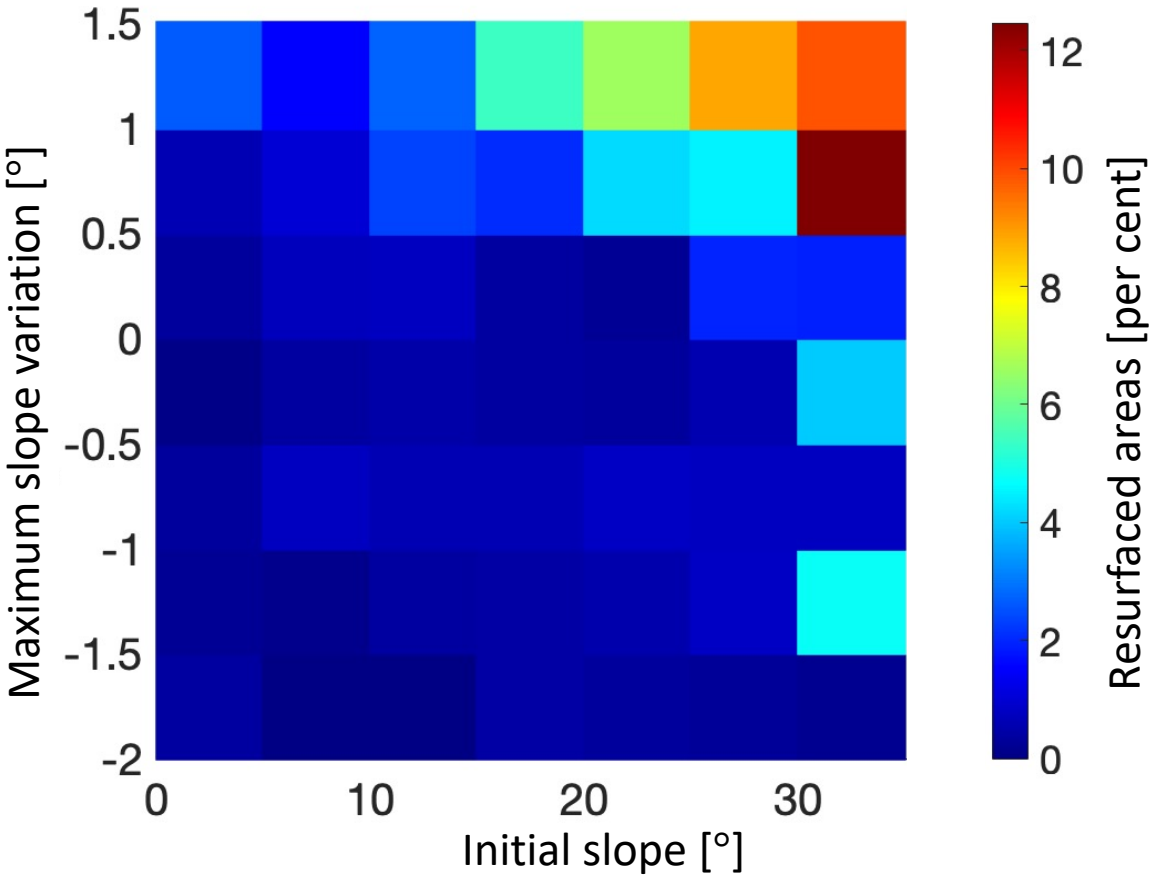

Figure 2.12: A statistical result showing the correlation between surface slope profiles, namely the initial slope and maximum slope variation, and resurfaced area for each surface patch. Resurfaced area defines the total revealed unweathered surface area in a patch (A_{tot}, equation (2.8)) as a percentage of the entire surface area of the patch (64 m^2). Note that the highest initial slope and positive variations give rise to the greatest resurfacing shown in the upper right corner. Areas expected to experience the greatest resurfacing will be the initially high-sloped regions having a positive slope variation, which is affected by the encounter orientation.

increments of 5° with a range of $[0°,\ 35°]$ and 0.5° with a range of $[-2°,\ 1.5°]$, respectively. On average, each bin includes 13 surface patches. After binning the data, and computing the total resurfaced area for each patch (Section 2.2.2.2.2) as a percentage of the total patch area, we compute the average percentage of resurfaced area for the surface patches in each bin. Figure 2.12 shows the average resurfacing in each bin as an 'expected' percentage of resurfaced area for a patch given an initial slope and slope variation.

The first trend we see in Fig. 2.12 is that the initially high-sloped regions (see the right-hand side of Fig. 2.12 where the initial slope $> 30°$) typically show locally resurfaced areas

regardless of the slope variation, which means that the surface grains at high-sloped regions are more susceptible to downslope movement. This trend is supported by the fact that erosion rates by downslope regolith flow become high as surface slopes are close to the angle of repose [45, 95]. The second feature we observe in Fig. 2.12 is that large slope variation (see the top of Fig. 2.12) is a dominating factor in determining regions of resurfacing. We find that most surface patches with slope variations exceeding +0.5° show local resurfacing despite some such patches having initial slopes far less than the angle of repose. Granular flow in a region of sub-critical slope (below the angle of repose) has been previously suggested by [47], who numerically showed that the tidal forcing from Mars could cause surface mobility on Phobos in areas with significant slope variations, even in regions with slopes less than the angle of repose. Although the tidal forcing on Phobos is different from what Apophis will experience, in that Phobos is continuously under the tidal effects of Mars while Apophis experiences a one-time event from Earth, we still find that the mid-sloped regions (initial slope between 15° and 30°) on Apophis are likely to experience resurfacing when there is a significant slope variation ($> 0.5^\circ$). When grain motions occur in mid-sloped regions, we note that the slope variation increases the patch slope prior to the closest approach distance (positive y-axis values in Fig. 2.12), while the grains in surface patches with negative slope variations are relatively stable and motionless, despite similar initial slopes and slope variation magnitudes. Figures 2.8 (a) and (b) show how the surface slope evolves (left-most panels) at sampled patches that have a slope increase and decrease, respectively. The corresponding right-side panels of Fig. 2.8 show the number of particles moving at each timestep measured in the DEM models during the 6-h encounter. The initial slopes for both patches are similarly set to $\sim$30°. The magnitude of the slope variation is slightly higher in the decreasing case, Fig. 2.8 (b), but both exceed 0.5° in absolute magnitude. We observe the surface grains actively moving when the slope variation is positive, however there is no significant grain motion in the patch with negative slope variation. In addition, the most significant grain motion occurs just before perigee when the slope rate of change is highest (the closest encounter happens at 180 min and is marked as a red dotted line in each panel of Fig. 2.8). This feature is commonly observed in other patches exhibiting significant grain motions.

2.2.3.2 Influence of encounter orientation on expected resurfaced area

Based on the results from Sec. 2.2.3.1, we find that the encounter orientation may be a dominant factor in predicting locations and total areas of resurfacing during the 2029 Apophis-Earth close encounter because different encounter orientations cause different surface slope profiles. To explore the influence of encounter orientation on regions of tidal resurfacing, we randomly select the encounter orientations rather than propagating from the current spin state because predicting the spin orientation of Apophis at the time of its closest approach to the Earth using the currently existing data still has a large uncertainty [82, 70]. We originally conduct 30 simulations with different encounter orientations but first introduce 3 representative cases chosen to maximize observable differences in resurfacing as a result of encounter orientation. In the dynamics model, we set 3 different initial spin orientations (at a time of 3 h before the closest encounter), which each place Earth above different coordinate planes in the body frame of Apophis at the time of perigee. Figure 2.13 shows a surface color map representing the largest magnitude of slope variation (aka. Maximum Slope Changes in the colorbar label of Fig. 2.13) across Apophis's entire surface during the encounter for each orientation. For the encounter orientations, the Earth is located above the x-y plane for Fig. 2.13 (a), the x-z plane for Fig. 2.13 (b), and the y-z plane for Fig. 2.13 (c).

For all 3 orientation cases, we confirm that the patches showing the largest maximum slope variations are clustered on the side of the object experiencing the strongest tidal forces, where the patches face the Earth for most of the duration of the encounter. As an example, Fig. 2.13 (a), when the Earth is located above the x-y plane, shows that the most significant slope variations, both positive and negative, occur for the patches nearest the Earth. Figure 2.13 indicates that the largest slope variations occur in the patches closest to the Earth, but not all patches have positive slope variations because the slope change is affected by the orientation of the patch normal vector compared to the direction of the Earth. Figure 2.7 depicts two cases where the same tidal force induces a positive or negative slope change depending on the different initial orientation of the patches relative to the vector of the Earth's tides. When the tidal force acts along the direction normal to the patch, it induces positive slope variation. The tidal

force vector acting opposite the asteroid's gravity prevents grains from resting on the surface and is more likely to induce significant grain motions. In contrast, the force vector causing the negative slope variation plays a role in strengthening the local gravity vector and thus lets grains pack tighter to the surface. This interpretation supports the trend seen in Fig. 2.12 that more grain motion is observed in patches with positive slope variations rather than negative ones.

Using the slope profiles for each encounter orientation driven by the dynamics model, we extrapolate expected areas of resurfacing across the entire surface of Apophis for 3 different encounter orientation cases (see Fig. 2.14). The amount of resurfacing on each patch is defined by mapping its initial slope and slope variation onto the statistically averaged plot from Fig. 2.12. We note that there are common areas that have the resurfaced patches seen in all cases, such as the 'neck' region of the contact binary shape. These areas are initially high-sloped regions, with slopes exceeding 30° or with supercritical initial slopes (higher than the expected friction angle), and are subject to tidal resurfacing regardless of encounter orientation. Despite the expected tendency for initially high-sloped regions to experience resurfacing, we find the encounter orientation still significantly influences how much resurfacing we see at those regions and how much we expect adjacent patches to also experience resurfacing (defining the 'width' of the resurfacing region). We mark the common areas that show significant resurfacing and have the widest neighboring resurfaced regions as red solid circles in Fig. 2.14 and find that these regions typically match the initially high-sloped regions with the largest positive slope changes. As an example, the location marked as the red solid circle in Fig. 2.14 (a) shows that significant resurfacing is expected at a high-sloped region on the neck when the Earth is located above the x-y plane. However, the same location when the Earth is located above the y-z plane (Fig. 2.14 (c)) shows very limited expected tidal refreshing. When we look at the slope changes when Earth is above the x-y plane (Fig. 2.13 (a)), we see positive slope variations in the aforementioned area around the neck, while this same region shows decreasing slopes when the Earth is above the y-z plane. We reaffirm this trend in another initially high sloped region represented in the red solid circle in Fig. 2.14 (c). At this area, larger positive slope variations occur in the case when the Earth is on the y-z plane (Fig. 2.13 (c)) than the other 2 orientation

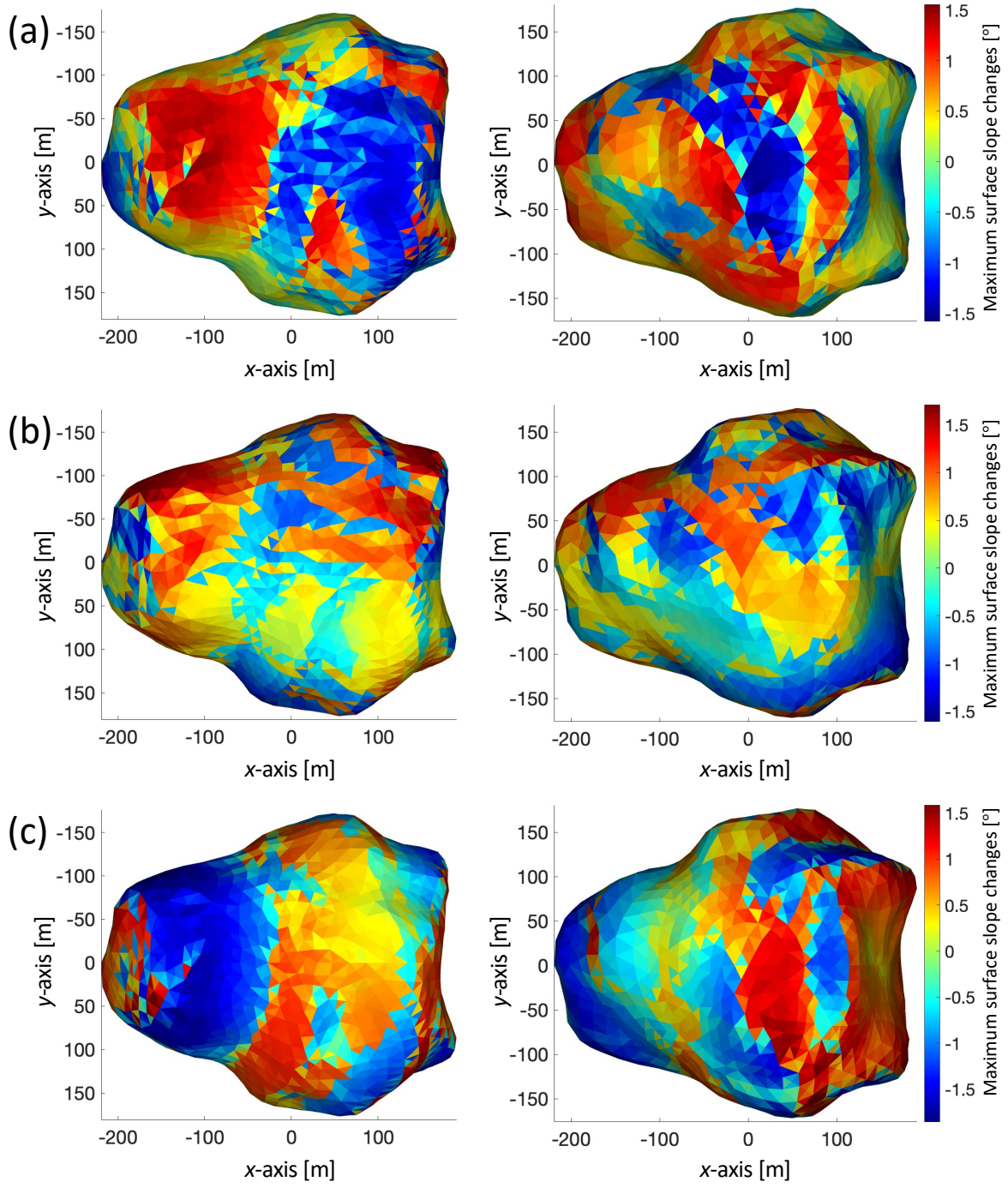

Figure 2.13: Maximum slope changes with different encounter orientations: the Earth is located above the x-y plane (a), the x-z plane (b), and the y-z plane (c). The left-most maps show the facets above the x-y plane, while those on the right-hand side are below the x-y plane. All coordinate planes refer to the body-fixed frame of Apophis with the origin at the center of body and x- and z-axes aligned with the longest and shortest primary body axes, respectively.

cases (Figs. 2.13 (a) and (b)). Besides the commonly resurfaced areas, we notice that there are certain regions that can show strong signals for resurfacing depending on the exact encounter orientation. We mark those regions in dashed red circles in Fig. 2.14. These regions mostly match with the mid-sloped patches (15 – 30 deg) nearest the Earth and thus have large slope variations that induce regolith motion. This result again indicates that the regions of expected resurfacing are strongly related to the encounter orientation.

To support the features we found by comparing 3 representative encounter orientation cases, we statistically investigate the estimated resurfacing for high-, mid-, and low-sloped patch subsets in 30 encounter orientation cases (see Fig. 2.15). Our metric for quantifying how many patches in each subset are being significantly resurfaced is the number of patches for which $A_{tot} \geq 0.03 A_{patch}$. The mean expected resurfaced area in mid- and low-sloped patches is less than 3%, thus the value (0.03) is chosen in the above inequality to most clearly delineate the color difference in the fraction of resurfaced patches among low-, mid-, and high-sloped patches. As expected, the high-sloped patches have the largest fraction experiencing significant resurfacing for all encounter orientations—represented by the colorbar in Fig. 2.15. The results indicate a maximum of 80 per cent and a minimum of 32 per cent of all initially high-sloped patches have more than 3 per cent of their total area resurfaced across our 30 orientation simulations. In all cases, this group has a higher level of average expected resurfaced area and larger standard deviations than the initially mid- and low-sloped patch subsets, despite variations dependent on the encounter orientation. The trend here supports the feature indicated in our 3 representative cases: that the degree of resurfacing and the width of the resurfacing regions at the initially high-sloped locations depend strongly on the encounter orientation. For the mid-sloped patch subsets, our results show that a small fraction ($\sim$10 per cent) of the patches experience significant resurfacing, and have a lower expected resurfaced area than the higher-sloped patches. As we confirmed in the comparison of our 3 representative encounter orientations, the resurfaced regions in the mid-sloped subset of patches match areas with significant positive slope variations. Unlike the high-sloped and mid-sloped patches, we confirm that the low-sloped patch subset is stable against tidal resurfacing regardless of the encounter

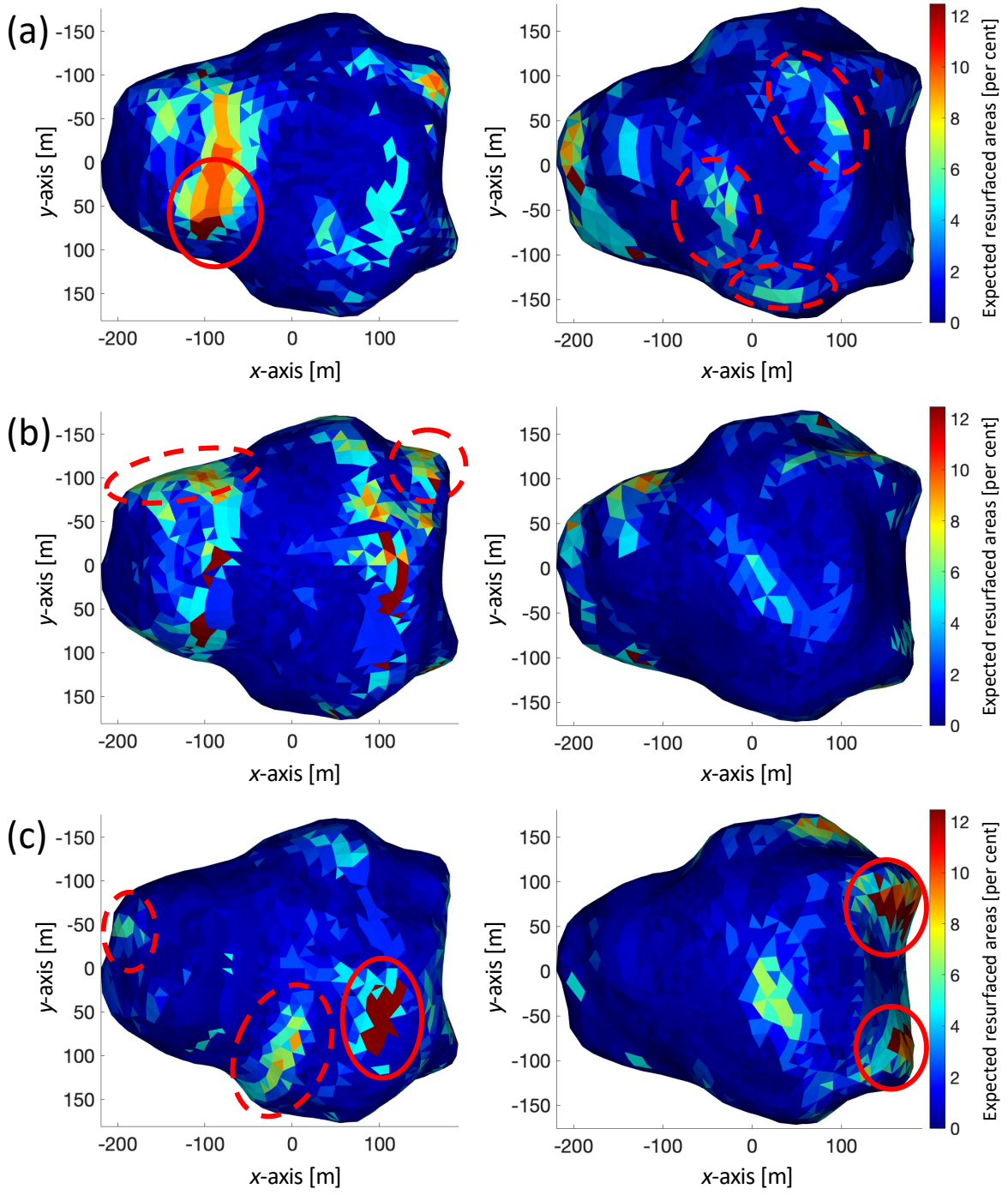

Figure 2.14: Global surface map showing the expected tidal resurfacing level, which is estimated by the statistical resurfacing result in Fig. 2.12, with different encounter orientations: the Earth is located above the x-y plane (a), the x-z plane (b), and the y-z plane (c). The left-most maps show the facets above the x-y plane, while those on the right-hand side are below the x-y plane. The red solid circles denote locations where the most active grain motions occur at the initially high-sloped regions among 3 orientation cases. The red dotted circles define some locations where our models indicate significant resurfacing only in specific encounter orientations.

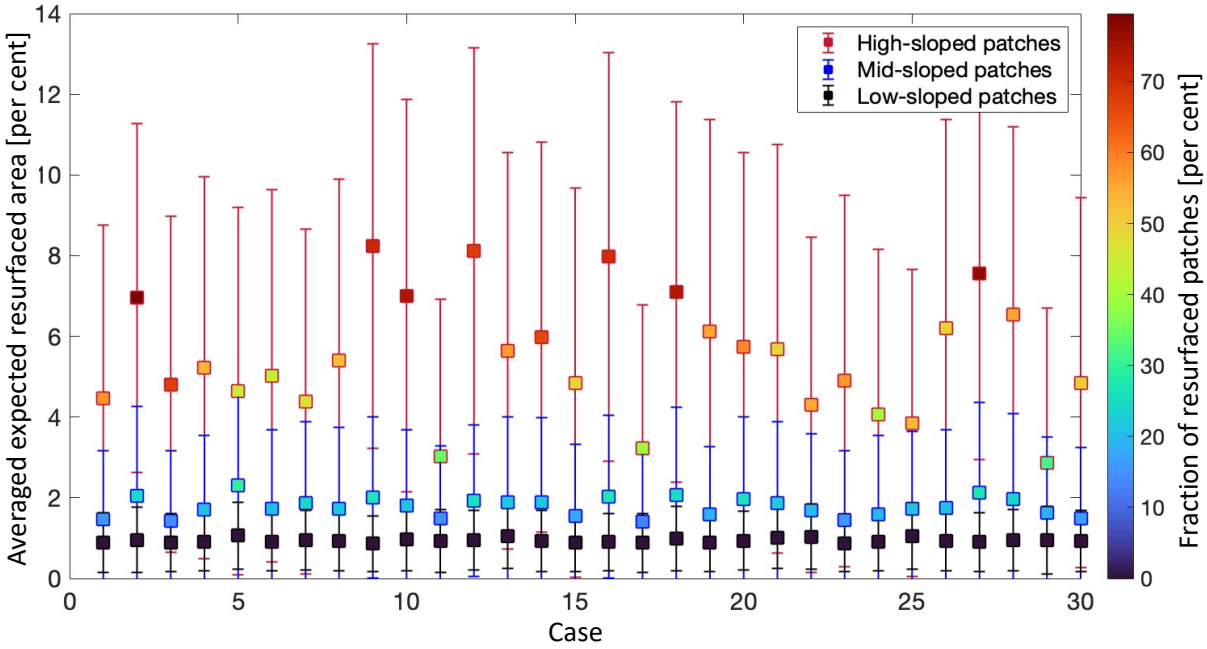

Figure 2.15: Simulation results for 30 different encounter orientation cases. The red, blue, and black errorbar colors represent the group of patches sorted into the initially high-sloped ($> 30°$), mid-sloped ($15°$–$30°$), and low-sloped ($< 15°$) subsets, respectively. The square shows the mean expected resurfaced area for each group, with error bars representing one standard deviation in the positive or negative directions. The color of the square represents the fraction of patches in that subset that have a total expected resurfaced area of at least 3 per cent of the total patch area.

orientation. As a final note, we address that all of our simulated cases indicate very local resurfacing, with a total expected resurfaced area of only 1 per cent of the entire Apophis surface area.

2.2.4 Discussion

Our simulation results indicate that the initially high-sloped regions show more grain motion than the low-sloped regions with a similar slope variation. This finding indicates that initially high-sloped regions are more sensitive to tidal refreshing because even a relatively small slope variation can make the surface slope exceed the friction angle. This result may indicate potential common areas that will experience tidal resurfacing during the Earth flyby regardless of the encounter orientation. If the initially high-sloped regions from the current shape model truly exist on Apophis itself, however, these areas might already exhibit fresher and brighter

regolith than other areas before the encounter. The high-resolution images from in-situ missions to S-types Itokawa and Eros show evidence of surface color variations on both bodies. Earlier studies (e.g., [75, 96]) found a correlation between these surface color variations and the surface slope distribution: the higher-sloped areas tend to show brighter surfaces because of down-slope grain motion that exposed fresher material underneath the weathered top layer, while the lower-sloped areas were covered in loose, weathered regolith believed to have migrated there. In consideration of the features seen on the surfaces of Itokawa and Eros, the initially high-sloped regions on the Sq-type Apophis's surface might already show fresher and brighter regolith unrelated to the upcoming tidal interaction, or as a result of previous tidal resurfacing. If we could obtain a surface map of the pre-encounter state of Apophis from a time when the tidal effect of the 2029 Earth encounter is negligible, comparing it against a similar post-encounter surface map would be a way to accurately confirm whether the upcoming planetary encounter will cause any brighter surface colors at the initially high-sloped regions. Besides that, we also note that some initially high-sloped regions from the shape model may be not be realistic, given that the current Apophis shape model still has significant uncertainties, as addressed by [1].

We also find that the encounter orientation is the dominating factor in predicting more targeted areas where we could detect tidal refreshing, given that a positive slope variation is more likely to induce surface grain motion. Since the same location in the body frame can have positive or negative slope variation depending on where the Earth is located in the patch frame, any area can be subject to resurfacing. When the Earth's tides are close to being aligned with the patch normal or downslope direction (Fig. 2.7 (a)), the tidal force competes with local gravity, preventing the grains from resting on the surface, thereby inducing motion. This means that we can predict areas of expected tidal refreshing on the surface of Apophis given more accurate knowledge of the encounter orientation at perigee. Currently, the most feasible way to predict the encounter orientation of Apophis during the 2029 flyby is by propagating the well-constrained spin state from the 2012–2013 apparition to the 2029 apparition while considering the potential tidal effects from the Earth, non-principal-axis rotation, and minor

effects of Yarkovsky and YORP that could dynamically alter the object's rotational state. Unfortunately, there are still significant uncertainties in the spin-state data from past apparitions [82, 1], and the computational errors associated with propagating the spin state over $\sim$16 yr are fairly significant. Given these uncertainties, the best way to improve our knowledge of the 2029 encounter orientation must come from ground observations in the time just before the 2029 encounter: the DSS-13 and DSS-14 antennas at Goldstone will start in mid-March and the DSS-43 antenna at the Canberra Deep Space Communication Complex in Australia will cover the time around the closest approach [97]. We anticipate that these pre-encounter radar observations will provide accurate detail about the rotational state of Apophis, which can then be used to constrain the likely areas of resurfacing, so that those areas can be targeted for confirmation by potential spacecraft and ground-based observations.

Lastly, we confirm that active grain motion most commonly occurs in the half hour before perigee (as shown in the right-side frame of Fig. 2.8 (a)) and with total resurfacing on the scale of $\sim$1 per cent of Apophis's entire surface area. These findings provide essential information about the timing and scale of potential tidal resurfacing, which could support the mission planning of observation campaigns and OSIRIS-APEX. In most patches, surface grains move actively when the patch slopes change most rapidly; the changing surface accelerations can make the grains unstable and move from their equilibrium positions. This means that the best time to detect active tidal resurfacing is during the last hour before Apophis reaches perigee, after which the surface grains reach new equilibrium positions because the rates of change in the patch slopes become smaller. We also note that the global tidal resurfacing that we predict is not extensive, which is consistent with conclusions from previous studies [38, 70]. However, our results still indicate that tidal resurfacing may be seen in certain localized regions—initially high-sloped areas and mid-sloped regions with significant positive slope variation. Given these indications, ground-based observations could detect the level of tidal resurfacing that our models predict if there are precise surface images or albedo maps both before and after the closest encounter. [97] address that Goldstone DSS-13 and DSS-14 antennas can obtain high-resolution radar images that would place tens of thousands of pixels on Apophis during the time 10 days before to 10 days after the closest encounter. That kind of

radar observation covers the time of the 6-h encounter considered in our simulations and can help provide a new, very detailed shape model, possibly capturing surface features as small as a few meters in size. Not only the radar observations, but optical observations can also support the shape refinement and obtain a database of Apophis's surface albedos (the optical telescopes that could observe Apophis are listed in Table 2 in [98]). The new model prior to the encounter can be used for more refined dynamics modeling to better constrain resurfaced areas. If tidal resurfacing indeed occurs as we predict, we expect evidence of tidal resurfacing to be detectable via analysis of surface images or albedo changes at the resurfaced areas predicted by the refined dynamics model. Considering the small scale of tidal resurfacing we predict, a change in the moments of inertia due to tidal resurfacing is likely to be minimal. Surface properties such as roughness and grain size distributions, important factors in our DEM modeling, could also be better characterized by dual-polarization imaging. Furthermore, other radar facilities such as the 10 GHz HUSIR (Haystack Ultrawideband Satellite Imaging Radar in Westford, Massachusetts) can resolve finer surface features with image resolutions down to a few centimeters near the time of perigee, which could be enough to detect active tidal refreshing. Lastly, the expected surface images from the OSIRIS-APEX mission can be combined with ground-based observations to better understand the influence of the tidal encounter on the surface, despite the spacecraft arriving at Apophis 4 months after the close encounter [63, 99].

2.2.5 Limitations

We address two main limitations for the current tidal resurfacing model in the DEM stage: 1) the relatively low porosity of the patch; and 2) the neglecting of cohesive forces in our models. The initial patch used for the DEM modeling stages has a $\sim$45 per cent porosity as a result of allowing the particles to coalesce under self gravity before carving out the shape of our patch (here we are referring to macroporosity between grains, i.e., 45 per cent porosity implies 55 per cent of the volume is occupied by solid grains and the remaining 45 per cent is void space between the grains). For comparison, the estimated bulk porosity for both of the rubble piles Bennu and Ryugu, recently visited by the OSIRIS-REx and Hayabusa2 spacecrafts, respectively, is around 50 per cent [100, 101], while the surface regolith layer is estimated to have a

significantly higher porosity [92]. This indicates that we are underestimating the porosity of the patches in our DEM models and likely underestimating the degree of resurfacing. Creating systems with significantly different porosities (by more than a few percent) would require preparing the patch in a way that is ad hoc or possibly unphysical, using unrealistic material parameters, adding cohesion during the packing stage, or modeling with irregular particle shapes [e.g.,[102, 103]]. The more void space there is in the patch, the more easily the patch can shear, as the structures maintaining the particle configuration will be less stable. The sample acquisition from the OSIRIS-REx mission to Bennu gave results that indicate potentially 70 per cent or higher porosity in the upper regolith layer on Bennu [92], implying a more 'fluffy' surface regolith structure than we are modeling here. Apophis is an Sq-type asteroid, which, based on comparisons with Sq-type Itokawa [104] and S-type Eros [105], may imply the presence of more fine-grained surface material compared to the boulder-heavy surface of the B-type Bennu [100]. Since the porosity approximation comes from Bennu's Nightingale Crater, where there are more fines than other regions of the surface [106], and without significant additional data about Sq-type surfaces, we still believe Bennu to be a satisfactory point of comparison. Regardless, we intend to investigate the effects of modeling regolith systems with higher porosities in a future study.

In contention with the low porosity of our patch, which may be reducing the amount of resurfacing we see, is the absence of cohesion in our models. Interparticle cohesive forces like Van der Waals forces can increase the shear strength of a granular assembly, keeping the system stable against the relatively weak tidal forces felt by any given surface patch. At the scale we model, where particles are tens of centimeters in diameter, we expect very low interparticle cohesion, if any [107]. Still, even a small amount of cohesion could be enough to restrict the resurfacing that we see in our models. This will be investigated in our future work.

2.2.6 Conclusions

This study visits the topic of tidal refreshing on the surface of Apophis, a phenomenon that may be observable during the 2029 Apophis-Earth close encounter, using our tidal resurfacing model. The main finding in this work is that the tidal resurfacing likely occurs at small scales

in very localized regions, mostly 30 min before the closest encounter. In particular, the orientation of Apophis at the time of closest approach will control which areas on the surface may experience tidally induced resurfacing. If detailed surface topographic maps or albedo data during the encounter event can be obtained through the collaboration of ground-based observation campaigns and in-situ missions, we may detect evidence supporting local tidal resurfacing as a result of the close Earth encounter.

Table 2.2: Surface slope data. $\delta\theta$ shows the minimum and maximum value at Region II, excluding Region I. If this value is unchanged (i.e., Region I = Region II), $\delta\theta$ shows the slope variation across the entire surface with a parenthesis. The increase rate defines the area difference between Region II and Region I. For the 2.8 hr case, five AR cases are introduced to illustrate the variations in the increase rate. Note that RI and RII mean Region I and Region II, respectively.

Setting		Pre-encounter Time		Planetary Encounter Time		
AR	R_E	Mean slope (°)	RI (%)	RII (%)	Increase Rate (%)	$\delta\theta$ (°)
Spin period - 1.5 hr						
1.0	3.5	83.2	97	97.4	0.4	0.47 - 1.94
0.8	3.5	82.7	96.2	96.2	0	(0.20 - 4.68)
0.57	3.5	82.3	96.6	96.6	0	2.50 - 3.17
1.0	5	83.2	97	97.4	0.4	0.31 - 0.69
0.8	5	82.7	96.2	96.2	0	(0.06 - 1.62)
0.57	5	82.3	96.6	96.6	0	0.63 - 0.80
1.0	10	83.2	97	97.4	0.4	0.06 - 0.09
0.8	10	82.7	96.2	96.2	0	(0.01 - 0.23)
0.57	10	82.3	96.6	96.6	0	(0.01 - 0.30)
Spin period - 2.8 hr						
1.0	3.5	22.3	0	22.7	22.7	4.12 - 16.23
0.9	3.5	22.7	0	31.5	31.5	3.13 - 19.89
0.8	3.5	24	10.2	46.9	36.7	5.12 - 34.48
0.7	3.5	26.7	22.1	55	32.9	6.89 - 148.83
0.57	3.5	33.1	33.7	63.4	29.7	9.14 - 38.41
1.0	5	22.3	0	0.7	0.7	3.96 - 4.22
0.9	5	22.7	0	6.9	6.9	1.62 - 4.67
0.8	5	24	10.2	20.9	10.7	2.21 - 6.92
0.7	5	26.7	22.1	33.2	11.1	2.88 - 34.24
0.57	5	33.1	33.7	43.6	9.9	3.80 - 11.22
1.0	10	22.3	0	0	0	(0.01 - 0.53)
0.9	10	22.7	0	0	0	(0.01 - 0.74)
0.8	10	24	10.2	11.8	1.6	0.31 - 0.75
0.7	10	26.7	22.1	23.5	1.4	0.34 - 2.66
0.57	10	33.1	33.7	34.8	1.1	0.39 - 0.98
Spin period - 3.1 hr						
1.0	3.5	16.6	0	0	0	(0.04 - 13.08)
0.8	3.5	16.9	0	0	0	(0.10 - 11.08)
0.57	3.5	22.5	15.4	29.7	14.3	7.13 - 21.88
1.0	5	16.6	0	0	0	(0.02 - 3.72)
0.8	5	16.9	0	0	0	(0.02 - 4.73)
0.57	5	22.5	15.4	17.7	2.3	2.41 - 8.36
1.0	10	16.6	0	0	0	(0.01 - 0.39)
0.8	10	16.9	0	0	0	(0.01 - 0.60)
0.57	10	22.5	15.4	16.8	1.4	0.78 - 1.72

Table 2.3: *pkdgrav* DEM Simulation Parameters

Quantity	Symbol	Value
Particle Number	N	7141
Particle Radius	R_p	5.96–17.86 cm
Size-Frequency Distribution Slope	α	–3.0
Coefficients of Restitution (*)	$\varepsilon_n, \varepsilon_t$	0.55
Coefficient of Static Friction	μ_s	1.0
Coefficient of Rolling Friction	μ_r	1.05
Coefficient of Twisting Friction	μ_t	1.3
Shape Parameter	β	0.7
Angle of Friction	ϕ_f	35.1°
Initial Patch Bulk Density	ρ_b	2.2 g cm^{-3}
Patch Dimensions (full side lengths)	$l \times w \times h$	$(8 \times 8 \times 3)$ m^3

Note. (*) ε_n and ε_t define a normal and tangential coefficient, respectively. Spring-dashpot normal and tangential damping coefficients C_n, C_t are dependent on the masses of interacting particles. For any 2-particle interaction: $C_n = C_t \in [9.78, 263]$ kg s^{-1}.

Chapter 3

Structure analysis

Given their complex dynamics, investigating small bodies' structure conditions can provide essential information to understand their evolutionary history. For this study, we develop the finite element model (FEM), which can compute the time-varying stress field of an irregularly shaped object given its dynamical states (Section 3.1). Here, we select interesting objects in small bodies as a case study and set a key science question. The FEM is extended to be adequately used to explore the question. The targeted small bodies are: 1998 KY26 (Section 3.2), (16) Psyche (Section 3.3), and (486958) Arrokoth (3.4).

3.1 FEM general formulation

In this section, we define a regular, bold and bold italic letter as a scalar, matrix and vector, respectively. We start with the structural equation in the form of a partial differential equation, driven by the theoretical assumption that all stress components in the continuum obey Newton's law of motion [108]. Then we adopt Galerkin approximation that provides a numerical solution to a partial differential equation by finite element method [109, 110]. The structural equation is given by

$$\rho \frac{\partial^2 \vec{u}}{\partial t^2} = \nabla^T \vec{\sigma} + \rho \vec{b} \tag{3.1}$$

where ρ is the bulk density, $\vec{u}$ is the displacement vector that consists of [u_x, u_y, u_z], $\vec{\sigma}$ is the stress vector that includes [σ_{xx}, σ_{yy}, σ_{zz}, σ_{xy}, σ_{xz}, σ_{yz}], and
$Vecb$ is the loading vector that contains [b_x, b_y, b_z]. In the equilibrium state, the acceleration

term, the left-hand side of Equation (3.1), becomes a zero ($\rho\frac{\partial^2\vec{u}}{\partial t^2} = 0$). We then define the weak form of this equation by considering the four-node tetrahedral mesh. The weak form of Equation (3.1) in the equilibrium state is given by

$$\iiint_V (\Pi\nabla^T\vec{\sigma} + \Pi\rho\vec{b})dV = 0 \tag{3.2}$$

where Π becomes any given variable.

We use a four-node tetrahedral FEM mesh and thus formulate this equation for each finite element. In the following discussion, the superscript j represents the j^{th} element. For example, $\vec{u}^j$ describes a 3-dimensional displacement vector of the j^{th} solid element. Using the shape function ($\mathbf{N}^j$), we further define $\vec{u}^j$ as $\mathbf{N}^j\bar{\vec{u}}^j$. Here, $\bar{\vec{u}}^j$ is a 12-dimensional vector that consists of a 3-dimensional vector of each node of four-node tetrahedral elements. The shape function plays a role in approximately characterizing variables in the off-node region. The details are well described in Section 2.2.3 in [72], and we follow the same definition of $\mathbf{N}^j$. In the same way, we define $\vec{b}$ and $\vec{\sigma}$ as $\mathbf{N}^j\bar{\vec{b}}^j$ and $\mathbf{N}^j\bar{\vec{\sigma}}^j$, respectively. In the linear elasticity, we introduce Hooke's law to describe $\vec{\sigma}^j$, which is given as

$$\vec{\sigma}^j = \mathbf{K}^j\vec{\epsilon}^j = \frac{E^j}{(1+\nu^j)(1-2\nu^j)}\begin{bmatrix} 1-\nu^j & \nu^j & \nu^j & 0 & 0 & 0 \\ \nu^j & 1-\nu^j & \nu^j & 0 & 0 & 0 \\ \nu^j & \nu^j & 1-\nu^j & 0 & 0 & 0 \\ 0 & 0 & 0 & \frac{1-2\nu^j}{2} & 0 & 0 \\ 0 & 0 & 0 & 0 & \frac{1-2\nu^j}{2} & 0 \\ 0 & 0 & 0 & 0 & 0 & \frac{1-2\nu^j}{2} \end{bmatrix}\begin{bmatrix} \epsilon_{xx} \\ \epsilon_{yy} \\ \epsilon_{zz} \\ 2\gamma_{xy} \\ 2\gamma_{xz} \\ 2\gamma_{yz} \end{bmatrix} \tag{3.3}$$

where E^j is Young's modulus, ν^j is Poisson's ratio, and $\vec{\epsilon}^j$ is the strain vector that consists of [ϵ_{xx}, ϵ_{yy}, ϵ_{zz}, ϵ_{xy}, ϵ_{xz}, ϵ_{yz}]. The components of the strain vector are replaced with $\nabla\mathbf{N}^j\bar{\vec{u}}^j$ as shown in the following logic.

$$\vec{\epsilon}^{j} = \begin{bmatrix} \frac{\partial u^j}{\partial x} \\ \frac{\partial v^j}{\partial y} \\ \frac{\partial w^j}{\partial z} \\ \frac{\partial v^j}{\partial x} + \frac{\partial u^j}{\partial y} \\ \frac{\partial w^j}{\partial x} + \frac{\partial u^j}{\partial z} \\ \frac{\partial w^j}{\partial y} + \frac{\partial v^j}{\partial z} \end{bmatrix} = \begin{bmatrix} \frac{\partial}{\partial x} & 0 & 0 \\ 0 & \frac{\partial}{\partial y} & 0 \\ 0 & 0 & \frac{\partial}{\partial z} \\ \frac{\partial}{\partial y} & \frac{\partial}{\partial x} & 0 \\ \frac{\partial}{\partial z} & 0 & \frac{\partial}{\partial x} \\ 0 & \frac{\partial}{\partial z} & \frac{\partial}{\partial y} \end{bmatrix} \begin{bmatrix} u^j \\ v^j \\ w^j \end{bmatrix} = \nabla \vec{u}^{j} = \nabla \mathbf{N}^j \bar{\vec{u}}^{j}. \tag{3.4}$$

Substituting $\vec{\epsilon}^{j}$ in Equation (3.3) into Equation (3.4), we then derive the relation, $\vec{\sigma}^{j} = \mathbf{K}^j \nabla \mathbf{N}^j \bar{\vec{u}}^{j}$.

Now, we can replace all vectors in Equation (3.2) with that for the j^{th} element. Here, Π is given as $\mathbf{N}^{jT}$. Then, the structural equation for the j^{th} element is derived as

$$\iiint_{V^j} \mathbf{N}^{jT} \nabla^T (\mathbf{K}^j \nabla \mathbf{N}^j) \bar{\vec{u}}^{j} dV^j + \iiint_{V^j} \mathbf{N}^{jT} \rho^j \mathbf{N}^j \bar{\vec{b}}^{j} dV^j = 0 \tag{3.5}$$

Using the partial integral, we redefine the left-hand term as described in the below.

$$\iiint_{V^j} \mathbf{N}^{jT} \nabla^T (\mathbf{K}^j \nabla \mathbf{N}^j) \bar{\vec{u}}^{j} dV^j = - \iiint_{V^j} (\nabla \mathbf{N}^j)^T \mathbf{K}^j (\nabla \mathbf{N}^j) \bar{\vec{u}}^{j}) dV^j \tag{3.6}$$

Then we finally derive the structural equation at the j^{th} element.

$$\iiint_{V^j} (\nabla \mathbf{N}^j)^T \mathbf{K}^j (\nabla \mathbf{N}^j) \bar{\vec{u}}^{j}) dV^j = \iiint_{V^j} \mathbf{N}^{jT} \rho^j \mathbf{N}^j \bar{\vec{b}}^{j} dV^j \tag{3.7}$$

The next step is to incorporate all the structural equations for each element into the entire body. The summation of j^{th} elements at j = 1,2,...,n_e, where n_e is the total number of elements in the FEM mesh, is defined as

$$\iiint_{V} f dV = \sum_{j=1}^{n_e} \iiint_{V^j} f dV^j \tag{3.8}$$

where f is an arbitrary function. Now we finally obtain the structural equation applicable to the four-node tetrahedral FEM mesh as the below.

$$\sum_{j=1}^{n_e} \iiint_{V^j} (\nabla \mathbf{N}^j)^T \mathbf{K}^j (\nabla \mathbf{N}^j)) dV^j \bar{\vec{u}} = \sum_{j=1}^{n_e} \iiint_{V^j} \mathbf{N}^{jT} \rho^j \mathbf{N}^j dV^j \bar{\vec{b}} \tag{3.9}$$

For simplicity, we further define Equation (3.9) as

$$\chi \bar{\vec{u}} = \Psi \bar{\vec{b}} \tag{3.10}$$

where χ and Ψ are sparse matrix driven by

$$\chi = \sum_{j=1}^{n_e} \iiint_{V^j} (\nabla \mathbf{N}^j)^T \mathbf{K}^j (\nabla \mathbf{N}^j)) dV^j \tag{3.11}$$

$$\Psi = \sum_{j=1}^{n_e} \iiint_{V^j} \rho^j \mathbf{N}^{jT} \mathbf{N}^j dV^j \tag{3.12}$$

The measured stress fields using this FEM is validated by comparing the simple case with the theoretically-computed one given the same condition (Figure 3.1).

3.1.1 Boundary conditions

To solve the linear system in Equation (3.10) with respect to the displacement, we need to estimate the inverse of Φ, which is possible to cause singularity issues. We thus apply a proper boundary condition to our problem and then use an iterative conjugate gradient algorithm for the least-squares method to mitigate any singularity issues. For the boundary condition, we set the displacement at the center of mass (COM) of the body as zeros in any case. This boundary condition restricts any translational motions of the body able to be caused by loading. However, even if we apply this boundary condition, Φ is still a singular matrix, and thus we further need a mitigation process to reduce errors. For this, we adopt an iterative conjugate gradient approach for the least-square problem [e.g. [111]] that is an efficient approach to solve the linear system with a large sparse matrix. It provides a unique solution by estimating the case when a residual is converged. The usage of this technique takes advantage when the Φ is a large and sparse matrix applicable to our current problem. Adopting this approach, we confirm that the residual is converged less than $\sim 10^{-17}$, which is negligible.

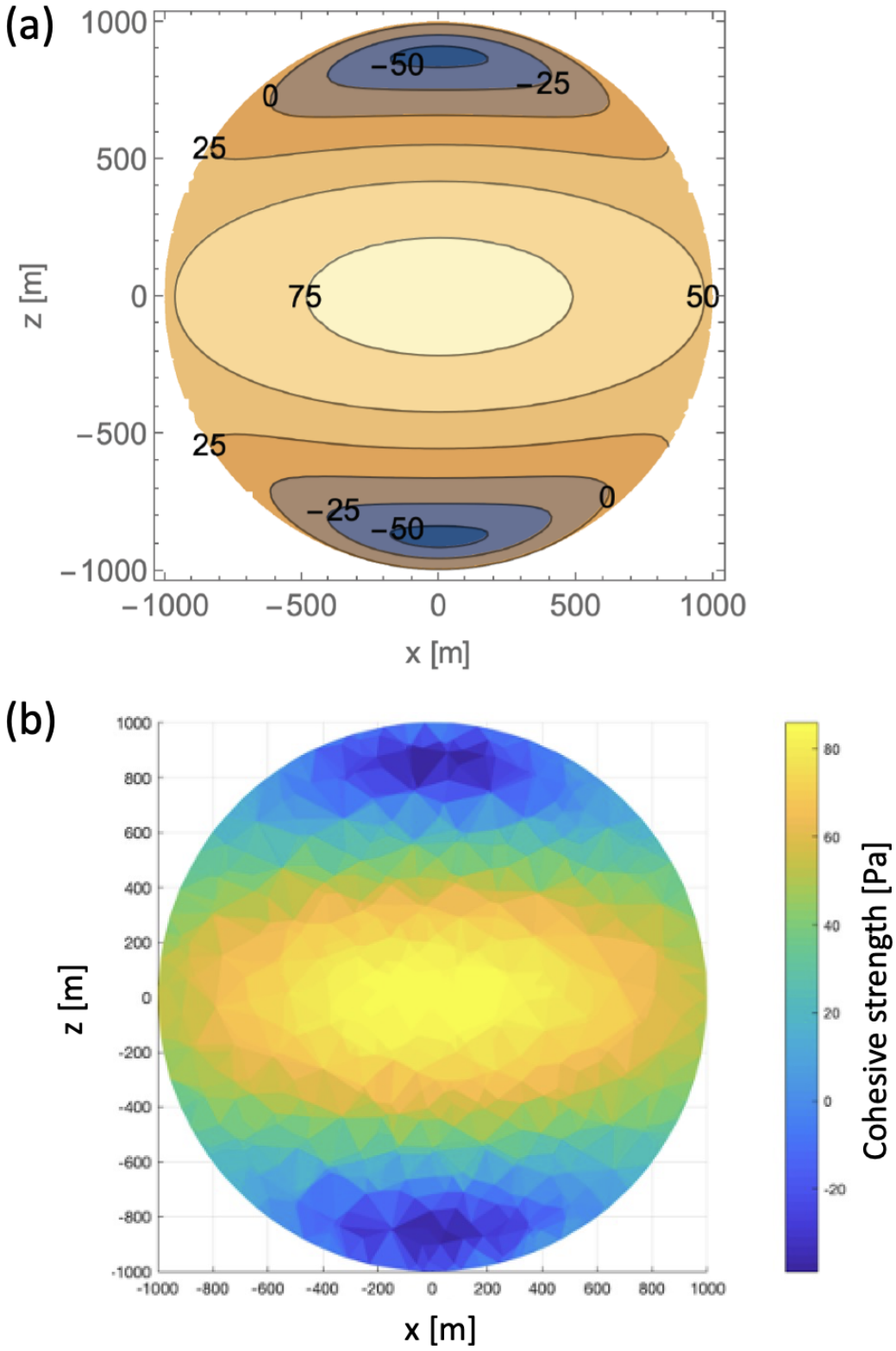

Figure 3.1: Validation of the FEM result using an analytical approach. Panel (a) shows the minimum cohesive strength distribution in a spherical body derived by a semi-analytical model [2], while panel (b) shows the FEM result. The maximum cohesive strength reaches ∼80 Pa at the most inside the object, which can be measurable in both approaches. Here, the used spherical body has a 1 km radius.

3.2 Case study: 1998 KY26

3.2.1 Research background

This case study explores the asteroid 1998 KY26, which is selected as a new target of the Hayabusa2 extended mission [112]. JAXA launched Hayabusa2 in December 2014 with the objective of (162173) Ryugu's sample return, performed the initially planned missions, and successfully released the reentry capsule on Earth. After the flawless mission completion, the Hayabusa2 is ready to explore Asteroid 1998 KY26 [112], classified as a near-Earth object. 1998 KY26 is inferred to be composed of carbonaceous materials and mafic silicates because of its dark surface [3]. The noticeable features of this object are its tiny size and rapid spin period. This object has a spherical shape with a size of 20 – 40 m, and the spin period is estimated at $\sim$10 min [3]. Given the size and rapid spin period, 1998 KY26 has long been considered a monolithic structure, not a rubble-pile asteroid commonly observable in the main asteroid belt such as Itokawa, Ryugu, and Bennu [56, 101, 113].

The primary goal of this study is to revisit the question of whether 1998 KY26 can endure the fast spin period, although it is a rubble-pile asteroid. For this, we investigate the stress level of 1998 KY26 and measure the minimum cohesive strength level required for 1998 KY26 to keep its shape. By comparing the strength level to other asteroids, we further discuss whether 1998 KY26 can still be a rubble pile asteroid despite its fast spin period.

3.2.2 FEM Simulation: 1998 KY26

We use the developed FEM (Section 3.1) to measure the stress fields of 1998 KY26. As a short reminder, the FEM computes the stress distribution of an irregular shape object given its bulk density, spin period, and shape based on linear-elastic deformation. For the FEM mesh representing the 1998 KY26's shape, we develop a 4-node tetrahedral mesh using the Doppler based shape model [3] (see Figure 3.2). As a mesh generator, we use Gmsh [114]. Figure 3.3 shows the final mesh for a surface and and slice of the object. This consists of 4599 nodes and 20,774 elements. For the setting of physical parameters, the bulk density is set to be 2800 kg/m3, which is estimated based on the optical and ground radar observations [3]. In the FEM

simulation, Poisson's ratio and Young's modulus are set to be 0.25 and 10^7 Pa, respectively. Here, 1998 KY26 is assumed to rotate along with one of the principal axes (Z-axis in Figure 3.3) with a constant spin period of 10 mins. The derived stress field is converted to the critical cohesive strength (Y^*) using the Drucker-Prager yield condition [115] derived as follow:

$$Y^* = \frac{\sqrt{3}(3 - \sin\phi)}{6\cos\phi}\left(\alpha I_1 + \sqrt{J_2}\right). \tag{3.13}$$

Here, I_1 and J_2 are the stress invariants and are expressed as

$$I_1 = \sigma_1 + \sigma_2 + \sigma_3, \tag{3.14}$$

$$J_2 = \frac{1}{6}\{(\sigma_1 - \sigma_2)^2 + (\sigma_2 - \sigma_3)^2 + (\sigma_3 - \sigma_1)^2\}, \tag{3.15}$$

where σ_i ($i = 1, 2, 3$) is the principal stress component. In Equation 3.13, ϕ and α are a friction angle and a material constant, respectively. The friction angle is set as 35°, which is a typical value of granular materials [116]. The material constant, α, is computed as

$$\alpha = \frac{2\sin\phi}{\sqrt{3}(3 - \sin\phi)}. \tag{3.16}$$

The critical cohesive strength (Y^*) defines the minimum strength level required for the object to avoid any structural failures.

3.2.3 Results and discussions

Figures 3.4 and 3.5 show the minimum level of cohesive strength at 1998 KY26's surface and interior structure. The minimum cohesive strength on the most of surface regions is less than $\sim$6 Pa, while some locations reach up to $\sim$12 Pa. The internal region requires a cohesive strength of $\sim$18 Pa. The cohesive strength is well distributed around the center of mass because of the sphere-like shape of this body.

In general, fast-rotating rubble-pile asteroids that exceed the spin limit of 2.3 h are subject to structurally break up due to the strong centrifugal force [117]. Thus, 1998 KY26 is also

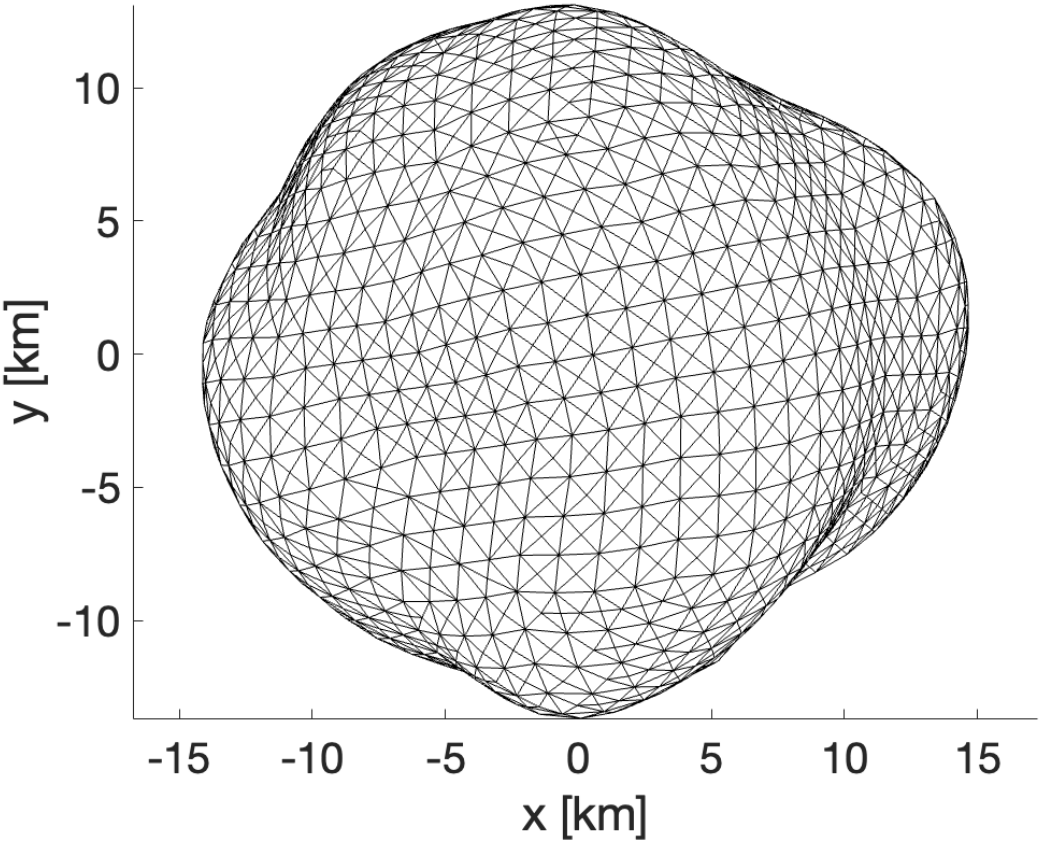

Figure 3.2: Surface mesh of 1996 KY26's shape model derived by [3]. This surface mesh consists of 4,092 facets 4599 vertices

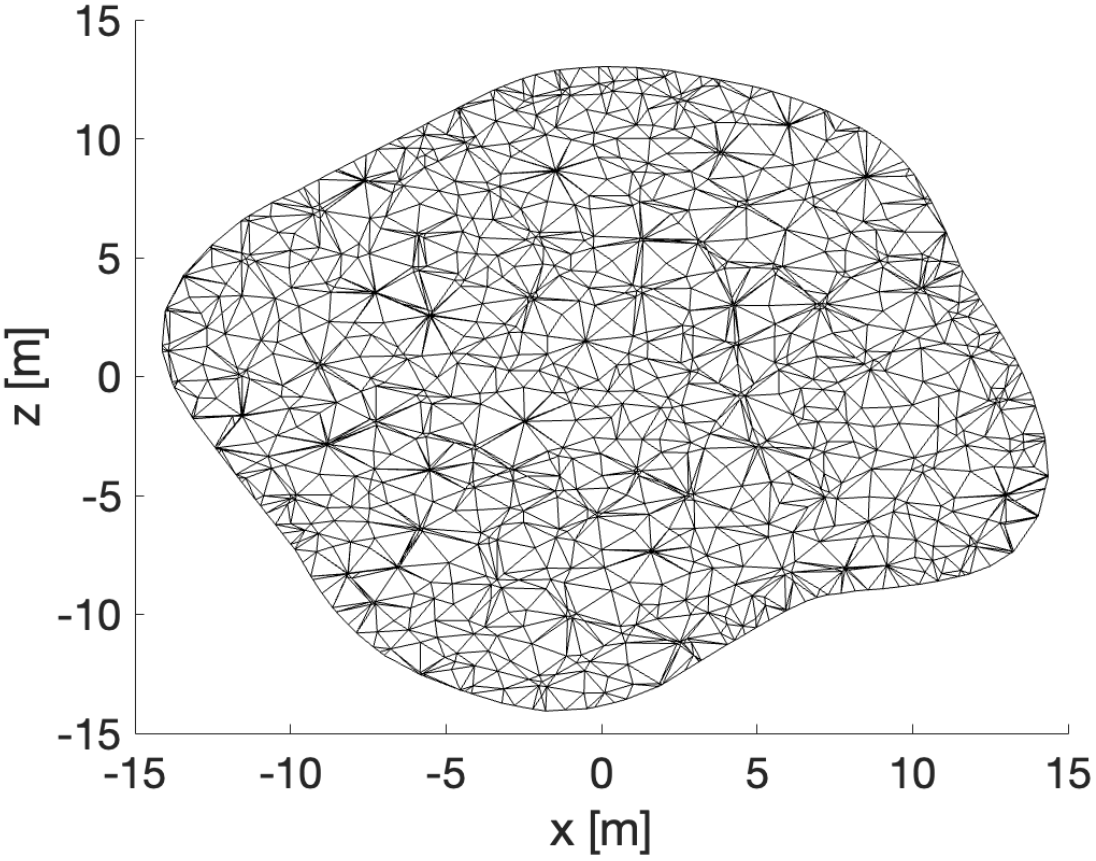

Figure 3.3: A slice of the 4-node tetrahedral mesh of 1996 KY26 using the Doppler based shape model by [3]. This structural mesh consists of 4599 nodes and 20,774 elements.

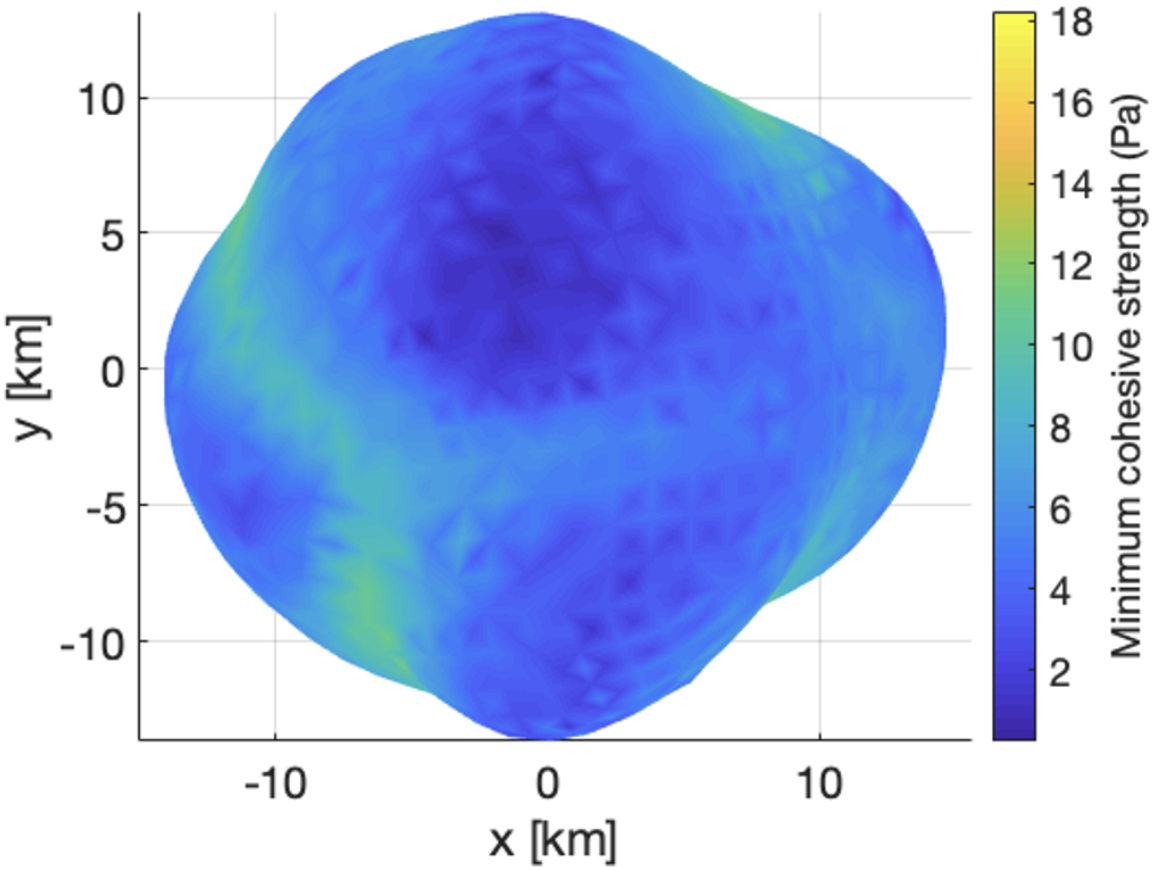

Figure 3.4: The minimum cohesive strength of the surface of KY26. The developed FEM computes the stress distribution of KY26 based on linear-elastic deformation. We then convert the stress field to the minimum cohesive strength using the Drucker-Prager yield condition.

considered a monolithic system, not a rubble pile, to sustain stable structural conditions. However, the minimum cohesive strength of 1998 KY26 reaches less than 20 Pa, which is lower than that of typical rubble pile bodies ($\sim$150 Pa – 200 Pa) [118]. Furthermore, this value is still less than that of a few fast-rotating rubble piles such as (29075) 1950 DA. The cohesive level of (29075) 1950 DA is measured to be $\sim$44 Pa [119]. Therefore, even if 1998 KY26 is a rubble-pile asteroid, the strength level of a few pascals is still a reasonable value observable in the main asteroid belt. This result indicates that 1998 KY26 can sustain the current shape regardless of a monolith structure or a rubble-pile system. The Hayabusa2 extended mission will eventually provide more detailed information on geological and geophysical conditions for this body.

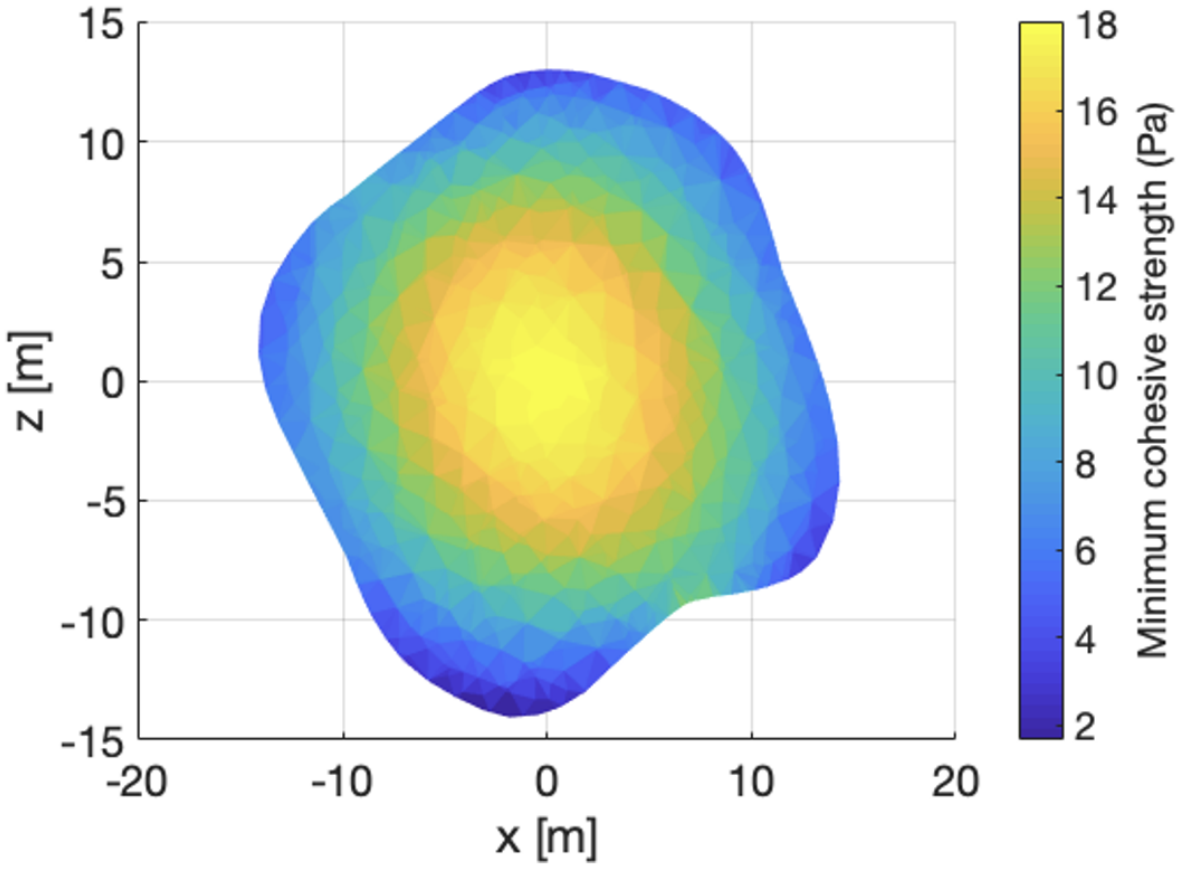

Figure 3.5: The Minimum cohesive strength of the internal structure of KY26. Here, the z-axis represents KY26's spin axis. The developed FEM computes the stress distribution of KY26 based on linear-elastic deformation. We then convert the stress field to the minimum cohesive strength using the Drucker-Prager yield condition.

3.3 Case study: (16) Psyche

The primary goal of this case study is to investigate the interior layout distribution assumed that Psyche is differentiated and constrain structural conditions consistent with the observed features. In Section 3.3.2, we describe how to develop an inverse problem algorithm to constrain the interior layout distribution of Psyche using the Three-layer model and FEM technique. The Three-layer model represents the structure of Psyche that consists of the iron core, the compressed layer, and the top surface layer. The FEM technique, described in Section 3.1, provides pressure distribution of the Three-layer model for structural analysis of Psyche. Section 3.3.3 provides results obtained from the performed simulations, and in Section 3.3.4, the results are discussed, mainly focusing on structural conditions that induce metal excavation via impact cratering process and ferrovolcanism. Finally, we argue the limitations that we noticed while using our current techniques in Section 3.3.5 and summarize our findings from this work in Section 3.3.6.

3.3.1 Research background

Asteroid (16) Psyche is one of the largest M-type asteroids with a size of $\sim$250 km in the main asteroid belt. The object has long been discussed as a remnant of the iron core from an early planet [120, 121, 122, 123, 124] and thus considered a unique relic originated from a differentiated planetesimal that can provide insights into the following questions about the formation of our Solar System: how an early planet has formed and evolved and where iron meteorites originated. To explore this object, NASA selected it as a target of its Discovery mission [6, 125] with a main scientific objective of determining whether Psyche is a core from a differentiated body [126, 127].

After Psyche was detected, the planetary science community dominantly thought that this body is a pure-metallic body [128, 129, 130] because the observations measured significantly higher radar albedo ($\sim$0.37) than other main-belt asteroids, commonly S- and C- types (0.14 - 0.15) [130]. However,if the asteroid is a pure metal or dominantly metal-rich object, the most puzzling physical parameter is its bulk density. While the density of iron meteorites is

$\sim$7.5 g cm^{-3} [131], the recent estimates of the Psyche's bulk density are all close to $\sim$4.0 g cm^{-3} [132, 133, 134, 135, 4, 136, 6], which is remarkably lower than the expected value. This inconsistency may be understandable if Psyche is a rubble-pile asteroid having a very high porosity ($> \sim$50%). Also, [137] recently indicated that Psyche might be difficult to reconcile with a fully metallic structure by showing that high porosity ($\sim$40%) cannot be sustainable due to the porosity removal by thermal evolution. They found that a Psyche-sized body must cool down below 800 K prior to porosity-adding events (i.e., disruptive impacts) to persist the sufficient porosity ($\sim$40%) until the present. However, the required timescale to cool down below 800 K (100s of Myr) is not compatible with the disruptive impacts (i.e., hit-and-run collisions [138]), which are most likely to have occurred within a few million years ($<$10 Myr) post-CAI formation [126], although some studies of planet formation suggested that hit-and-runs might have occurred for 100s of Myr in the solar system (e.g., [139, 140]). If the pure-metallic structure with high porosity is not the case for Psyche, we may interpret that this object has mixed silicates and metal. [141, 4] showed that radar albedo has significant variations across the entire surface as Psyche rotates. While the highest albedo follows that of M-type asteroids, the lowest value ($\sim$0.2) is within the high radar albedo ranges of S- and C-type asteroids. This variation indicates that Psyche does not have a constant composition across the surface. The recent works (e.g., [4] and [142]) also support this conclusion. In addition, [143] and [144] showed the presence of orthopyroxene and hydrated silicates on the surface although they do not provide strong constraints on abundances of silicates. In advance, Psyche's thermal emission observations can support the existence of a silicate layer but still do not constrain its abundance. In terms of the thermal inertia, there were three findings: $100 - 150$ J m^{-2} s$^{1/2}$ K^{-1} by [145], $5 - 25$ J m^{-2} s$^{1/2}$ K^{-1} by [146], and $180 - 380$ J m^{-2} s$^{1/2}$ K^{-1} by [147]. Since high thermal inertia generally indicate the abundance of metallic contents, [145] and [147] interpreted their measurements as the surface of Psyche contains abundant metal contents. Conversely, [146] obtained a considerably lower value of thermal inertia that indicates the surface is highly likely to be covered with fine-grained silicates. The most recent work, [147], derived the spatially resolved thermal emission measurements further to discuss the possible compositions for Psyche's surface. This study concluded that the pure silicate and

pure metal are unlikely for the Psyche's surface composition. Instead, the metal content would exist at least 20% on the surface.

Given that Psyche has metallic and silicate-rich components, a few scenarios are possible for its formation process. If Psyche originates from a differentiated planetesimal, it could be a fragmented remnant of the core with not an entirely stripped silicate layer [148, 149]. [149] performed numerical hydrocode simulations showing that proto-Mercury could remove its mantle layer via high-speed collisions with a larger target body that can support Psyche being a relic of inefficient accretion. With the assumption that Psyche is a differentiated silicate-iron body, the ferrovolcanic surface eruption proposed by [150] and [127] is also applicable to explain potential high metal-rich components on the surface. Depending on whether the iron core includes sulfur-rich contents and the thickness of the silicate layer, Psyche might experience ferrovolcanism that erupted metallic components in the iron core onto the surface [127]. The recent radar observation analysis by [4] suggested that Psyche could be a differentiated object containing the surface layer with a regolith composed of similar enstatite or CH/CB chondrites and localized high metal concentration. They picked ferrovolcanism as the most credible formation mechanism, although an impact cratering process might cause the localized metal concentration at crater-like regions. Lastly, we address that it is still possible that Psyche might come from an unmelted/undifferentiated body. The meteorite having the best-fit density of Psyche is the CB Chondrites [151] known as the most primitive meteorite group. However, if the primordial body is the case for Psyche, this interpretation raises questions about this body's origin [6]. Furthermore, it is also questionable that its surface can induce the significant radar albedo variations detected in [141, 4]. Given that both scenarios for the differentiated and primordial structure are similarly possible, this study adopts the former as the working assumption and investigates the interior condition of the differentiated Psyche.

The data currently available for Psyche is still not enough to provide details on its interior. We thus refer to the structural condition of some small bodies that can provide insights. Most small-sized objects between $\sim$200 m to 10 km are dominantly rubble piles - gravitational aggregates - as seen in Itokawa ($\sim$330 m in diameter) [56], Ryugu ($\sim$870 m in diameter) [101],

and Bennu ($\sim$480 m in diameter) [152]. If the object is much more tiny (less than a few hundreds or tens of meters), it is likely to be monolithic or strength-dominated body. Rather, the bigger sized object ($>$ tens of kilometers) is more likely to be shattered body whose structure is intact but fractured - as seen in Eros ($\sim$34 km in diameter), Gaspra ($\sim$12 km in diameter), and Ida ($\sim$32 km in diameter). For the larger asteroids ($>\sim$100 km), the one such as Vesta ($\sim$500 km in diameter) has a structure differentiated into the core, mantle, and crust [153]. Although it is unable to constrain where Psyche is subgrouped, we expect this asteroid might be in the transition between shattered and differentiated body only considering its size ($\sim$250 km in diameter).

In this case study, we model the structure of Psyche as layered by assuming that Psyche could originate from a differentiated planetesimal. The identical interior layout is a metallic core covered with a silicate-rich layer. With the assumption that the metallic core is spherical and the silicate-rich layer (later separated into two types: dense and less dense ones) overlays it, we numerically investigated the layer distribution (i.e., the size of iron core and thickness of the silicate-rich layer) by considering reasonable geophysical conditions on each layer. For this, we developed an inverse problem algorithm using a Finite Element Model (FEM) that provides stress fields of Psyche's structure by accounting for its density variations and pressure-based crushing limit in the silicate-rich layer. Our study eventually indicated that Psyche is still eligible to expose the metallic components in crater-like regions via an impact cratering process or experience ferrovolcanism in localized regions when the differentiated Psyche with the spherical core shape has a certain amount of silicates compatible with the reported bulk density of 4.0 g cm^{-3}.

3.3.1.1 Compaction mechanism in the silicate-rich layer

If the iron-core covered with the silicate-rich layer is the case for Psyche, the silicate-rich layer is likely to be compressed under high-pressure. When high pressure is applied, grains could be crushed, resulting in a more compact configuration. Earlier work (e.g., [154, 155, 156]) described that, in the case of silicate grains, the grain fracture begins when the applied pressure exceeds $\sim$10 MPa. Especially for Psyche, the first few sub kilometers from the surface reach

this crushing limit ($\sim$10 MPa). This allows the subsurface to hold lower porosity than the top surface layer. [157] conducted one-dimensional compression tests using a discrete element method (DEM) model to study the particle breakage effect in silica sands. The simulations were set with the particle size ranging from 1.4 to 1.7 mm and a grain density of 2.6 g cm^{-3}, which is compatible density with the silicate layer of Psyche although we cannot constrain grain sizes yet. Their work demonstrated three stages in the compaction mechanism. The first stage is when the grains exceed the yield point ($\sim$10 MPa) but less than the maximum compression index ($\sim$20 MPa). In this stage, the particles start to be rearranged and the limited number of particles fractured, allowing the initial porosity to decrease up to $\sim$30$\%$. We anticipate that the silicate layer of Psyche can experience this compaction stage because of the applied pressure level. After this stage when the grains exceed the maximum compression index ($\sim$20 MPa), the number of crushed particles dramatically increases, leading to nearly 60$\%$ of the initial particles being broken and more than 60$\%$ of porosity being reduced. After porosity dramatically decreases, the particles finally approach the stabilizing stage - only 10$\%$ of the rest of particles are crushed even under the incremented loading pressure. These results are validated by comparing to previous experimental results performed by [158]. For Psyche, the pressures acting on the silicate-rich layer only range from 0 - 15 MPa, confirmed from our FEM simulation. Thus, within a few sub-kilometer, compaction is highly likely to begin by the rearrangement and breakage of a few particles as seen in the first stage in [157], although not significant compaction in very high pressure regime ($\sim$ 100 MPa) is expected.

Taking into account the compaction process on Psyche, we separate the silicate-rich layer into two parts: *a top surface layer* which does not undergo the compaction process and *a compressed surface layer* which is subject to the compaction. We set the threshold of the crushing limit as 10 MPa to differentiate those two layers. Of course, this threshold (10 MPa) is likely to be affected by grain features (i.e., grain shape, grain size distribution, and initial porosity of the structure). The initial state of grains may be critical to determine the crushing limit. From earlier studies on high-pressure compression tests of silica (e.g., [155, 159, 160]), we notice some correlations between grain properties (e.g., initial relative density, particle angularity, and

grain size distribution) and crushing behavior. However, we have hitherto insufficient information on the grain properties on the Psyche's surface, and thus it is impossible to figure out the accurate threshold of crushing limit for Psyche. Thus, we adopted the crushing limit of 10 MPa. To understand how our main result's trend depends on the threshold of the crushing limit, we further perform simulations by applying the lower and upper values of the crushing limit within the pressure region (0 - 15 MPa) in the silicate layer that is 5 MPa and 15 MPa, respectively.

3.3.1.2 Psyche shape model

Currently, five 3D shape models of Psyche are available [141, 161, 162, 135, 4]. Among them, we use the latest one by [4], which well constrained the topographic features of Psyche. Figure 3.6 shows the surface mesh of the shape model. This shape model is generated based on radar images obtained in 2005, 2015, and 2017 from the Arecibo S-band radar and in 2019 from the Atacama Large Millimeter Array, adaptive optics (AO) images in 2018 and 2019 from Keck and in 2015 and 2020 from the Very Large Telescope, and stellar occultations in 2010 and 2019. The dimension is estimated as 278 $(-4/+8)$ $\times$ 238 $(-4/+6)\times$ 171 $(-1/+5)$ in kilometers. Applying the nominal mass of 22.87 $\pm$ 0.70 $\times$ 10^{18} kg driven by [5] and [6] through the analysis of perturbations from other asteroids, [4] estimated the overall bulk density of Psyche is 4.0 ± 0.2 g cm^{-3}.

[4] assessed the major topographic features (i.e., dynamical depressions, craters, and missing mass region) found in their shape model, as well as those reported by other studies [141, 161, 162, 135], in terms of whether they truly exist in Psyche or are artifacts of observation data processing. They reported two crater-like regions at the northern and southern hemispheres each and two missing mass regions at the equatorial region with convincing evidence, although other topographic features are still uncertain to be concluded. Among them, we note the crater-like regions named Panthia and Eros [4]. Panthia is centered around longitude 300° and latitude -40° with a diameter of $\sim$90 km. [4] suggested that this region possibly has a high metal concentration because its radar albedo (> 0.4) is significantly higher than the background. This region is also detected by [135] and found to be much brighter (optically)

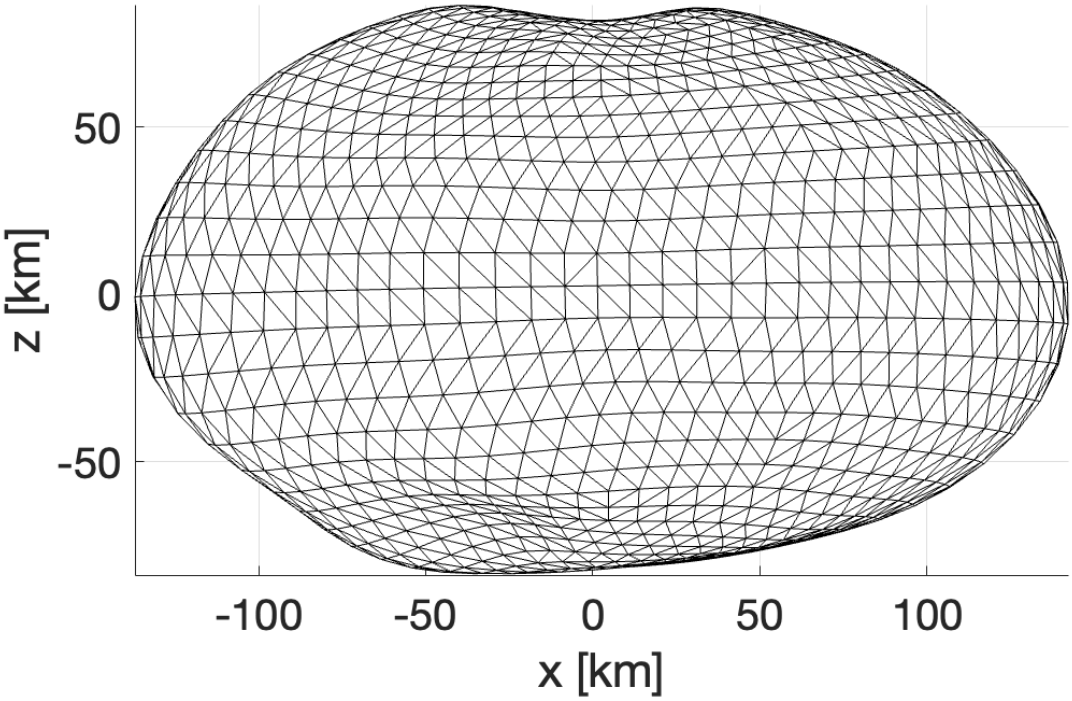

Figure 3.6: Surface mesh of Psyche's radar-derived shape model [4]. This surface mesh consists of 3,342 facets and 3344 vertices.

than the surrounded areas. If Panthia is an impact crater, we anticipate that impact cratering processes [163] likely mix the metallic materials in the core and the silicate layer to be eventually exposed on the surface at some levels. This scenario can partially explain why Panthia has the highest radar albedo, showing the localized metal concentration. Another certain crater, Eros, is located around longitude 290° and latitude -65° with a diameter between 50 and 75 km wide, which is smaller than Panthia. This area does not show high radar and optical albedos as Panthia has. However, the metal abundance in Eros cannot be ruled out because the area around Eros has bifurcated echoes suggesting multiple sources of high metal in the region [4]. Eros is within one of those higher-albedo regions and might be the source of that stronger echo (M.K. Shepard, personal communication). In our analysis, we thus consider those two crater-like regions, Panthia and Eros, and estimate the core size that is possible to reveal the metallic core onto the surface via the impact crater process, assuming that the core shape is spherical.

3.3.1.3 Dynamical environment

Psyche's spin states are well constrained from earlier works (e.g., [162, 164, 161, 141, 4]) that showed all good agreements. We follow the estimates from [4]. The spin period is $\sim$4.2 h with a spin pole at longitude 36° and latitude -8°. At present, there is no evidence indicating that Psyche is likely to be a non-principal axis rotator. Instead, given its large size and fast spin period, it is reasonable to consider that this body has a principal rotation behavior [165].

3.3.2 Numerical model

3.3.2.1 Three-layer model

We develop a three-layer model that represents a structure of Psyche that contains an iron core, a compressed silicate-rich layer (compressed layer), and an uncompressed silicate-rich layer (top surface layer) (see Figure 3.7). The entire shape is given by the radar-driven shape model [4]. As noted in Figure 3.7, the layouts of the iron core and the compressed layer are spherical as the compressed layer surrounds the core. The major motivation of this layer setting for the spherical layout assumption is that how the internal layers are distributed is highly unknown;

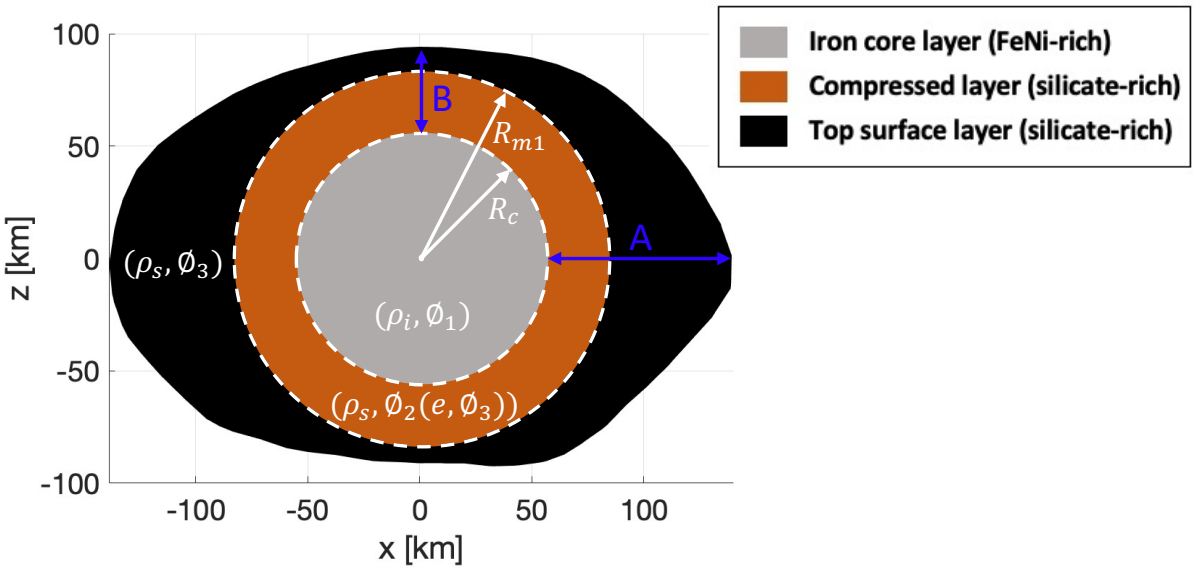

Figure 3.7: Three-layer model layout. Definitions of all symbols in the figure are described in Table 3.1.

potential issues of this assumption are discussed in Section 3.3.5 and thus subject to future investigation. The total bulk density of the structure is fixed at 4.0 g cm^{-3} consistent with the earlier works that reported the Psyche's bulk density (e.g., [6, 135, 4]). However, each layer has the different bulk density as a combination of grain density (ρ) and porosity (ϕ) depending on its composition. For example, the iron core has a denser density than the silicate-rich layer because of the abundance of metallic materials having higher grain density, and this structure is gravitationally stable. In the following section, we describe how to set the assumed ranges of grain density and porosity for each layer. The parameter setting are summarized in Table 3.2.

3.3.2.1.1 Grain density settings Grain density defines the bulk density of solid rocks that constitute the layer. In order to define this value, we refer to the bulk density of meteorites that have compositions similar to each layer. First, the silicate-rich layer is dominantly made up of silicate, consistent with the composition material of stony meteorites. Based on the meteorite data hitherto available, the bulk density of stony meteorites is well estimated between 2.5 and 3.5 g cm^{-3} [166, 132, 167]. This range is also compatible with the bulk density of an S-type asteroid ($\sim$2.0 g cm^{-3}) [56] that mostly sustains macroporosity of around 40% [64] or less. Next, the metallic core layer is composed of iron (Fe) and Nickel (Ni). The best-fit meteorite

Table 3.1: Nomenclature in Section 3.3

Symbol	Definition
R_c	Core radius
R_{m1}	Compressed layer radius
A	Minimum silicate layer thickness (lower bound)
B	Maximum silicate layer thickness (upper bound)
ρ_{bulk}	Bulk density of Psyche
V_{total}	Total volume of Psyche
V_c	Volume of an iron core layer
V_{m1}	Volume of a compressed silicate-rich layer
ρ_i	Grain density of an iron meteorite (for the iron core layer)
ρ_s	Grain density of a stony meteorite (for the silicate-rich layer)
ϕ_1	Porosity of an iron core
ϕ_2	Porosity of a compressed silicate-rich layer
ϕ_3	Porosity of a top surface layer
e	Compression rate in the silicate layer (see Equation (3.19))

Note. (*) All but R_c and R_{m1} are given parameters in our simulation.

whose mineralogy is dominated by iron and nickel is the iron meteorites. The grain density of this meteorite group depends on the Fe/Ni composition ratio (as the larger amount of Ni the meteorite has, the higher density is estimated), but be mostly distributed in the range from 7.0 to 8.0 g cm^{-3} [168, 166].

3.3.2.1.2 Porosity settings In this study, porosity defines macroporosity that measures the portion of pores in the layer. We assume that porosity is uniformly distributed in each layer for simplicity, although it may be a function of depth. This issue is discussed in Section 3.3.5. Since the porosity of Psyche is poorly known, we consider it as a free parameter within a wide range to avoid any biased structural condition depending on this value. In order to determine the applicable porosity ranges, we refer to earlier studies (e.g., [169, 170, 171]) that analyzed porosity of well-explored celestrial bodies.

For the iron core, we take into account two phases. The first phase is when the iron core was crystallized but never experienced fragmentation driven by significant impacts. If the core has not been subject to catastrophic impacts, it could sustain a relatively low porosity. [171] numerically investigated the inner core solidification process and showed porosity of the core could reach up to 5%. However, if the body has been affected by huge impacts (the second phase), it could be fragmented, causing a relatively high porosity as seen in [138]. In general,

large bodies such as Psyche may have porosity similar to lunar soils [128, 6]. The porosity range of the lunar crust is estimated to vary from 4 to 21$\%$ to the depths of a few tens of kilometers, confirmed by feldspathic rocks obtained from Apollo missions [169]. For now, it is impossible to precisely constrain the porosity range of the iron core of Psyche. Thus, we set an extensive range (0 - 30 $\%$) in simulations that can cover all ranges discussed above.

For the silicate-rich layer, we need to consider two layers - the top surface and the compressed layer. The top surface is defined as the layer where the pressure regime is less than the crushing limit (10 MPa) in our structure model. To infer the possible porosity range, we referred to the lunar crust and S-type asteroids given the similar bulk density and pressure regime with the top surface layer. Among large S-type asteroids, the well-examined object is Eros because the NEAR Shoemaker spacecraft has visited this body. The bulk density is given as 2.67 g cm^{-3} by [172], which is compatible with the determined grain density range (2.5 - 3.5 g cm^{-3}) of the silicate layer. This object is a shattered body, which means it may not be a rubble-pile but may simply be fractured, and has the bulk porosity ranging in 21$\%$ – 33$\%$ [170, 173]. We measured the central pressure of this object using a semi-analytical model, which provides elastic stress fields in a triaxial ellipsoid given its self-gravity and rotational force [2]. Figure 3.8 shows the stress field of Eros when the shape dimension is assumed to be $34.4 \times 11.2 \times 11.2$ km, and the spin period is determined to be 5.27 h with a spin axis along the shortest principal axis (z-axis). As seen in the figure, the central pressure reaches tens of kilo-pascals ($>$ 50 kPa). This pressure level is located at the top surface of Psyche, under the depth of a few meters, possibly indicating that this location could sustain the similar bulk porosity of Eros. Although Eros implies that the very top surface of Psyche possibly has a high porosity, this does not provide any constraints on the deeper surface layer. We thus further look at the lunar crust that has been investigated using high-resolution gravity data measured from the dual Gravity Recovery and Interior Laboratory (GRAIL) spacecraft [169, 174]. Earlier studies (e.g., [169] and [174]) found that the lunar crust has the bulk density of 2.55 g cm^{-3}, consistent with the top surface layer, and the average porosity of 12 - 21 $\%$ to depths up to 15 km. We perform a simple calculation to compare the pressure regime of the lunar crust and Psyche. Given the zero-pressure at the lunar surface, a pressure (P) at a certain depth (h) can be computed as $\rho_l \times g_l \times h$. Here,

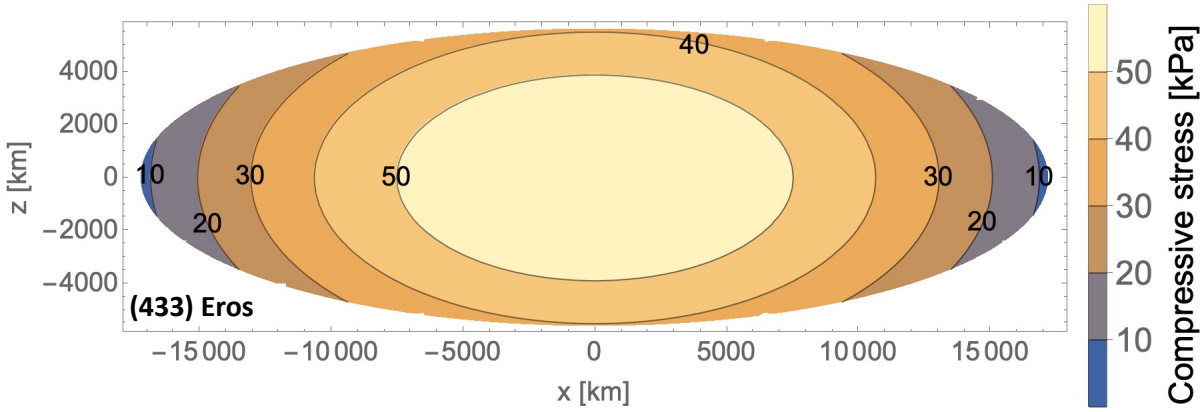

Figure 3.8: Elastic stress fields of Eros derived by a semi-analytical model [2]

ρ_l and g_l are the lunar crustal density of 2.55 g cm^{-3} and the surface gravity of 1.6 m s^{-3}, respectively. Using this relation, we figure out that the depth of 2.4 km in the lunar surface has the pressure regime that matches the top surface layer of Psyche ($<$ 10 MPa). Given that pore closure likely occurs below 15 km depth in the lunar crust [174], the top-surface layer of Psyche is still possible to sustain a similar porosity regime with the lunar crust. As a final note, it cannot be ruled out that the top surface layer of Psyche could be highly fragmented like a rubble-piles (e.g., Itokawa has bulk porosity over 40 $\%$ but a lower bulk density of 1.9 g cm^{-3} than the top surface layer) or unconsolidated terrestrial sediments asteroid by impacts and re-accumulated process. Based on this, we set the very broad range of porosity of the top surface as 10 - 50 $\%$, which covers all porosity mentioned above.

Now, we describe the porosity range applicable in the compressed silicate-rich layer. The grain density of the compressed layer is the same as that of the top surface layer, but porosity decreases, as discussed in Section 3.3.1.1. [157] numerically performed one-dimensional compression tests to study the particle breakage effect in silica sands and showed that the initial porosity decreases up to $\sim$30$\%$ at the compression pressure of 10 MPa. Given the compression rate, the porosity range of the compressed layer is set to be 7$\%$ - 35$\%$, which is the decreased range of the top silicate layer (10$\%$ - 50$\%$). However, one might question whether the 30$\%$ decrease is still significantly high to occur in the silicate layer under a low pressure regime of 10 MPa. To explore this issue, we additionally perform a simulation with a lower compression rate ($\sim$ 5$\%$) to understand how the compression rate influences the final structure layout.

Table 3.2: Geophysical parameter of each layer in the Three-layer model

Layer	ρ [gcm^{-3}]	ϕ [%]
Top silicate-rich layer	2.5 - 3.5	10 - 50
Compressed silicate-rich layer	2.5 - 3.5	7 - 35
Metal-rich layer	7.0 - 8.0	0 - 30

Note. (*) ρ represents a grain density.

3.3.2.2 Finite Element Model (FEM) Approach

We use a finite element model (FEM) to calculate the stress distribution of the layered structure of Psyche. This FEM is a modified version of the earlier model [72] to apply to the current problem for investigating a differentiated object. The major change made in the current version is considering density variations over a target body. For structural analysis, we start from the structural equation given as

$$\rho \frac{\partial^2 \vec{u}}{\partial t^2} = \nabla^T \vec{\sigma} + \rho \vec{b} \approx 0 \tag{3.17}$$

where ρ is the bulk density, $\vec{u}$ is the displacement vector that consists of [u_x, u_y, u_z], $\vec{\sigma}$ is the stress vector in the equilibrium state ($\rho \frac{\partial^2 \vec{u}}{\partial t^2} = 0$) that includes [$\sigma_{xx}$, σ_{yy}, σ_{zz}, σ_{xy}, σ_{xz}, σ_{yz}], and $\vec{b}$ is the loading vector that contains [b_x, b_y, b_z]. In the earlier model [72], ρ is considered as a constant parameter. However, in the current model, we apply the different value of ρ depending on the layers. Equation (3.17) eventually provides the stress field in the equilibrium state where the body is solely influenced by self-gravity and rotational forces. Thus, $\vec{b}$ is computed by a summation of gravity and centrifugal force. Then, the stress field is developed using Hook's principle as a constitutive law for linear elasticity. For the implementation, we expand this structural equation to a four-node tetrahedral FEM mesh that represents the structure of the target body. The detailed procedure is described in the following section.

3.3.2.2.1 FEM mesh

We develop a 4-node FEM mesh using the ground-radar driven shape model by [4]. The shape model is a surface mesh that consists of 1,652 vertices and 3,300 faces. To generate a tetrahedral volumetric mesh, we use TetGen, which is an open-source mesh generator developed by [175]. The final mesh has 3,344 nodes and 15,569 elements.

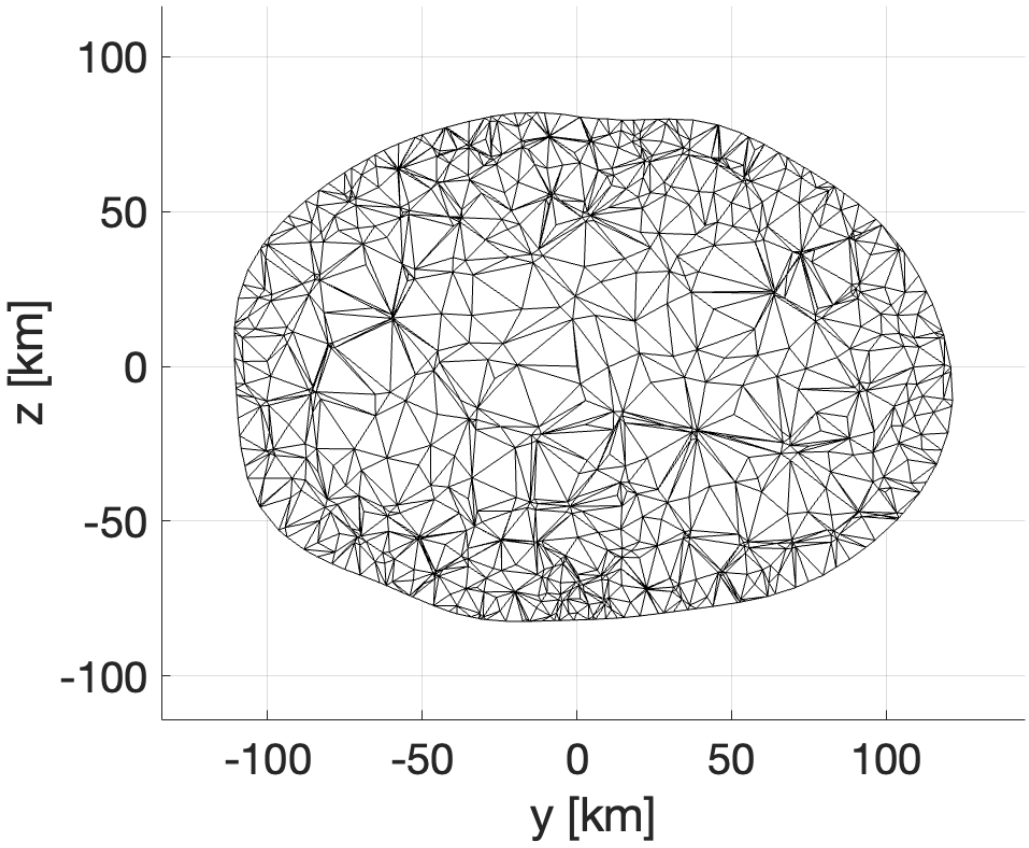

Figure 3.9: A slice of the 4-node tetrahedral mesh of Psyche using the radar-derived shape model by [4]. This structural mesh used for the FEM simulation consists of 3,344 nodes and 15,569 elements.

Figure 3.9 shows a slice of the FEM mesh, which represents the body's internal structure. We accept this mesh quality because it does not induce any stress concentration caused when using a low-quality FEM mesh. In the FEM mesh, the elements are not isotropically distributed, but the interior tends to have relatively larger elements than those close to the surface layer. However, this element distribution is still reasonable to capture the stress fields distribution because the internal region has the least variation in the stress field [72]. In other words, the inside region of the structure is not much sensitive to the volume of elements.

Table 3.3: Simulation input parameter settings

Quantity	Value/Range	Units
Young's modulus	1.0×10^7	Pa
Poisson's ratio	0.25	-
Total bulk density	4.0	g cm^{-3}
Rotation period	4.2	h
Number of nodes	3,344	-
Number of elements	15,569	-
Shape dimension	$278 \times 238 \times 171$	km

Note. (*) Young's modulus is an independent parameter of the stress solution in the linear-elastic deformation [176].

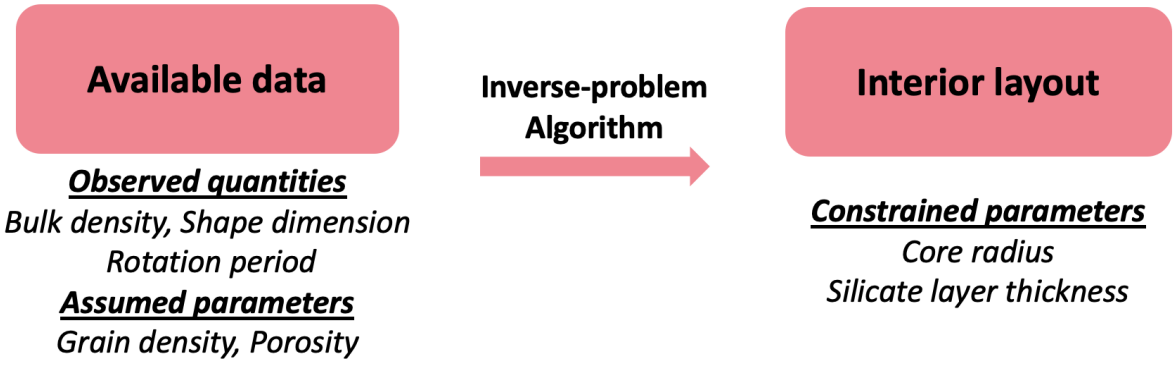

Figure 3.10: The defined inverse problem to investigate the interior layout given the currently available data on Psyche. The available data are the observed quantities, including Psyche's bulk density, shape dimension, and rotation period, and the assumed parameters, including grain densities and porosities for each layer. Given these data, We constrain the core radius and silicate layer thicknesses for the interior layout distribution.

3.3.2.3 An inverse problem algorithm for structure layout

3.3.2.3.1 Structure layout constraints in the Three-layer model

To estimate the size of the three layers (the core, the compressed, and the top surface layer), we use the geometric constraints with a constant total mass (22.87×10^{18} kg) of Psyche that induces a bulk density of 4.0 g cm^{-3} given the current shape model [5, 6, 4] (Figure 3.10 shows the concept of the defined inverse problem). We then propagate the equation of the total mass of Psyche computed by the summation of each layer's mass as follows.

$$\rho_{bulk} V_{total} = V_c(1-\phi_1)\rho_i + V_{m1}(1-\phi_2)\rho_s + (V_{total} - V_c - V_{m1})(1-\phi_3)\rho_s \tag{3.18}$$

where the variables are defined in Table 3.1. Here, ρ_{bulk}, V_{total} are observed quantities, ρ_i, ρ_s, ϕ_1 and ϕ_3 are assumed parameters. The details in the given parameter settings are described in Section 3.3.2.1.2. The rest of the parameters, including ϕ_2, V_c, and V_{m1}, are driven by the following equations.

$$\phi_2 = (1 - e)\phi_3 \tag{3.19}$$

$$V_c = \frac{4}{3}\pi {R_c}^3 \tag{3.20}$$

$$V_{m1} = \int_{R_c}^{R_{m1}} V \, dV \tag{3.21}$$

Here, ϕ_2 is computed by ϕ_3 and a compression rate (e) driven by the earlier compression tests of silica sands[157, 158]. For example, if porosity at the compressed layer reduces 30%, ϕ_2 is defined as (1 - 0.3) $\times$ ϕ_3 given e = 30 %. Equation (3.20) and (3.21) show that V_c and V_{m1} are expressed by a function of the core radius (R_c) and the compressed layer radius (R_{m1}). Thus, Equation (3.18) is expressed as a function of R_c and R_{m1}, which are free parameters in the simulation.

Figure 3.11 represents the correlation between R_c and R_{m1} (see the blue-colored line). Here, the white area is the considered region to pick a reasonable set of (R_c, R_{m1}), while the grey area is excluded. The boundary line (C1) is where the core radius is identical to the compressed silicate layer radius. The region below C1 indicates that the core is always placed below the compressed silicate layer. The upper horizontal line (C2) reflects the assumption of the spherical shape of the core. Thus, the maximum core radius is consistent with the minimum dimension (88.5 km) of Psyche along the shortest principal axis in the current shape model. Also, the line (C3) means the maximum dimension (140 km) of Psyche along the longest principal axis that the compressed layer radius cannot exceed. Based on this correlation, we can sort out possible sets of (R_c, R_{m1}) but still have many options. Thus, in order to further narrow down and determine one specific set of (R_c, R_{m1}), we incorporate our FEM technique.

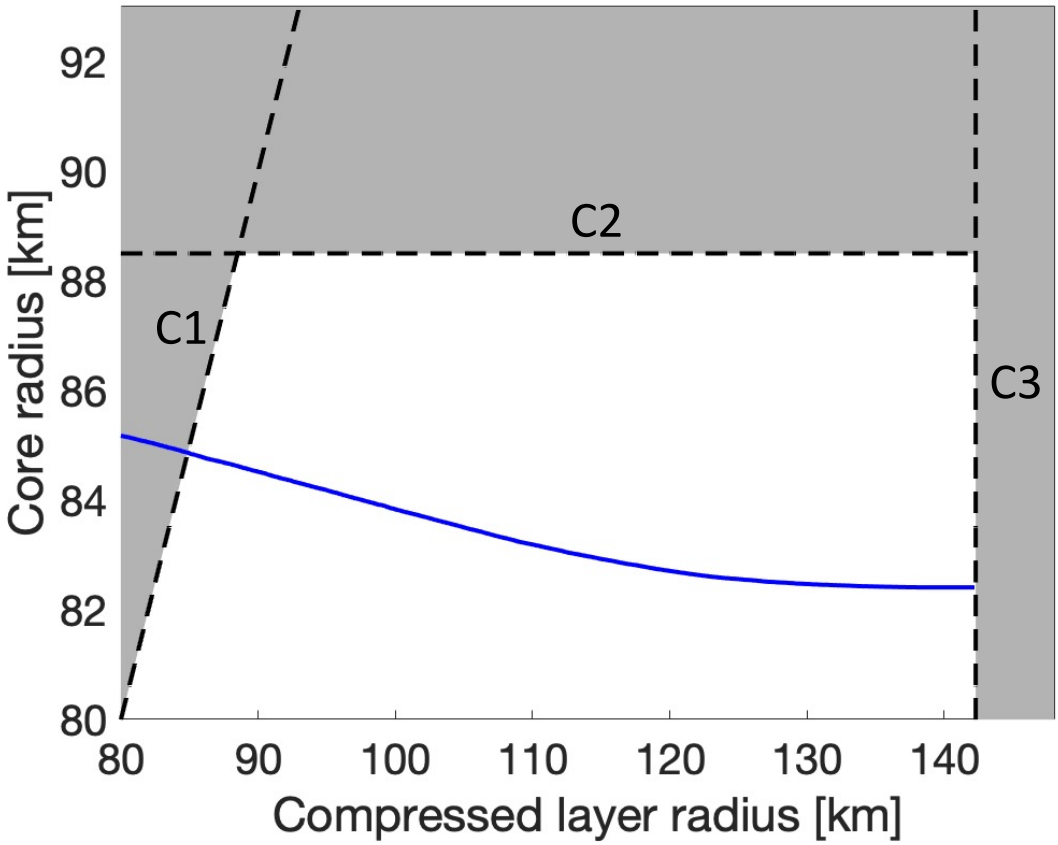

Figure 3.11: Correlation between a radius of the core (R_c) and the compressed layer (R_{m1}). The blue line represents a core radius depending on the compressed layer radius. The left dotted line (C1) is a boundary where the core radius is identical to the compressed layer. The upper horizontal line (C2) shows the minimum dimension ($\sim$88.5 km) along the shortest principal axis, while the right dotted line (C3) means the maximum dimension ($\sim$140 km) along the longest principal axis. The white area includes possible sets of (R_c, R_{m1}).

3.3.2.3.2 Structure layout constraints using FEM technique In order to find a unique structure layout at the given geophysical parameters, we adopt the condition where the compaction starts at the the threshold of the crushing limit in the silicate-rich layer. Using this condition, we can find out a unique case among the possible sets of (R_c, R_{m1}) from Equation 3.18. A numerical algorithm schematized in Figure 3.12 describes the entire process of how to constrain the final structure layout of Psyche, and the FEM technique section shows the partial process of how to find the unique case among the possible sets of (R_c, R_{m1}) using the FEM technique developed in section 3.3.2.2.

In the initial stage, we randomly select a set of (R_c, R_{m1}) among the possible ones and define it as the initial structure layout. Again, the possible sets are investigated based on the correlation between R_c and R_{m1} driven by Equation (3.18), which defines the blue curve in Figure 3.11. We then compute the pressure distribution of the initial structure using FEM when this body rotates along the spin pole with a spin period of 4.2 h [4]. After obtaining the pressure, we find the boundary line when the pressure reaches the threshold of the crushing limit in the silicate-rich layer. This boundary line indicates when the compaction process indeed starts in the given structure and must be consistent with the compressed layer. We check if the boundary line matches the compressed layer from the initial structure layout. If they do not match as seen in Figure 3.13 (a), we redefine the initial structure layout by applying another set of (R_c, R_{m1}). Usually, we use the set that has R_{m1} closer to the boundary line because this condition makes the simulation converge faster. These processes, redefining the initial structure layout and computing the pressure distribution, are reiterated until the simulation converges into a unique case that gives the boundary line matched the compressed layer. In the final stage, we export the matched case as the final structure. Figure 3.13 (b) shows the final structure layout after the simulation ends. The input parameters are given in Table 3.3 and the porosity of the iron-core and the top surface is set as 0% and 50% separately. We notice that both sets of (R_c, R_{m1}) used at the initial (Figure 3.13 (a)) and final stage (Figure 3.13 (b)) satisfy Equation (3.18) but the later one is the only case that provides the same pressure value as the crushing limit (this case, 10 MPa) at the compressed layer.

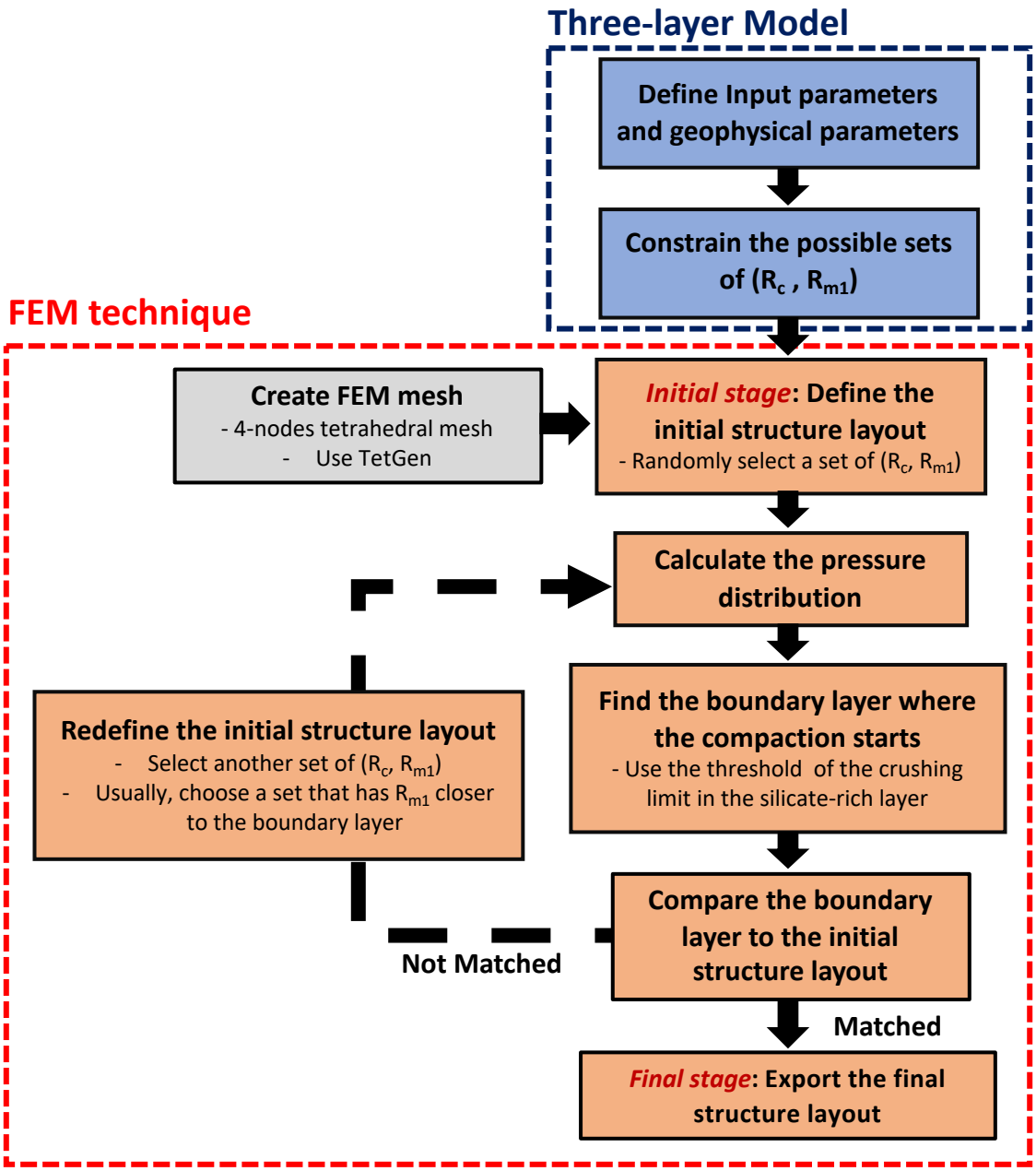

Figure 3.12: An inverse problem algorithm to constrain the structure layout using the Three-layer model and FEM technique. Currently, the bulk density and mass of Psyche have large uncertainties, although there is some supporting evidence inferring those parameters. Given this issue, we decided to fix the bulk density as 4.0 g cm^{-3}, which is the best-matched parameter from the earlier studies, in the Three-layer model. This value is estimated by [4], given the nominal mass is 22.87×10^{18} kg which is driven by [5] and [6]. The matched case is defined before the final stage when the discrepancy between the boundary line and the compressed layer from the initial structure layout is less than 0.01 km.

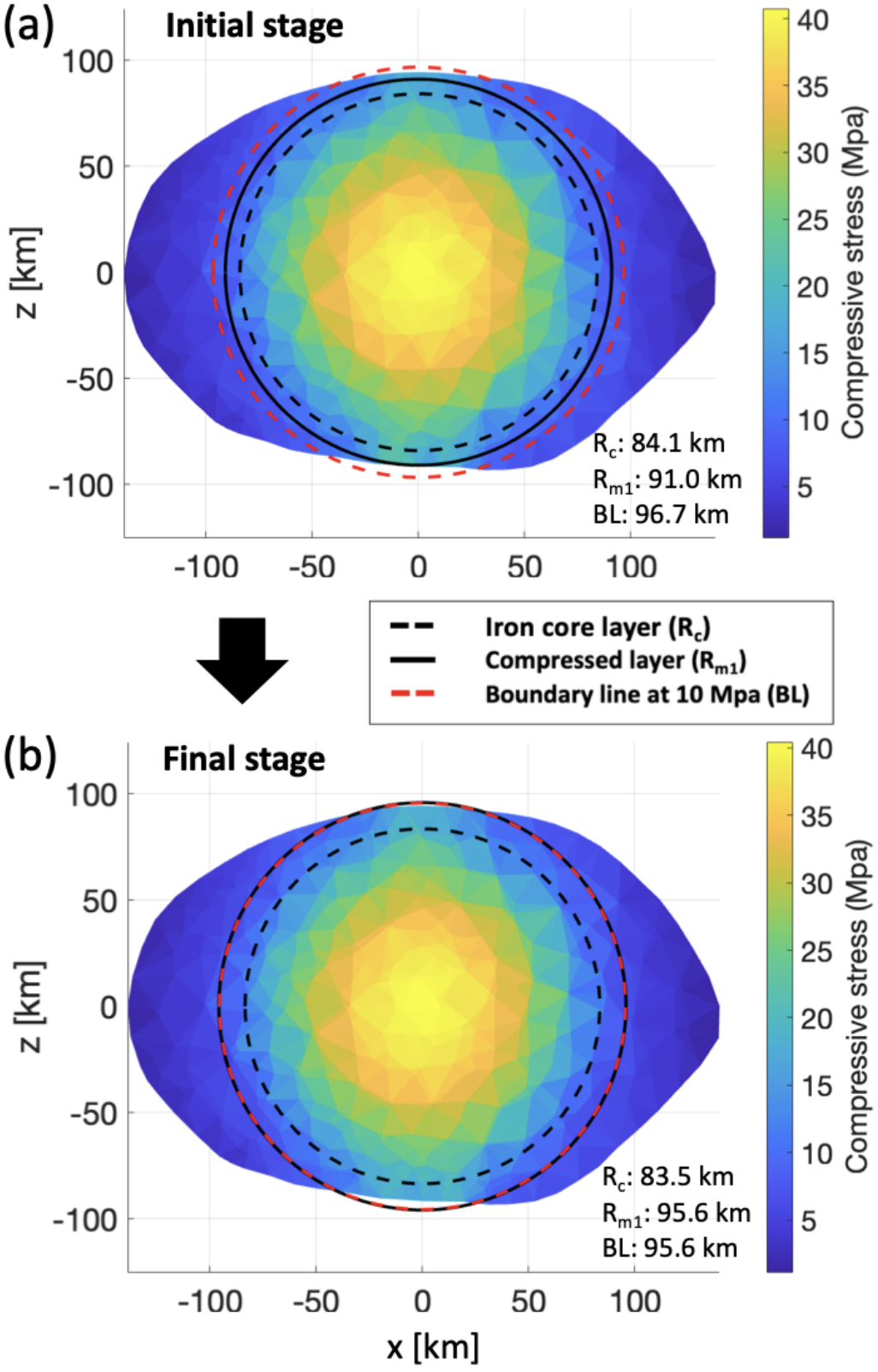

Figure 3.13: Structure layout (a) at the initial stage and (b) the final stage. Figure (b) show a unique case when the boundary line matches the crushing limit. Here, the crushing limit is set as 10 MPa. This case represents when the porosity of the iron-core and the top surface is 0% and 50% separately, given e = 30 %.

3.3.3 Results

We perform 7,500 simulations in total within the defined porosity ranges of the top surface layer and iron core with the crushing limit of 10 MPa (see Section 3.3.3.1). Different porosity results in various bulk densities, leading to different core sizes and silicate-rich layer thicknesses. To find the dependence on the crushing limit of the silicate layer, we conduct additional simulations with the same simulation conditions but adopt a different crushing limit of silicates (see Section 3.3.3.2). Lastly, we use a different compression rate (5 $\%$) in the compressed silicate layer and compare the result with the compression rate of 30 $\%$. Although we set the initial compression rate (30 $\%$) by referring to earlier studies (i.e., [158, 157]) regarding one-dimensional compression test of silica, it may be different in the environment of Psyche depending on geological features such as grain size and shape.

3.3.3.1 Constrained structure layouts of Psyche

We first introduce three simulation cases with the crushing limit of 10 MPa (see Figure 3.14). The geophysical parameter settings for those simulations are given in Table 3.4. The result shows that CASE1 has the largest core size among the three cases. Given this core size, the compressed silicate-rich layer's thickness is estimated to be $\sim$7.5 km. Compared to CASE1, CASE2 has an entirely lower porosity showing that each layer is denser. The core size is estimated to be $\sim$5 km smaller in radius, while the compressed silicate-rich layer's thickness is similar ($\sim$7.2 km). For CASE3, we set the highest porosity for the top surface layer to be the most fluffy top and the lowest porosity for the core to be the densest core. Given the condition, the core is estimated to be the smallest size, $\sim$10 km smaller than CASE1 in the radius, with the thickest compressed silicate-rich layer ($\sim$10 km). The results are also summarized in Table 3.5.

We then perform 7,500 simulations and output the constrained size of the interior layout for all cases. Figure 3.15 shows a color map representing the constrained core size in radius given the wide range of the core porosity and the top surface porosity. Here, We only consider the cases whose core sizes do not exceed the minimum dimension ($\sim$88.5 km) of the current

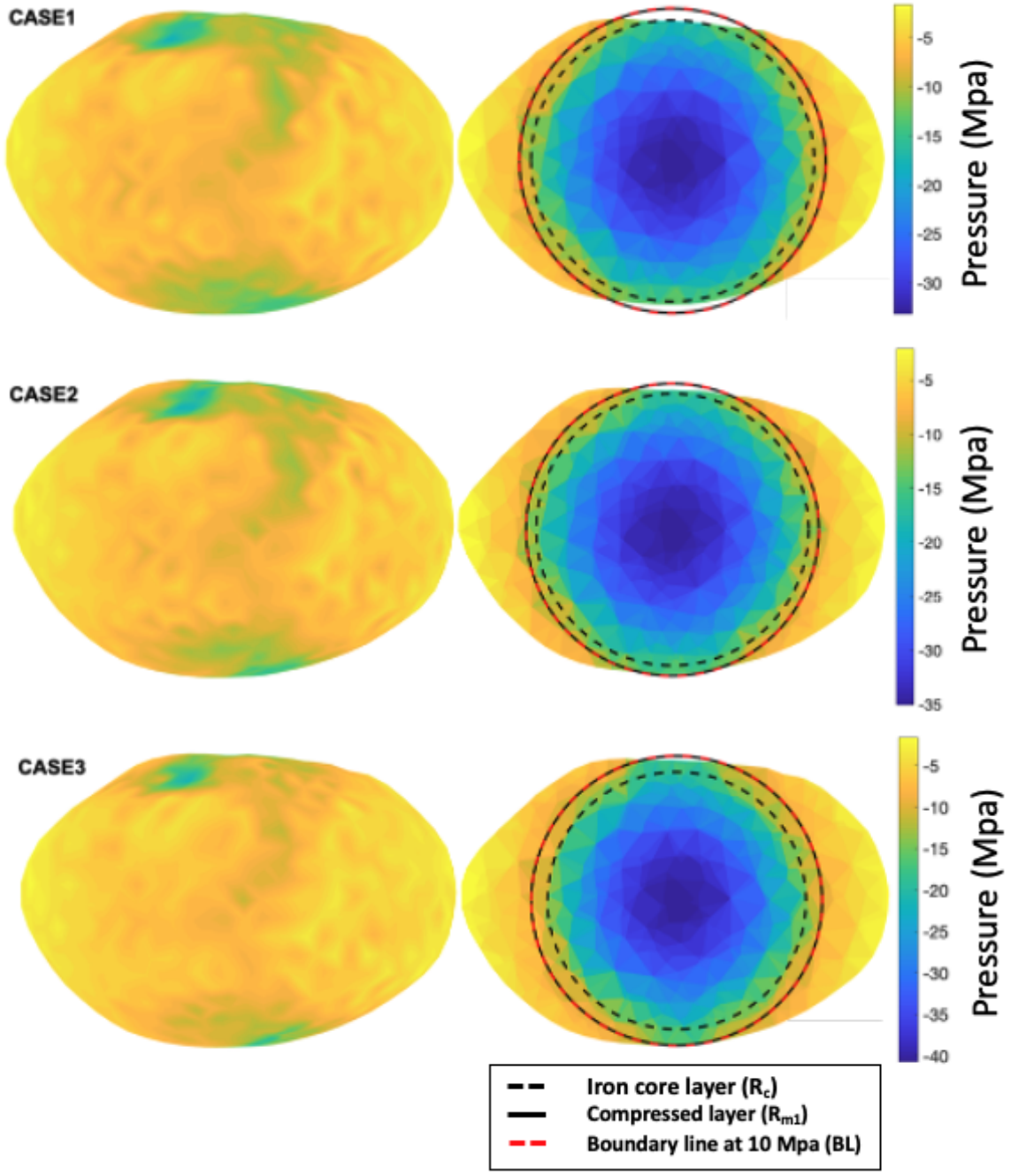

Figure 3.14: Pressure distributions of CASE1 (top), CASE2 (middle), and CASE3 (bottom). The left-side and the right-side columns show the surface and interior, respectively.

Table 3.4: Geophysical parameter settings for three simulated cases.

Geophysical parameter	CASE1	CASE2	CASE3
Grain density of the iron core [g/cm^3]	7.5	7.5	7.5
Grain density of the silicate-rich layer [g/cm^3]	3.0	3.0	3.0
Porosity of the iron core [%]	21	17	4
Porosity of the top silicate-rich layer [%]	33	27	33
Porosity of the compressed silicate-rich layer [%]	23	19	23

Table 3.5: Simulation results for three cases.

The measured value	CASE1	CASE2	CASE3
Core radius [km]	92.1024	88.7037	83.7017
Thickness of the compressed silicate-rich layer [km]	99.5975	95.3379	94.1336

shape model given the geometric constraint described in Section 3.3.2.3.1. The trend seen in the color map entirely shows the core becoming larger as the core and silicate layer has a higher porosity. The correlation between volume and density accounts for this trend. As the more highly porous structure causes the lower bulk density, this body can sustain the larger volume under the same condition of mass. In Psyche, the large core eventually induces a relatively thin silicate layer. In detail, the estimate of core size varies from 72 km to 88.5 km. This core size takes up 30 - 45 $\%$ of the overall size of Psyche. The minimum core radius is located when the core and silicate layer have the lowest porosity, specifying the densest layers. Conversely, the largest core is placed at the most porous structure. Note that the current shape model shows an elongated shape having a minimum radius of 88.5 km along the shortest principal axis pointing at the pole and a maximum radius of 140 km along the longest axis heading the equator. Given this shape model, the thickest silicate-rich crust is place at the equatorial region, while the thinnest layer is located around the polar regions (represented as A and B in Figure 3.7). Figure 3.16 shows the minimum and maximum thickness of the silicate layer that reaches $\sim$16 km and $\sim$68 km, respectively, when the structure is the densest. These minimum and maximum values can define the lower and upper limits of the silicate thickness. As a final note, we address that not all cases are converged. White pixels in the top-right corner seen in Figure 3.15 corresponded to the cases when a simulation did not converge. The non-convergence is the result of cases when the pressure in the silicate layer does not reach up to the crushing limit of 10 MPa, leading to no solution. The non-converged cases mostly occur when the core has a large porosity which is a very high upper limit for the porosity of the core, given that iron meteorites have porosity less than 10 $\%$ [177]. However, even if the overburden pressure in the silicate layer does not reach the crushing limit, this does not mean that Psyche cannot have a differentiated structure having a core and silicate layer. The structure layout is impossible to be determined in the inverse problem algorithm (Figure 3.12) because the boundary line does

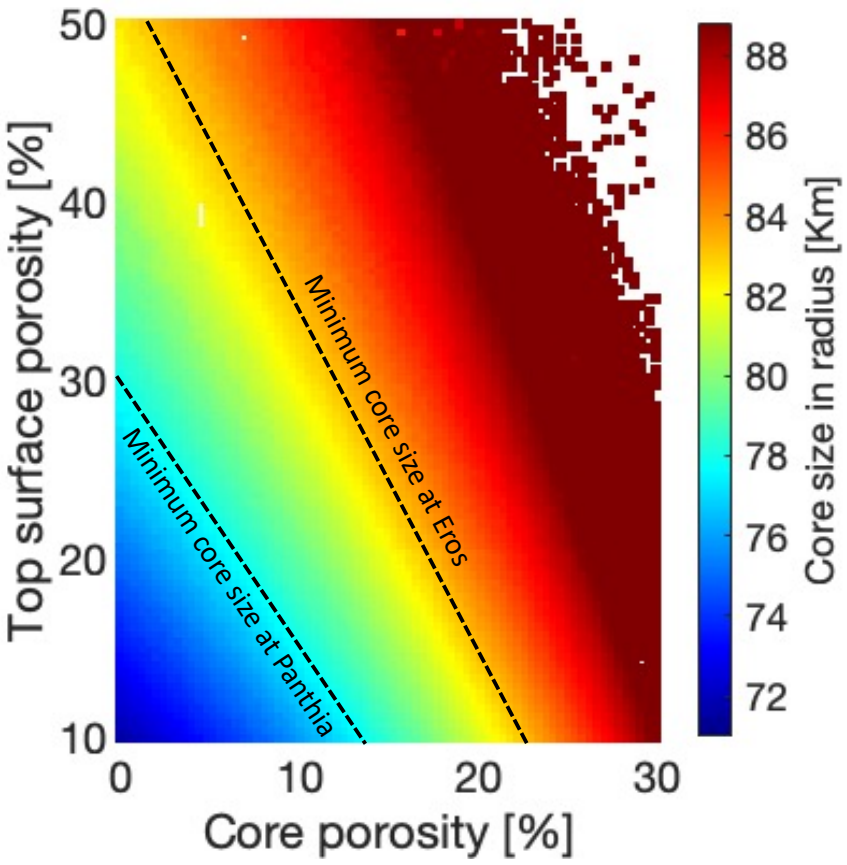

Figure 3.15: A colormap that shows the constrained core size within the possible porosity ranges. The black dotted lines define the minimum core size possible to be exposed at Panthia (Left) and Eros (Right) via an impact cratering process. In the determined porosity range, there are some cases at the bottom right corner where the porosity of the core is set to be higher than that of the overlying silicate layer. We address that this condition may not be realistic, although the composition discontinuity between the core and silicate layer may allow that porosity is not mutually related to each other.

not exist but may simply be estimated by the bulk density of the silicate and core layer, which satisfy the bulk density of 4.0 g cm^{-3} for the entire body, without considering the compaction effect.

3.3.3.2 Dependence on the crushing limit of silicate

We set the threshold of the crushing limit of silicate as 10 MPa by taking into account earlier studies (e.g., [154, 157]). However, as mentioned in Section 3.3.1.1, this threshold can be controlled by grain properties (i.e., shape, size, initial porosity) on the surface of Psyche. Thus, we select two more different thresholds within the pressure regime ($\sim$15 MPa) of the silicate

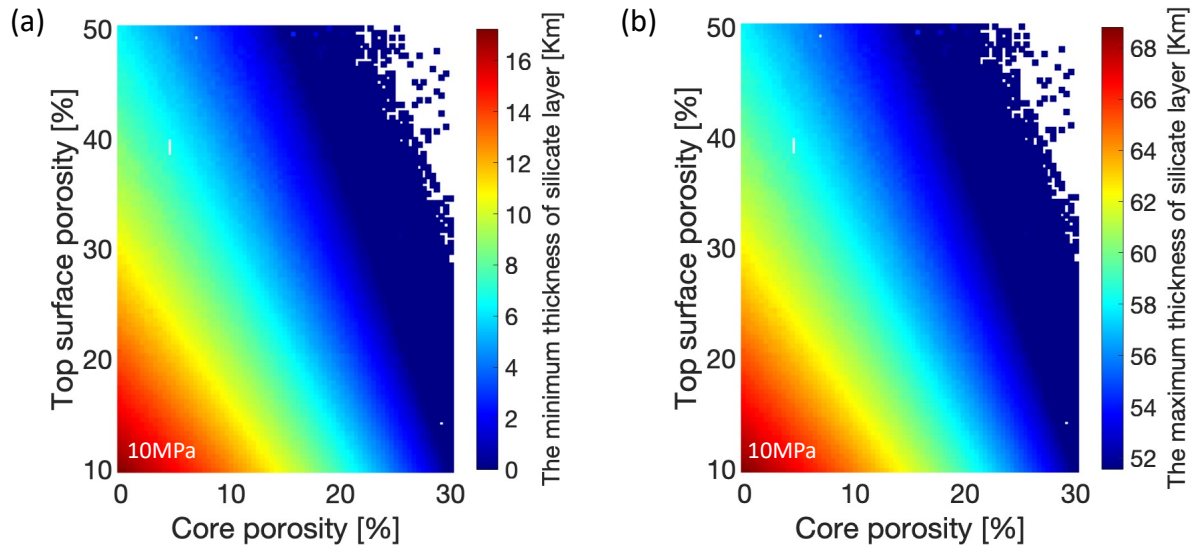

Figure 3.16: A colormap that shows the silicate-rich layer thickness: (a) The minimum thickness placed at the polar region and (b) the maximum thickness located at the equatorial region.

layer, the lower and upper values, and analyze how the trend of the core size and silicate layer thickness is affected. Figure 3.17 (a) and (b) show the core size in radius at the crushing limit of 5 MPa and 15 MPa, respectively. We first note that the 15 MPa case does not provide the solution in many simulation cases when the core size is larger than $\sim$80 km in radius, unlike the 5 MPa. This feature results from that the pressure regime in the silicate layer does not exceed 15 MPa, which is set as the crushing limit. Thus, the interior layout cannot be defined, while the 5 MPa and the 10 MPa cases find the solution under the same geophysical parameter settings. Except for the not-converging simulations, Figure 3.17 (a) and (b) capture the same trend seen in the previous section (Figure 3.15). The core size becomes larger as the structure becomes porous. However, under the same condition of porosity, the core size converged becomes slightly different depending on the crushing limit, resulting in the shifted color distribution. For example, consider the simulation result at the point where the core and top-surface porosities are given as 0% and 30%, respectively. The estimates of the core size are 76.6 km with the 5 MPa crushing limit, 77.9 km with 10 MPa, and 78.5 km with 15 MPa. With the lower crushing limit, the core size is estimated smaller. This is because compaction occurs closer to the surface in the silicate-rich layer with the lower crushing limit and thus induces the thicker compressed layer. This compressed layer has the denser bulk density due to a decrease

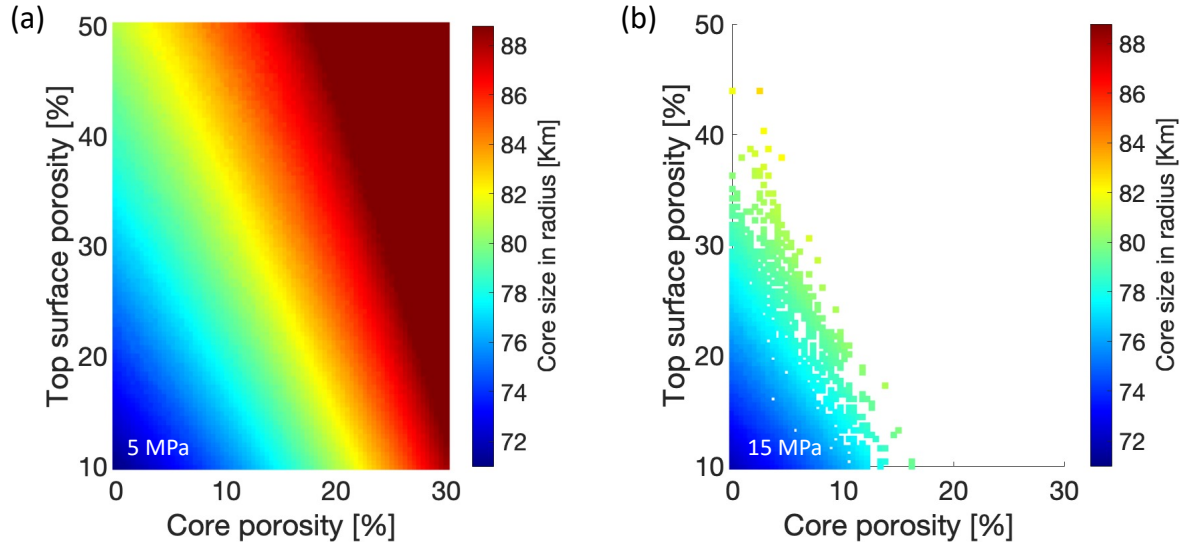

Figure 3.17: Comparison of colormaps between the crushing limit of (a) 5 MPa and (b) 15 MPa. In most cases where the core exceeds a certain size (∼80 km), the 15 MPa provides a non-colored area that represents the simulation is not converged. We interpret this area as when the pressure in the silicate layer does not approach the defined crushing limit, and thus any solution for the interior layout does not exist.

in porosity and eventually takes up a large portion of Psyche's mass. Therefore, the smaller iron core exists as the compressed layer increases. Owing to this mechanism, given the lower crushing limit of 5 MPa, the smallest core size reaches 71.0 km in radius, while the 15 MPa case gives 71.8 km. We also note that the silicate layer thickness at 5 MPa slightly increases compared to the 10 MPa and 15 MPa cases (Figure 3.18). However, only a few hundred meters are changed in the core radius, and this difference can be negligible compared to the entire Psyche size.

3.3.3.3 Dependence on the compression rate in the compressed layer

One may question how the simulation results can change if the actual case of Psyche has a more minimal compression rate in the silicate layer. To understand the dependence on the compression rate, we perform supplementary simulations with the same simulation settings in Section 3.3.3.1 but a much smaller depression rate ($\sim 5\%$). Figure 3.19 (a) and (b) show the core size at the compression rate of 30% and 5%, respectively. This result shows that there is no noticeable difference between them. This is because even the highest compression rate of 30% is still small to reduce the bulk density of the compressed layer until affecting the core size.

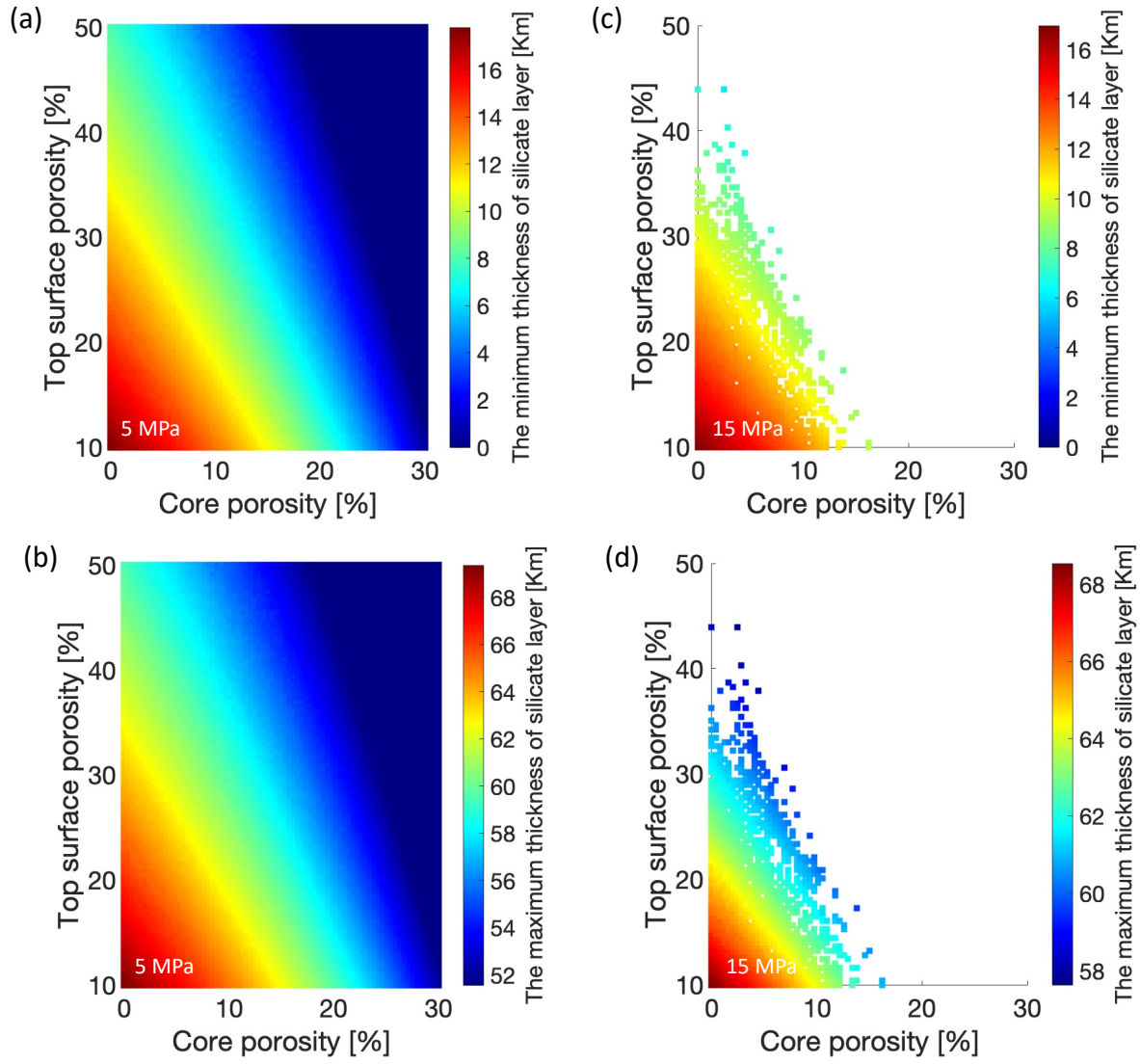

Figure 3.18: Comparison of colormaps that shows the silicate-rich layer thickness between the crushing limit of 5 MPa and 15 MPa: (a) The minimum thickness at 5 MPa, (b) the maximum thickness at 5 MPa, (c) The minimum thickness at 15 MPa, and (d) the maximum thickness at 15 MPa. As mentioned in Figure 3.17 (b), the 15 MPa provides a non-colored area that represents the simulation is not converged. Thus, the white area here also represents the case having no solution for the interior layout.

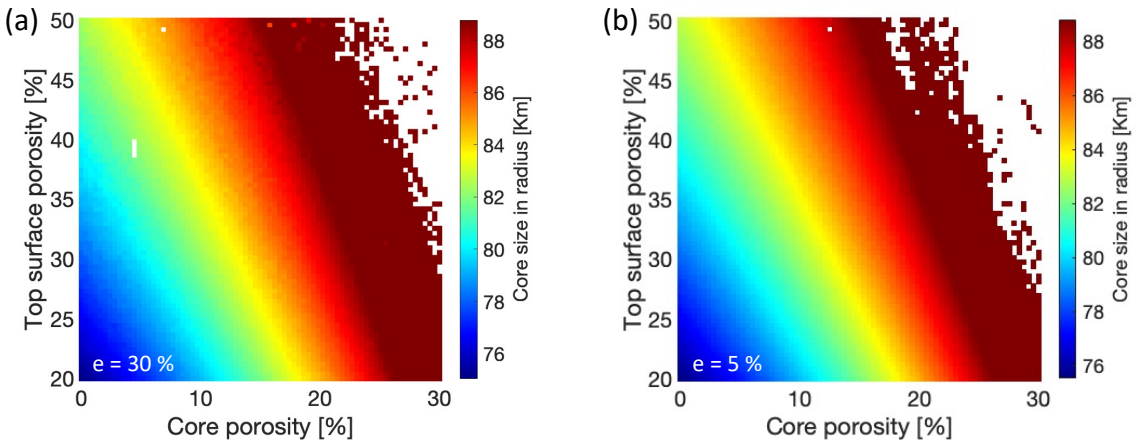

Figure 3.19: Comparison of colormaps that shows the core radius between the compression rate of 30 % and 5 %

Also, since the compressed layer thickness is less thick than the top surface and core as seen in Figure 3.13 (b), the change in the compressed layer's bulk density does not have a significant effect on constraining the entire layout distribution. As a final note, we only run simulations within a reduced porosity range (20 - 50%) for the top surface compared to the original setting (10 - 50%), but this does not change our conclusion.

3.3.4 Discussion

Based on the constrained interior layout distributions, we further analyze possible internal conditions that are compatible with the observed surface features of Psyche. Using the core size and the thickness of the silicate-rich layer defined by the simulations (Section 3.3.3.1), we discuss the following likelihoods to reveal the metallic components in the core onto the surface if the differentiated structure is the case for Psyche: 1) If the iron core could be exposed at crater-like regions by the impact cratering process and 2) If Psyche could experience ferrovolcanic surface eruptions.

3.3.4.1 Exposed metallic materials at crater-like regions

The current shape of Psyche [4] exhibits topographic features that represent *almost certain* craters at two locations as described in Section 3.3.1.2. Here, the confidence level - *almost certain* - is determined in [4] by comparing the current shape model to previous work [141,

135, 142] in terms of topographical and optical albedo features. As described in Section 3.3.1.2, the radar albedo indicates potential metal abundances in those two crater-like regions. In the following discussion, we further constrain the compatible core size with the observed features on Panthia and Eros.

The process that likely causes the localized concentration of metals within Psyche's crater floor is impact cratering [176, 178, 163]. In general, the impact crater formation has three stages: contact-compression, excavation, and modification stages. Figure 3.20 is a schematic depicting a plausible impact cratering scenario within the differentiated layers. After the contact-compression stage (when an impactor hits the surface and then the generated shock waves compress this area downward), a transient crater begins to form by ejecting away the materials (the excavation stage). If a transient crater formation penetrates a thin silicate layer to reach the metallic core, the ejected materials can be made up of mixed silicate and metal. The developed impact ejecta then radially falls onto the surrounding crater. The metal-mixed regolith via the impact-cratering procedure could explain the association of the crater-like region and its high radar albedo features observed in Psyche [4].

In order to constrain interior conditions to reveal the metals on the surface during an impact, we first estimate the maximum excavation depth (H_{exc}) where materials can excavate and become the ejecta. Based on the simple crater formation process, H_{exc} is experimentally derived as only about one-third of the full depth of the transient crater, which is also approximated as one-tenth of the transient crater size (D_t) [176]. The material deeper than H_{exc} takes place beneath the transient crater floor, which cannot be revealed on the surface. Given the final crater sizes (D_f) of Panthia ($\sim$ 90 km) and Eros ($\sim$ 62.5 km), each of D_t can be determined using a typical value ($\sim$ 1.2) of D_f/D_t empirically derived for terrestrial craters [176]. Eventually, the maximum excavation depth estimates are 10.8 km and 7.5 km for Panthia and Eros, respectively. The depths are a little deeper than their final crater depths, $\sim$ 10 km for Panthia and $\sim$ 4 km for Eros depicted in the current shape model. We then find the minimum core size that can be within the excavation areas by measuring the distance between the deepest excavated horizon and the center of the mass of Psyche. In Panthia, the core over the size of 78 km can reach the excavated zone, while Eros requires the larger one over 83 km. Panthia has the lower

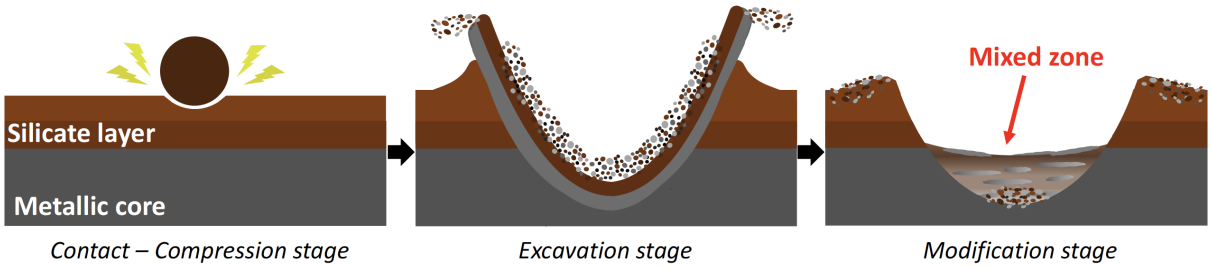

Figure 3.20: Impact cratering process schematic for a crater-like region on the surface of Psyche. Here, brown-like colors indicate silicates, while grey-like ones mean metal.

estimate of the core size to be exposed because its size is larger than Eros and thus induces a deeper excavated horizon. We marked this result as black dotted lines in Figure 3.15. If a core size is over this line, we can infer that the metal in the core is ejected with the upper silicate layer in the excavation stage and eventually exposed at the breccia lens and ejecta blanket of the craters.

3.3.4.2 Ferrovolcanic surface eruptions

Ferrovolcanism denominates the process that the core materials intrude into the covered rocky layer or even erupt onto the surface of planetesimals while solidifying. [150] first suggested that Ferrovolcanism may be an applicable mechanism to explain metallic components distributed on the surface of metallic asteroids. [127] then analyzed that the differentiated Psyche may experience the ferrovolcanic surface eruption given the size and bulk density driven by [134]. If this mechanism indeed occurs, there are a few requirements. First, Psyche's core should be crystallized from the surface to inside (i.e., inward solidification). If the core is too large, then the outward solidification is a more suitable process like the case for the Earth [179]. However, the estimated core size of Psyche, $\sim$100 km at maximum, is compatible with the inward solidification process [180, 171]. Second, the core should have melted sulfur-rich contents, which are lighter constituent elements than iron and nickel. Third, the core should produce a layer composed of solid iron-nickel and sulfur-rich liquid while solidifying because the excess pressure generated by the density contrast between the solid and the melt becomes an energy source for melt to intrude the rocky layer. To address the second and third conditions on Psyche, [127] referred to the simulation results regarding the inward core solidification conducted by [171].

This work confirmed that Psyche-sized core ($\sim$100 km in radius) is possible to produce pockets of sulfur-rich liquid within the solid iron-nickel while the core is cooling down. Using two free parameters, the vertical extent of melt and the amount of sulfur inside the melt, [127] calculated the rocky layer thickness that the sulfur-rich melt can penetrate (Ref. figure 3 in [127]).

We set the minimum and maximum silicate layer thicknesses found in Figure 3.16 as the lower and upper limit of the silicate layer to assess the ferrovolcanic surface eruptions on Psyche. The minimum and maximum silicate layer reaches up to $\sim$16 km and $\sim$ 68 km when the structure has the lowest porosity. In the following description, we use the results from [127] to suggest feasible conditions to experience the ferrovolcanic surface eruption given the silicate thicknesses. In order to penetrate the rocky layer of $\sim$ 16 km thick, the core needs to sustain the vertical extent of melts higher than at least 5 km, which can be sufficiently generated in the inward solidification of the Psyche-sized core [127]. The required amount of sulfur-rich contents is at least $\sim$13 wt$\%$ S and reaches up to $\sim$27 wt$\%$ S as the vertical extent of melts decreases from 20 km to 5 km thick. On the contrary, the rocky layer of $\sim$ 68 km thick necessitates a much larger vertical extent of melts and sulfur-rich contents than the thinner case. The corresponding core condition to the thickness is at least 20 km height of the melt, including more than $\sim$25 wt$\%$ S of sulfur-rich contents. As assessed by [127], we also confirm that the defined structural layout still supports that Psyche might experience ferrovolcanism to reveal the metallic materials in the core onto the surface when the requirements (i.e., the size of the vertical extent of melts and amount of sulfur-rich contents) are satisfied. As a final note, we address that our results of the interior layout were obtained using the data (i.e., shape, rotation period, and bulk density) in the current state. However, Ferrovolcanim is a possible mechanism when the core is solidifying, which means that the timeline is unlikely to be the current but the early stage of the planetesimal formation. Therefore, the analysis above is only reasonable when Psyche has not experienced significant changes in its shape and physical properties compared to its primordial ones.

3.3.5 Limitations

The first issue means that the mechanical properties (bulk density and porosity) in our structure model are homogeneously distributed in each layer. In reality, these properties may change continuously as seen in the lunar crust [181, 169, 174]. For example, porosity likely decreases proportionally as the applied pressure is high. Likewise, the bulk density tends to be denser at the deeper layer. Thus, these mechanical properties are considered functions of depth in general. However, the currently available Psyche data is not sufficient to consider the details. This homogeneity assumption can be reconsidered as an inhomogeneous structure given its gravity field data obtained from the upcoming Psyche mission.

The second issue describes that we keep the core shape as a sphere. However, given that the gravity field of Psyche and its moment of inertia are currently unknown, this assumption can be reasonable. A recent study, [142], suggested that Psyche might form at equilibrium, and its shape could be deformed by post-impacts. They addressed that the current shape presents small deviations from a Jacobi ellipsoid with a spin period of $\sim$3 hr and thus inferred that this might be Psyche's primordial conditions. However, this work does not provide any constraints on the possibility of the core being in hydrostatic equilibrium. After the primordial shape had been formed, it is highly possible to have been influenced by some disturbances such as impacts [138] that might affect the internal structure. Given that there is no data (i.e., gravity field) to constrain its impact scenarios and primordial conditions, it is unavailable to model such a core shape of Psyche correctly. As with the first issue, we believe that the upcoming NASA's Psyche mission will provide more information (i.e., whether it is differentiated or undifferentiated, high-resolution topographic features to constrain its impact history) to better constrain its internal structure, and then we will revisit this issue.

Here, we review some earlier works (e.g., [142, 127, 138]) that may hint at Psyche's initial shape and impact history. First, in terms of the initial shape, [142] developed Psyche's shape using disk-resolved images and derived a triaxial ellipsoid consistent with the shape model. Then, they found that the spin period of $\sim$3 h is compatible with inducing hydrostatic shape corresponding to this triaxial ellipsoid. Based on this result, they suggested that this triaxial

ellipsoid might be a primordial shape of Psyche having a spin period of $\sim$3 h and post-impacts slowed down its spin period up to $\sim$4.2 h and led to the current shape. However, this work does not put any constraints on its core shape although it may provide insight into the initial condition of Psyche's surface geometry. Second, regarding the impact history, [149] tested a hit-and-run scenario, one of the hypotheses of Psyche's evolution, between two planetesimals based on Smoothed Particle Hydrodynamics. They proposed that Psyche could repeatedly experience hit-and-run collisions and eventually become a mantle-stripped body. The collision simulation corresponding to this scenario showed that the entire structure is highly disrupted by the impact and reaccumulated. However, this work is also one of possible scenarios for Psyche and does not provide any details on the current internal structure. Lastly, we note that [127] recently assumed the structure of Psyche as a differentiated one to assess the possibility of a ferrovolacanic surface eruption process. The structure was modeled to have two layers that have the same layout with the triaxial shape model by [134]. However, this assumption was not based on any evidence. They also mentioned that Psyche's shape might be more complex than their current assumption. Given this, we decided to use a spherical core shape for the simplest assumption in the current work.

3.3.6 Conclusion

In this study, we used the Three-layer model and FEM approach to constrain the interior layout of Psyche, given that this object is a metallic core covered with a silicate-rich layer. Below are the main results of our simulations.

- If Psyche indeed originated from a differentiated planetesimal, given the reported bulk density of 4.0 g cm^{-3}, the estimated core size is 72 km to 88.5 km in radius (30 - 45 $\%$ of the overall size of Psyche) within the assumed porosity ranges.
- The crushing limit of silicate affects the core size, but this change is minimal. With the lower crushing limit, the core size becomes smaller under the same geophysical condition because the compressed layer is thicker than the higher crushing limit case. Since this compressed layer has a high bulk density and takes up a more significant portion

of Psyche's mass, the sustainable core size becomes smaller. The minimum core size reaches 71 km at the 5 MPa crushing limit while slightly increasing to 71.8 km at the 15 MPa case.

- The compression rate in the silicate layer has a minimal effect of constraining the core size. Under the pressure regime (- 15 MPa) in the silicate layer of Psyche, compaction would occur with a less significant scale (compression rate less than 30 $\%$). Within this scale, the change in the compression rate does not induce any noticeable difference in the final interior layout.

- The current observation analysis shows that Panthia has the highest radar albedo than the surrounding, indicating a localized region of high metal concentrations. In addition, Eros cannot be excluded from metal abundance because this region is still within the area having elevated radar albedo and bifurcated radar echoes implying high metal sources. The minimum core size compatible with the impact cratering process to induce metal excavation at Panthia (Eros) is 78 km (83 km) in radius, which takes up 34 $\%$ (40 $\%$) of the total size of Psyche. The non-porous iron core even excavates its metal onto the surface at Panthia if the top silicate layer is highly fragmented ($> 30\%$).

- The constrained interior layout has the minimum and maximum silicate layer of $\sim$16 km and $\sim$ 68 km at the pole and equator under the spherical core shape assumption when the structure has the lowest porosity. This structure condition still supports the ferrovolcanic surface eruption as suggested by [127]. However, this interior layout is derived using Psyche's current physical conditions, which may not provide any insight into the timeline of Ferrovolcanism. Thus, this conclusion is only reasonable when Psyche still keeps its primordial conditions.

This case study suggested a possible interior structure of Psyche given the hypothesis that the asteroid is originated from a differentiated planetesimal. We then investigated the possible structural conditions compatible with the impact cratering process and ferrovolcanic surface eruptions to explain metal abundances on Psyche's surface. With detailed observations by

NASA's Psyche in 2026, the current work will be extended to understand Psyche's internal structure, which will provide insight into its history.

3.4 Case study: (486958) Arrokoth

3.4.1 Research background

(486958) Arrokoth is a cold classic Kuiper Belt Object (KBO), which has been minimally dynamically perturbed. The cold classic KBO is generally considered to have been formed directly rather than having been moved into their orbits by Neptune or other dynamical processes [182, 183], and thus Arrokoth might be one of the most primitive objects in our solar system. In 2019, NASA's New Horizons spacecraft successfully made its historic flyby to Arrokoth at a distance as close as $\sim$3,500 km. During the close approach, it took an image using the Long Range Reconnaissance Imager (LORRI). The LORRI image confirmed that Arrokoth has a bilobated shape – two lobes connected with a narrow contact region (hereafter 'neck') – and revealed the details of its shape and geological features [184, 185, 9, 186]. The contact binary shape of Arrokoth consist of a relatively smaller lobe having a maximum dimensions of 15.4 km $\times$ 13.8 km $\times$ 9.8 km and a larger lobe having that of 20.6 km $\times$ 19.9 km $\times$ 9.4 km. Those two lobes are considered planetesimals which had been formed in a protoplanetary disk and highly porous objects that composed of abundant Methanol ice (CH_3OH) and dusts [185]. Given the Arrokoth's current shape, the most probable formation scenario is that those two chunks are gently collided each other with a very slow speed less than 5 km/s instead of high speed collision [183, 187]. The fact that the Arrokoth's surface does not show any signs for catastrophic disruptions also supports the gentle merging process [188]. One geological feature identified in New Horizons images is that Arrokoth has the largest crater-like region (hereafter 'sky crater') on the small lobe. The depression has a size of 7 km width and 1 km depth and is probably an impact crater because of its bowl shape. The sky crater takes up $\sim 7\%$ of the size of the small lobe. Given the significant crater size, we postulate that the structurally weakest neck region of Arrokoth might be subject to the substantial structural disturbance (i.e., neck break up) if the sky crater forming event occurred after the bilobate shape had formed [8].

In this study, we visit the question of how the bilobated Arrokoth responded to the structural disturbances generated by the sky crater impact. We mainly focus on the change in the cohesive strength regime required to keep the current shape on the neck of the bilobated shape after the sky crater impact event. For this, we used a developed numerical model that has twofold. The first stage is to characterize the impact parameters (i.e., impact speed and impactor's size) that generate the identical size of the sky crater using the crater-scaling relationship. As a next stage, we adopted the finite element model to investigate the structural disturbance responding to the sky impact in terms of the cohesive strength level evolution around the neck, given the information on the characterized sky crater forming event. We provide a full description of the methodology in Section 3.4.2 and our simulation results in Section 3.4.3. In Section **??**, we discuss the measured cohesive strength regime by referring to other small bodies' strengths and the key findings that could indicate the potential dynamical behavior of the bilobated structure after being subject to the sky crater-like large impacts.

3.4.2 Numerical model

To explore how Arrokoth reacted to the sky crater-forming impact, we developed a numerical model for constraining the minimum cohesive strength regime required to keep the current shape without any structural disruptions. The model has two stages of investigating the evolution of stress fields of the entire object after the sky impact. In the first stage, we use a pi-scaling law for characterizing the environment when the sky crater had formed to estimate the linear momentum imparted into the small lobe due to the sky crater. At the following stage, we use a finite element model for measuring the stress field across the Arrokoth structure, especially the the neck area, when applying the impulse velocity derived by the linear momentum caused by the sky impact. The time-varying stress fields provide the minimum cohesive level required for the Arrokoth structure to keep the current bilobated shape after the sky crater forming impact.

3.4.2.1 Sky crater forming impact event characterization

We have a limited information used for characterizing the sky crater forming impact event. First, we can estimate the size of the final crater after the impact. The Arrokoth LORRI image

revealed that the sky crater has a size of ∼7-km width and 1-km depth [184], which has a similar depth/diameter ratio with craters on other objects (i.e., Šteins and Eros, main belt asteroids) that have the similar gravity field with Arrokoth. Second, we know the Arrokoth's composition that includes abundant methane and water ice [185]. Lastly, earlier studies ([183, 8, 186]) investigated that Arrokoth's bulk density is likely to be between 250 to 500 kg/m^3 by analyzing its geophysical properties and structure stability. Given this information, we use a pi-scaling law suggested by [7] to estimate the impact-induced linear momentum.

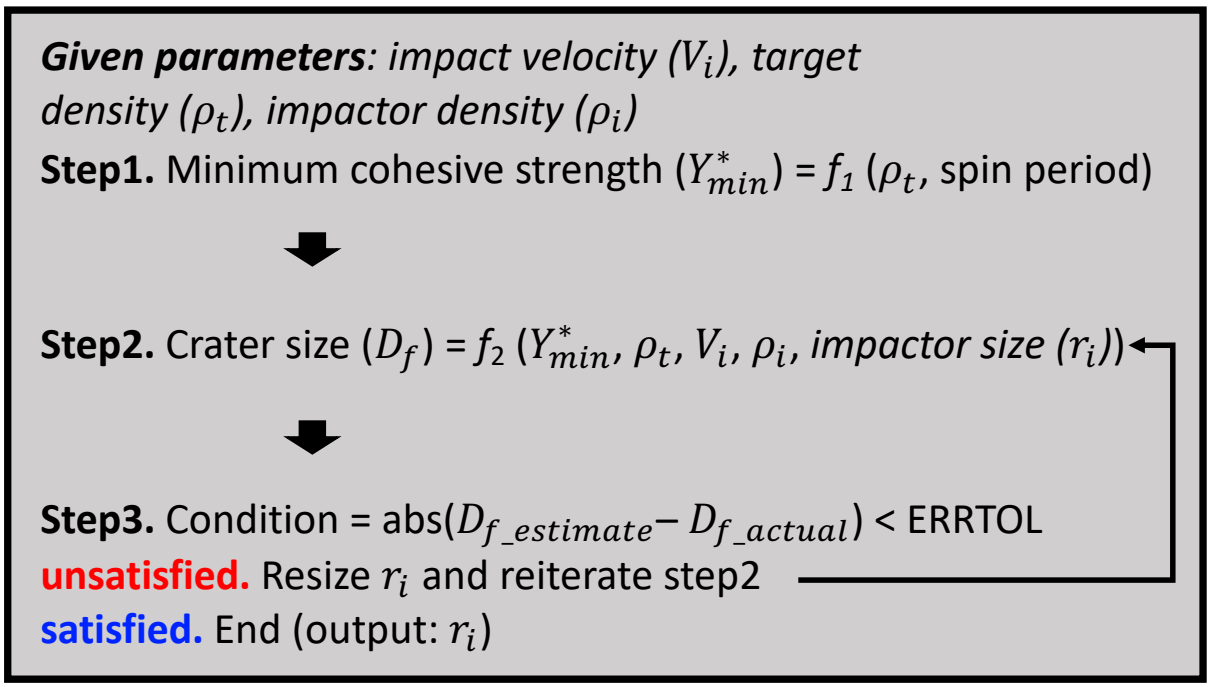

Figure 3.21: Algorithm of the impact crater size scaling law model. In step 1, the minimum cohesive strength is determined based on the stress field at the equilibrium state using the FEM. The equilibrium is defined when the object is under its self-gravity and rotation without any other external effects. In step 2, the crater size is determined based on a pi-scaling law relation [7] given the assumed impact parameters (i.e., bulk density of the taget and impactor and the impactor's velocity). We follow Equation (7) in [8]. In step 3, we compare the estimated crater size to the actual size of the sky crater. For the comparison, we set the error as 10^{-7}.

Figure 3.21 shows a schematic of our model using a pi-scaling law. In this model, we first estimate the crater size using a different combination of the impact parameters and then compare the estimate to the actual size of the sky crater. Here, the impact parameters includes a target's bulk density (here, a target is Arrokoth), a target's strength, an impactor's bulk density, and impact velocity. Given the uncertainty of the impact parameters, we make assumptions that could be applicable to the case of KBO. For the impactor's bulk density, we assumes that

the impactor has the same materials as the targeted body, Arrokoth. Since the most reasonable bulk density regime of Arrokoth is between 250 kg/m^3 to 500 kg/m^3, that of the impactor also follows the same range. For the impactor's speed, we refer to the impact speed distribution onto Arrokoth investigated by [189]. The study suggests impact velocity spectrum onto Arrokoth for each Kuiper Belt sub-population with the collision probability (Figure 2 in [189]). If the impactor comes from the cold classics, which have the similar orbit to Arrokoth, the impact speed likely ranges between 100 m/s to 1 km/s with the peak value of 300 m/s. The impact speeds are all distributed in the range less than 4 km/s, even if the impactor comes from other regions, not the cold classics. Lastly, for the target's strength, we estimate the stress field of Arrokoth at the equilibrium state using the FEM when it is under its self-gravity and rotation without any other external effects (Step 1 in the pi-scaling law model). Figure 3.22 shows the cohesive strength distribution on a slice of the Arrokoth structure. The cohesive strength is computed from the FEM simulation given its current spin period of 16 hr and bulk density of 500 kg/m^3. The maximum strength of around 3 kPa occurs at the neck regions, and the entire body's strength at the equilibrium does not exceed 5 kPa. In step 2, we convert the impact parameters to a crater diameter using a pi-scaling law. Here, we follow the impact crater scaling model applicable to Arrokoth developed by [8]. The study adopts a conversational approach for the crater scaling laws by [7], although there might be added uncertainty in applying it to KBOs due to the limited knowledge of their impact processes [190]. As seen in step 2 in Figure 3.21, a crater diameter can be measured as a function of the impact parameters and impactor's size (see Equation (7) in [8]). In step 3, we compare the estimated diameter to the actual diameter of the sky crater, $\sim$7 km. Given an error of 10^{-7}, we reiterate the estimation of the crater size by parameterizing a factor of the impactor's size until the estimate matches the actual size.

Using the impact scaling model, we investigate the linear momentum brought in by the impactor (Figure 3.23 (a)) and the corresponding impulse velocity felt by the small lobe (Figure 3.23 (b)). The impulse velocity is computed based on the simple assumption that the linear momentum imparts to the small lobe. We consider three different cases for the impact speed within the possible regime suggested by [189]. The preliminary result shows that the linear momentum decreases as the impact speed decreases. This trend is caused by the fact that

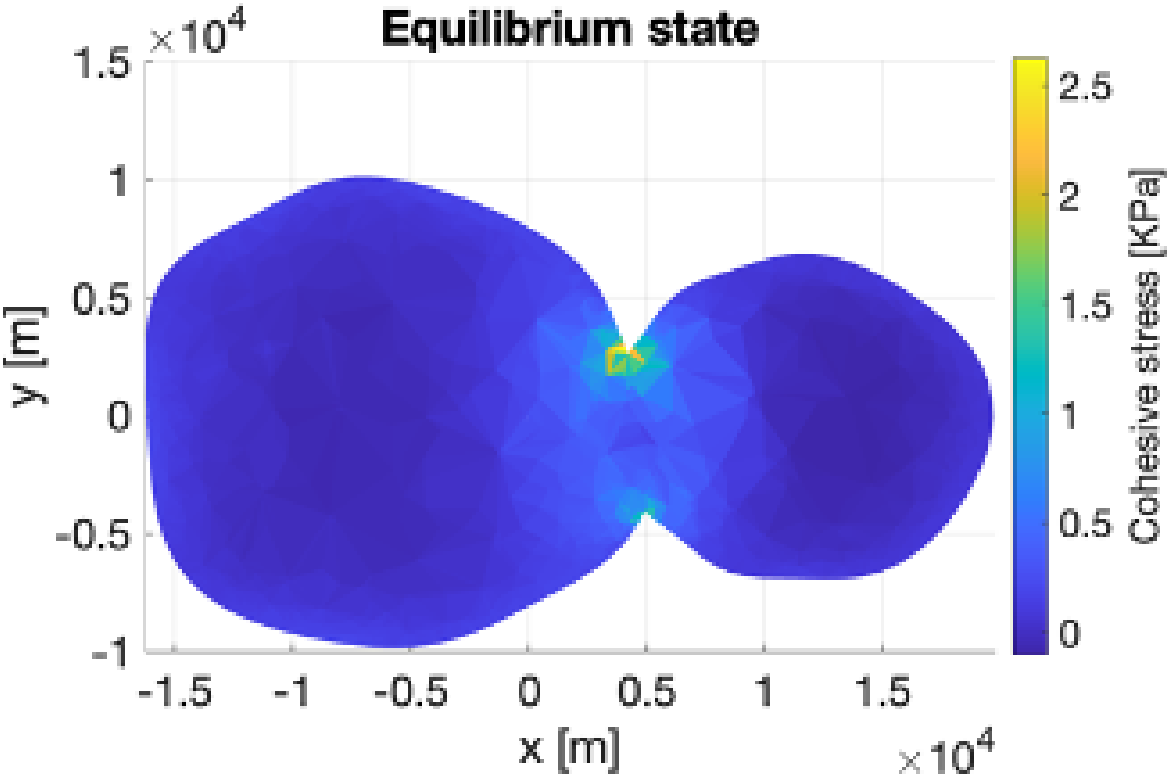

Figure 3.22: Arrokoth's strength regime at the equilibrium state. This plot shows the cohesive stregnth distribution on a slice of the object. The cohesive strength is computed from the FEM simulation given its current spin period of 16 hr and bulk density of 500 kg/m^3. The cohesive strength around the neck is less than 3 kPa, and the entire structure has the cohesive stregnth regime less than 5 kPa.

a larger impactor is required to generate the 7-km-wide crater with a slower impact speed. However, all the cases with an impact speed of fewer than 1 km/s have the same order of magnitude ($\sim 10^{13}$). The magnitude of the linear momentum induces an impulse velocity of around 0.1 m/s. Given the lower impact speed, the impulse velocity becomes higher.

3.4.2.2 Impact-induced cohesive strength variation

In order to calculate the time-varying stress field after the sky crater forming event, we extended a numerical approach, initially developed by [72], using the finite element method for computing the stress field of an irregularly shaped body. The irregular shape is modeled as

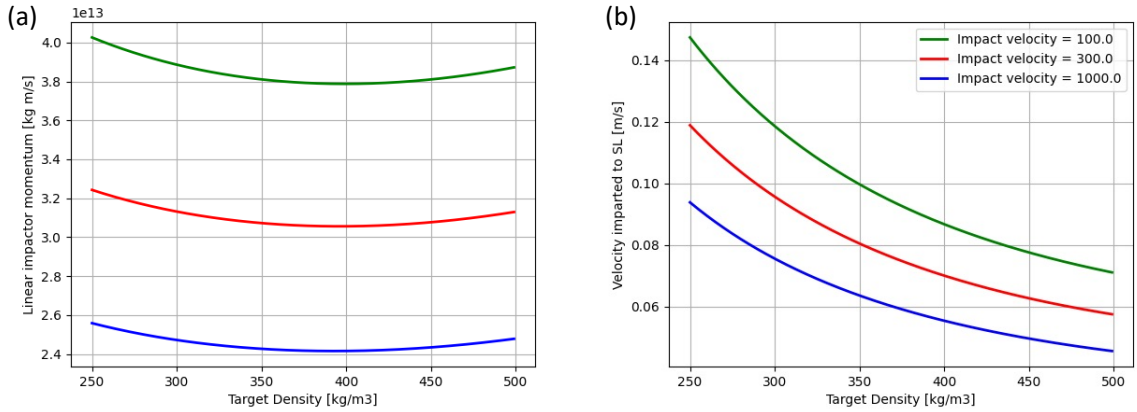

Figure 3.23: Result plots from the pi-scaling law model. (a) shows the linear momentum brought in by the impactor given the impactor's velocity ranging from 100 m/s to 1 km/s. The green, red, and blue colored lines represent the impactor's velocity of 100 m/s, 300 m/s, and 1 km/s, respectively. Here, the bulk densities of a target and an impactor are set as 500 kg/m^3. The minimum cohesive strength is set as 5 kPa, which is above all cohesive strengths at the equilibrium state. (b) shows the impulse velocity imparted into the small lobe by converting the estimated linear momentum based on the linear momentum conservation when the impactor contacts the small lobe. When the object is denser, the impulse velocity is slower because of the higher mass of the structure.

a 4-node tetrahedral mesh and is considered to have a uniform rotation behavior. The distinguished feature of this numerical model is considering the time-varying loading derived from the targeted body's dynamic behavior, such as rotation, and provides the dynamic evolution of the stress field. The stress calculation is based on linear-elastic deformation. It is considered to have no large shape deformation, which means the body keeps its initial shape all the time while applying the dynamic loading vectors on the object. This model has been adopted for other small bodies to characterize their structural properties (i.e., cohesive strength). [72] used this model to investigate the stress evolution of (99942) Apophis, expected to close flyby the Earth in 2029, given that it is affected by the tidal effect. This study revealed that the most significant stress variation occurs at the neck region of the Apophis' contact binary shape, although the stress variation would have a minimal effect on occuring changes in the Apophis' structure condition during tis 2029 Earth encounter. Another previous study was adopting this numerical model to (16) Psyche, the largest metal-rich asteroid in the main asteroid belt, to

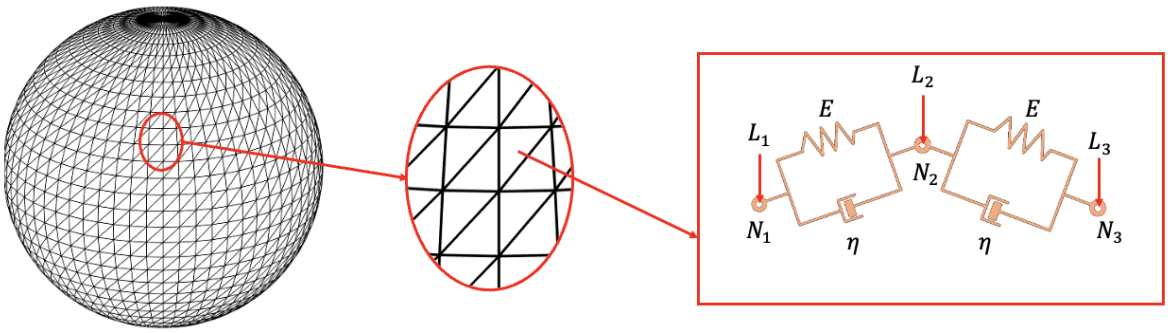

Figure 3.24: A schematic showing how nodes are connected to each other. In the selected viscoelastic model (Kelvin-Voigt model), the connection between each node is modeled as a paralleled spring and dash-pot system. Here, the left-side panel is the FEM mesh, while the middle-side panel shows the zoomed part of the mesh. The right-side panel depicts the node connection in the Kelvin-Voigt model. N defines the node, while L represents the loading vector. E and η are Young's modulus and viscosity, respectively.

constrain its possible interior structure layout given the assumption that Psyche is a differentiated silicate-iron body [191]. In order to investigate the viscoelastic behavior of Arrokoth after the impact, we extended the original FEM in this study.

The general formulations used for the FEM are well described in [72] and [191], mainly in terms of how the stress fields of a 4-node tetrahedral mesh representing an irregular shaped small body are computed given a time-varying lading vectors. The main change in the extended model is that we replaced the linear elastic model corresponding to Equation 16 in [72] (Equation A3 in [191]) to the viscoelastic model represented by the kelvin-voigt model, which is the simplest approach to investigate the behavior of the viscoelastic material [192]. In the 4-node tetrahedral mesh, a connection between each node consists of a spring and a dash-pot in parallel as shown in Figure 3.6. The following equation describes the constitutive equation used for the extended FEM:

$$\bar{\sigma} = E\bar{\epsilon} + \eta\dot{\bar{\epsilon}} \tag{3.22}$$

where E and η are a constant defining Young's modulus and the viscosity, respectively. $\bar{\sigma}$ is the stress vector at a node that includes six components (σ_{xx}, σ_{yy}, σ_{zz}, σ_{xy}, σ_{xz}, σ_{yz}). $\bar{\epsilon}$ and $\dot{\bar{\epsilon}}$ are a strain and strain rate vector, respectively. As described in the previous studies ([72] and

[191]), $\bar{\epsilon}$ and $\dot{\bar{\epsilon}}$ can be rewritten as a function of a displacement ($\bar{u}$) and displacement rate ($\dot{\bar{u}}$) as follows:

$$\bar{\epsilon} = \nabla N \bar{u} \tag{3.23}$$

$$\dot{\bar{\epsilon}} = \nabla N \dot{\bar{u}} \tag{3.24}$$

where N defines the shape function that help approximately characterize variables in the off-node region. As a final note, the extended FEM solves the second-order differential equation with respect to $\bar{U}$ using a Runge-Kutta 4th-order integrator. Here, $\bar{U}$ a $3\kappa_n$ sized vector that combines all $\bar{u}$ for each node where κ_n is a number of node of the 4-node tetrahedral mesh. The second-order differential equation is given as:

$$\ddot{\bar{U}} + \chi \dot{\bar{U}} + \Psi \bar{U} = \bar{b} \tag{3.25}$$

where $\bar{b}$ is the dynamic loading vector that combines self-gravity and rotational force. Here, χ and Ψ are $3\kappa_n$-by-$3\kappa_n$ square matrices. Each matrices can be computed given the following parameters:

$$\chi = f(\rho, v, \nu, E) \tag{3.26}$$

$$\Psi = f(\rho, v, \eta) \tag{3.27}$$

where ρ and v are a bulk density and volume of the corresponding node.

3.4.2.3 Geophysical parameter settings

The geophysical and other parameters used for simulations are described in Table 3.6. As most geological parameters for the KBO are not well known, defining Young's modulus and viscosity to represent the material composed of the Arrokoth structure is difficult. We set the range of Young's modulus as 1 – 10 MPa, which is in line with the value of Young's modulus

range found at the surface of comet 67 P [193]. This range also includes the previous studies' parameter settings for the FEM [72, 191, 194] and the discrete element model [36] for small bodies. Next, we referred to [194] to set the possible range of the viscosity of Arrokoth. In Section 4.2 in [194], The viscosity of small bodies can be estimated using a quality factor (Q factor). The Q factor defines a dimensionless parameter characterizing the system having an energy dissipation and is given as Equation 3.28.

$$Q = \frac{\textit{Initial energy stored in the system}}{\textit{The loss of energy over one cycle of the oscillated system}} \tag{3.28}$$

Considering that the Arrokoth structure can be simplified as two-mass system connected with a spring and damper, the Q factor can be written as a function of the material's density, geophysical parameters (young's modulus and viscosity), and the equilibrium distance between the two masses. The following equation shows how the Q factor can be computed.

$$Q = \frac{2\pi}{1 - e^{\frac{-2\pi c}{\sqrt{k - \frac{c^2}{4}}}}} \tag{3.29}$$

Here, k and c are defines as below.

$$k = \frac{E}{\rho {l_0}^2} \tag{3.30}$$

$$c = \frac{\eta}{\rho {l_0}^2} \tag{3.31}$$

where ρ and l_0 are the Arrokoth's bulk density and the equilibrium distance between the small and large lobes. Using Equation 3.29, we figured out how η changes within the possible range of E. We apply the Q factor of 100, which is a typical value for solid bodies [195, 196]. Figure 3.25 shows the correlation between η and E given the Arrokoth bulk density regime ranging from 250 to 500 kg/m^3. We note that the Young's modulus has the same order of magnitude with the corresponding Young's modulus.

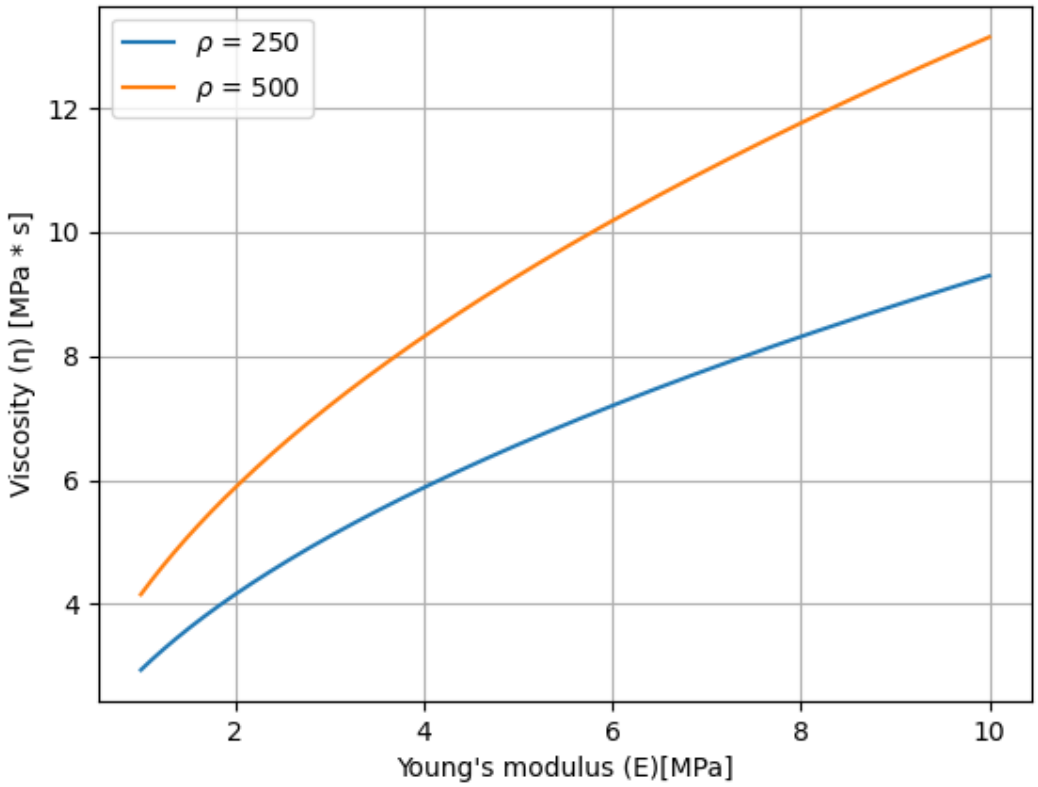

Figure 3.25: Viscosity settings depending on Young's modulus. The density (ρ) unit is kg/m^3.

3.4.2.4 FEM mesh resolution settings

The FEM needs a 4-node mesh representing an irregular shape of the targeted object. In the FEM simulation, one important step is to adequately refine the mesh to have a mesh quality until it can provide a reasonable FEM solution and computation time. In general, the FEM solver is more likely to face a divergence issue or provide a less accurate solution for stress fields as the imported FEM mesh is less refined because a coarse mesh usually has a low mesh quality. However, the more refined mesh tends to have unacceptable computation time to obtain the solution for stress fields. To generate the Arrokoth's FEM mesh, we start with the LORRI image derived shape model [9] as shown in Figure 3.26. Using the Tetgen [197] and MeshLab [198], which are commonly used FEM mesh generators, we generate and refine the FEM mesh. In our simulations, we selected the mesh (see Figure 3.27), which consists of 417 nodes and 1,392 elements, because it gives acceptable computation time. To assess whether the mesh

Table 3.6: Geophysical and other parameter settings for simulations.

Quantity	Value/Range	Units
Young's modulus	1 - 10	MPa
Poisson's ratio	0.25	[-]
Viscosity	1 - 10	MPa · s
Friction angle	35	○
Rotation period	15.92	hr
Bulk density	250 – 500	kg/m^3
Volume	TBW	m^3
Number of nodes	417	[-]
Number of elements	1392	[-]
Step size	0.01	sec
Total simulation time	16	hr

provides an acceptable result for stress fields, we performed the identical simulation with a higher-resolution mesh and then see how the stress fields depend on the mesh resolution. The high-resolution mesh has the finer mesh that consists of 1141 nodes and 4,108 elements.

In the simulation, Young's modulus and the bulk density are set as 10 MPa and 500 kg/m^3, respectively. Other parameters required for the simulation follow Table 3.6. Figure 3.29 shows the cohesive strength at the equilibrium on a surface and a slice of Arrokoth with the selected mesh, while Figure 3.28 show the case of the high-resolution mesh. We notice that the selected mesh is fully enough to capture the trend in the cohesive strength seen in the high-resolution one. Given the contact binary shape, the highest cohesive strength occurs around the neck region, which is the most narrow region of the entire structure. Both meshes show the high strength regime around the neck, although there is a little discrepancy in the strength regime. The high-resolution mesh has the maximum cohesive strength of 3.3 kPa and 2.0 kPa at the surface and the inside of the body, respectively. In the selected mesh, the cohesive strength at the surface and the inside of the body reach up to 2.6 kPa and 1.4 kPa for each, which shows the cut-off value of 0.6-0.7 kPa compared to the high-resolution one. However, the measured strength regimes in both cases still have the same order of magnitude. Furthermore, in the present problem of how the cohesive strength changes after the sky impact, we focus on the variation in the strength regime rather than its specific value. This strength discrepancy does not cause a significant change in our analysis of the strength variation on Arrokoth.

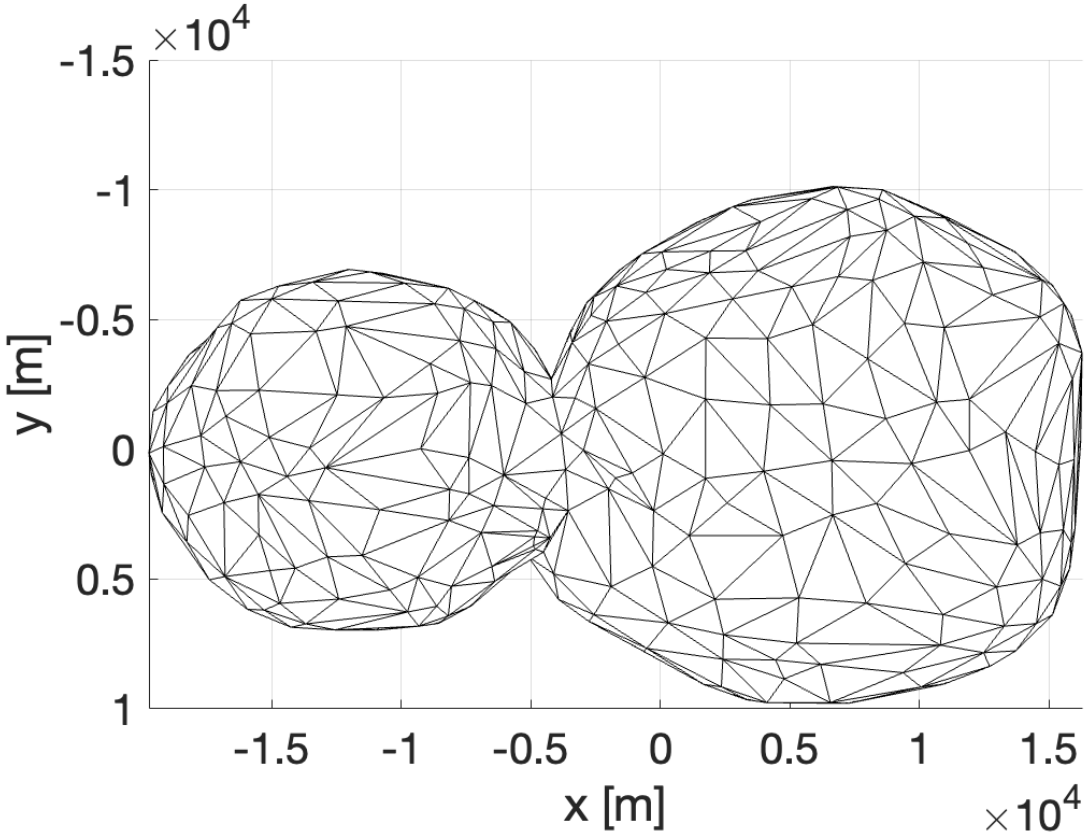

Figure 3.26: Arrokoth's shape model derived by the LORRI image [9]. This surface mesh consists of 832 facets and 417 vertices.

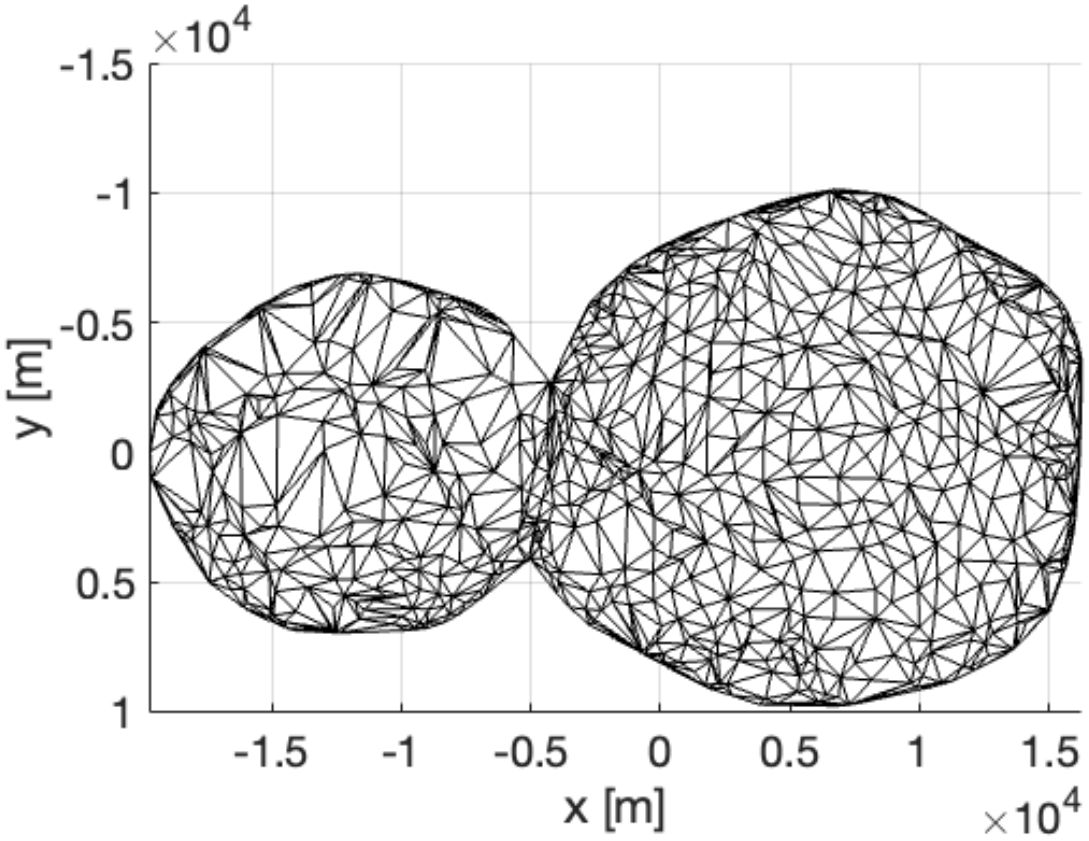

Figure 3.27: A slice of the selected Arrokoth's FEM mesh. This structural mesh used for the FEM simulation consists of 417 nodes and 1,392 elements.

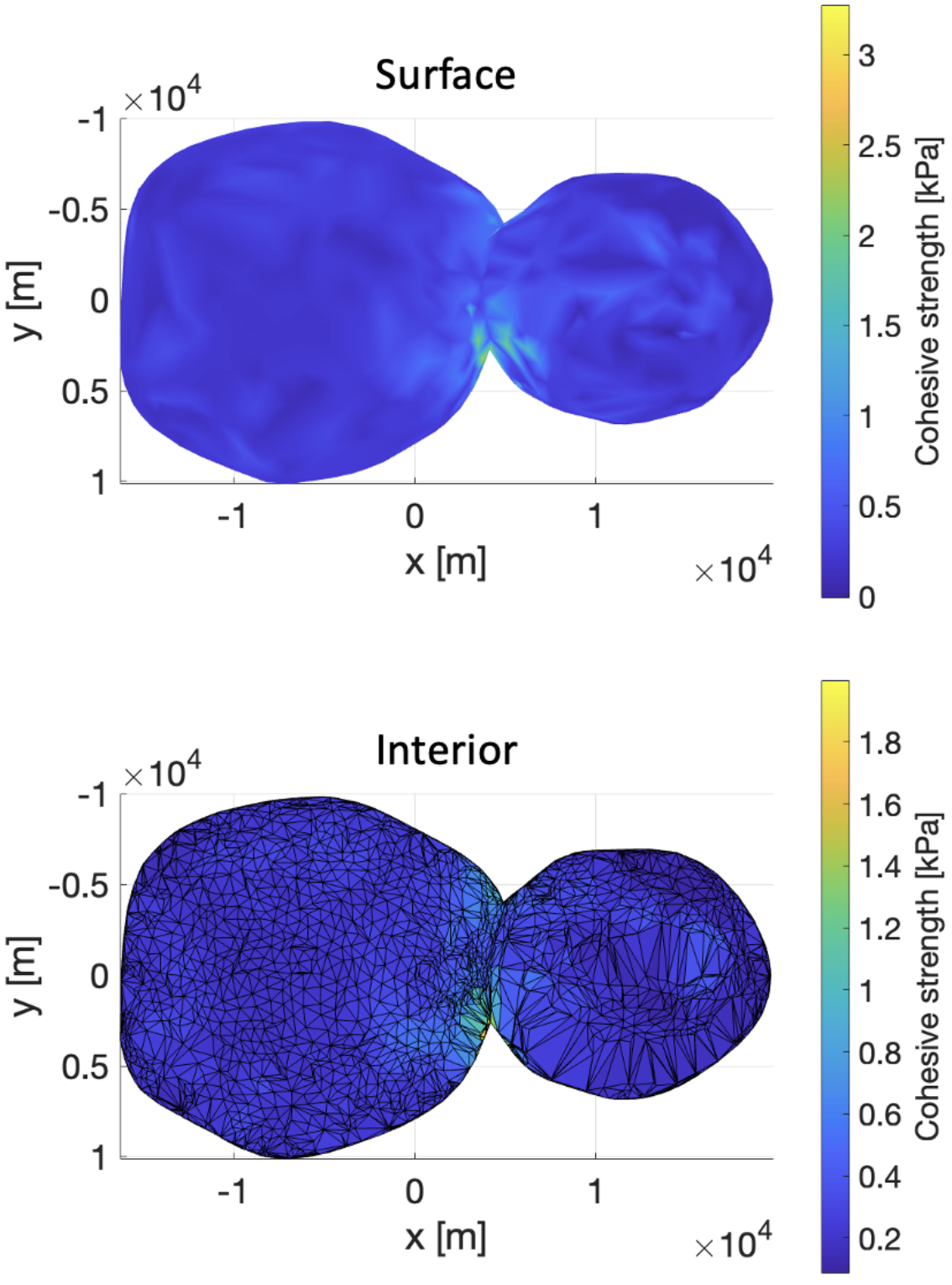

Figure 3.28: Minimum cohesive strength in Arrokoth at equilibrium state with the high resolution mesh. The cohesive strength at a surface and a slice of Arrokoth are shown in the top and bottom panels, respectively.

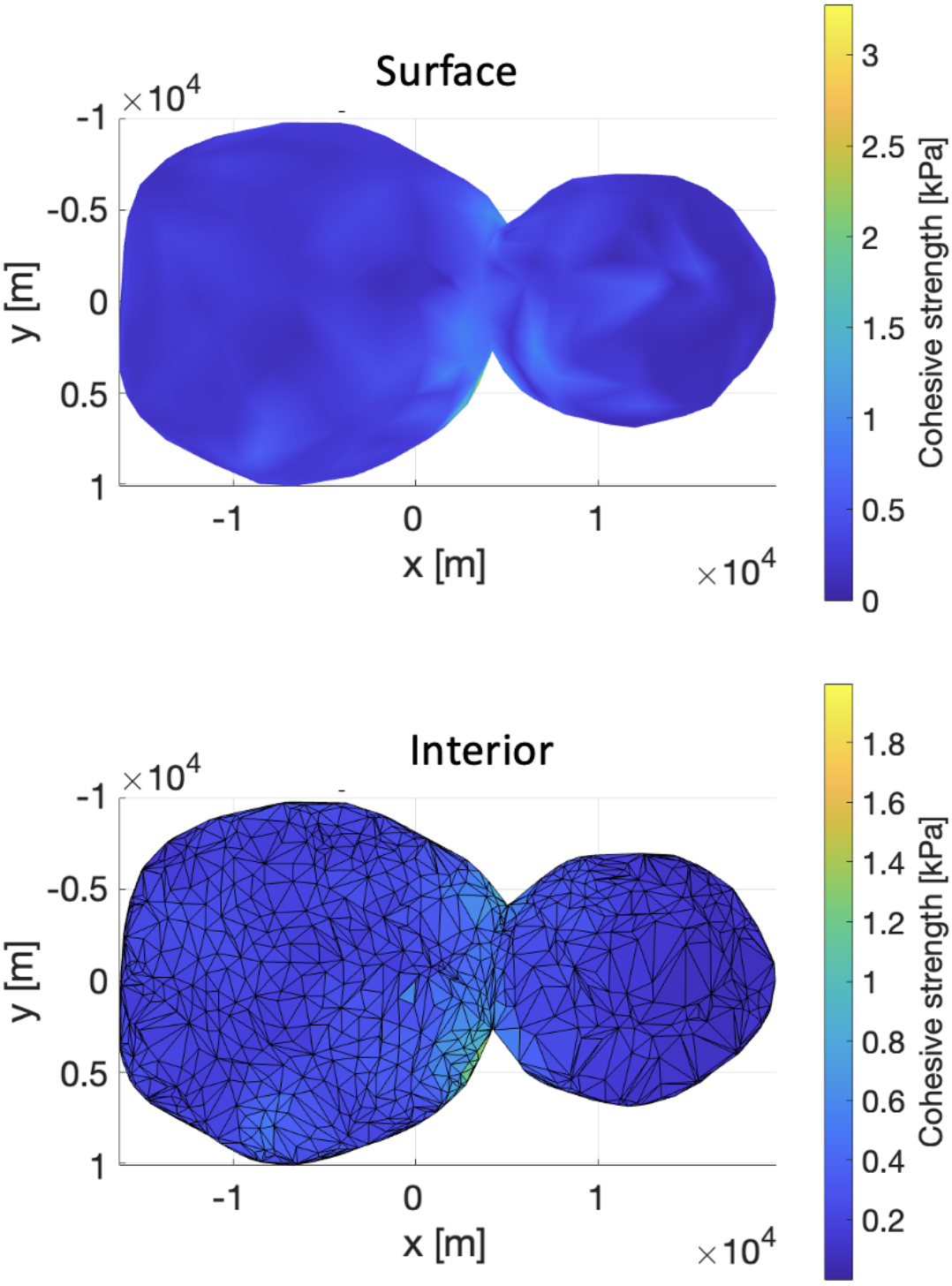

Figure 3.29: Minimum cohesive strength in Arrokoth at equilibrium state with the reduced-resolution mesh, which is used for the major simulations in this study. The cohesive strength at a surface and a slice of Arrokoth are shown in the top and bottom panels, respectively.

Table 3.7: FEM simulation results for three cases having a different bulk density of the target and impactor. Here, δY_{max} defines the highest cohesive strength variation.

Bulk density	Impulse velocity	δY_{max}
250 kg/m^3	0.148 m/s	15 kPa
350 kg/m^3	0.1 m/s	12 kPa
500 kg/m^3	0.071 m/s	9 kPa

3.4.3 Results and discussions

We performed the FEM simulations to constrain the cohesive strength regime required to keep the Arrokoth's bilobated shape. Given the uncertainty of simulation parameters (i.e., an impact speed, the target's density, and geophysical parameters – Young's modulus and viscosity), we run multiple simulations with a possible range of simulation parameter spaces (Table 3.6) and see how the maximum cohesive strength regime changes. In this section, we show a representative case to address the result for the FEM simulation. This case has the parameter settings given as: an impact speed of 100 m/s, a target's bulk density of 500 kg/m^3, and Young's modulus of 10 MPa corresponding to the viscosity of 10 Mpa·s. Figures 3.30 and 3.31 show the change in the cohesive strength variation on a slice and surface of the body, respectively. The time duration of the figures corresponds to a single cycle of the oscillation of the stress field. We notice that the cohesive strength variation reaches up to $\sim$12 kPa around 4 minutes after the impact around the neck area, which is the structurally weakest part of the bilobated structure. The specific node where the maximum variation occurs is located on the plane perpendicular to the direction of the sky impact. Figure 3.32 shows the time-varying cohesive strength at this location during the Arrokoth's rotation period ($\sim$16 hr). As see in the figure, the cohesive strength variation follows the response in the under-damped system with the current parameter settings. The following sections discuss how the maximum cohesive strength value changes depending on the simulation parameter settings.

3.4.3.1 Dependence on Bulk density

Table 3.7 summarizes the simulation parameter settings and the measured maximum cohesive strength. Given an impact speed of 100 m/s (see the green line in Figure 3.23 (b)), we selected

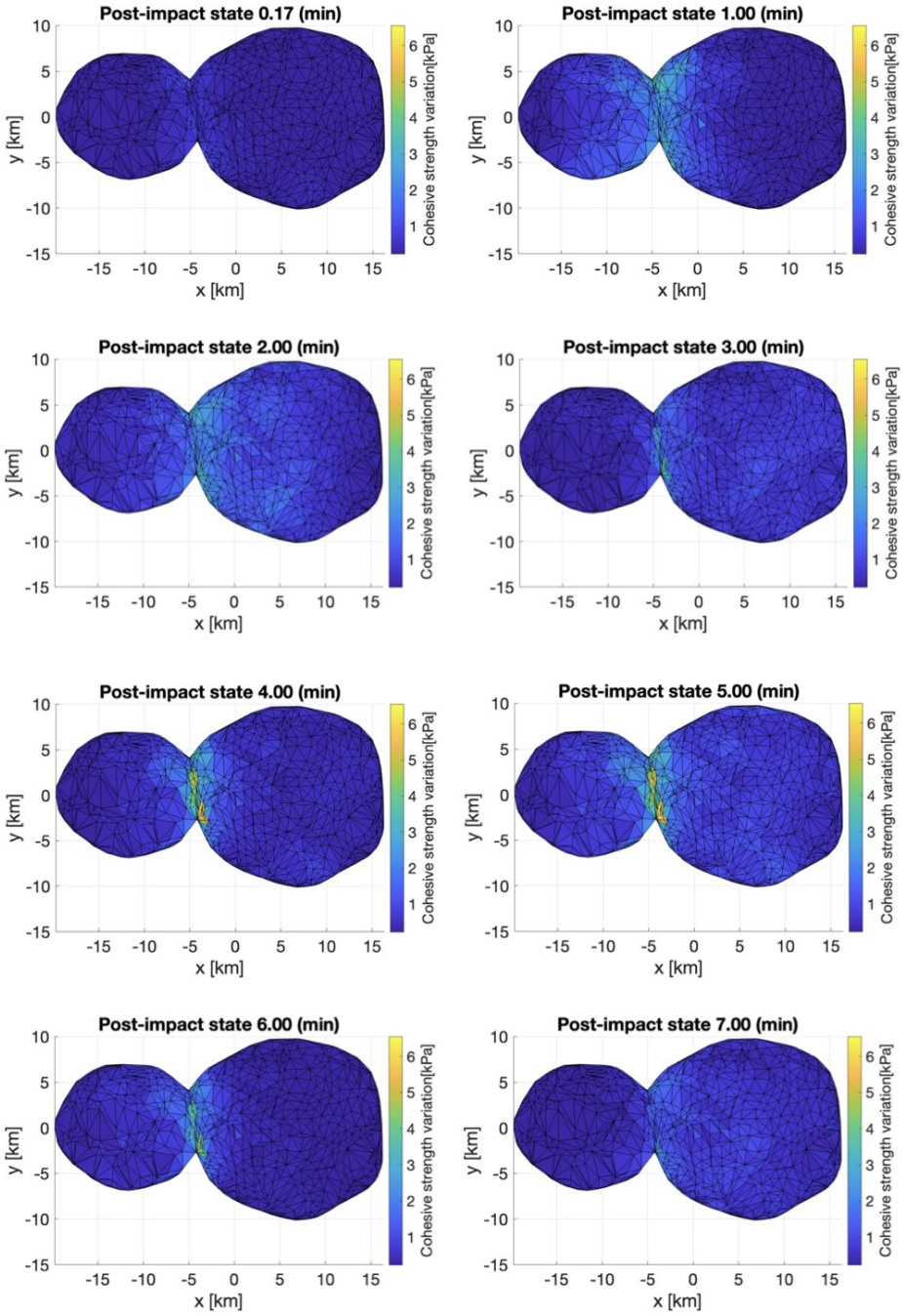

Figure 3.30: The result for the FEM simulation showing time-varying cohesive strength variation on a slice of the body over one oscillation cycle. The variation value defines a subtraction of the cohesive strength at a specific time state from the one at the equilibrium state. The impact speed, the target's bulk density, Young's modulus, and viscosity are set as 100 m/s, 500 kg/m^3, 10 MPa, and 10 Mpa·s, respectively.

three cases with a bulk density of 250 kg/m^3, 350 kg/m^3, and 500 kg/m^3. As seen in Figure 3.23 (b)), the different bulk density induces a different impulse velocity felt by the small lobe: As the lower bulk density corresponds to the faster impulse velocity because the linear momentum

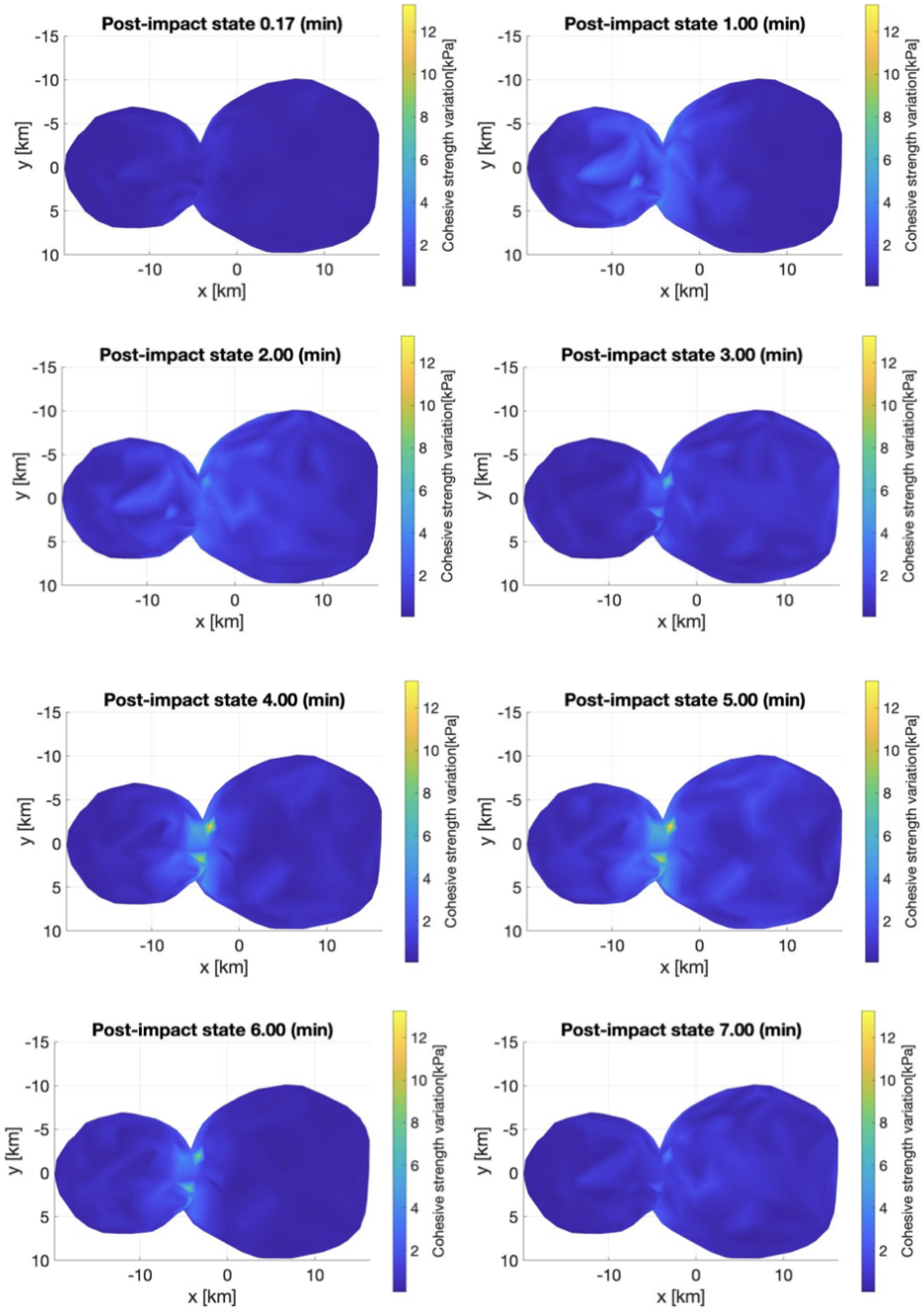

Figure 3.31: The result for the FEM simulation showing time-varying cohesive strength variation on a surface of the body over one oscillation cycle. The variation value defines a subtraction of the cohesive strength at a specific time state from the one at the equilibrium state. The impact speed, the target's bulk density, Young's modulus, and viscosity are set as 100 m/s, 500 kg/m^3, 10 MPa, and 10 Mpa·s, respectively.

imparted into the small lobe is larger. As a result, we can see the trend – the higher impulse velocity is applied to the small lobe, a higher cohesive strength level is required to keep the initial shape. If Arrokoth has a bulk density of 250 kg/m^3, the cohesive strength around the

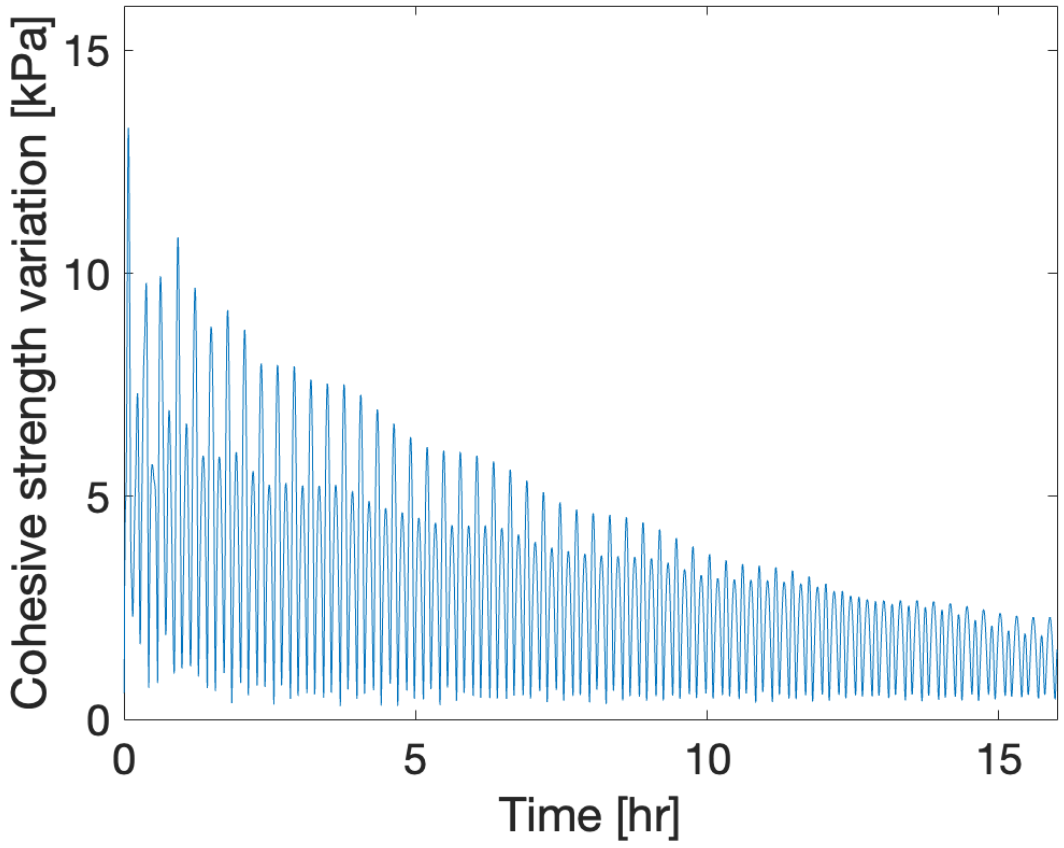

Figure 3.32: The result for the FEM simulation showing time-varying cohesive strength at a specific node where has the maximum cohesive strength over the Arrokoth's single rotation period ($\sim$16 hr).

neck area should sustain at least 15 kPa to avoid any structural disturbances or deformations. In the case of a bulk density of 350 kg/m^3 and 500 kg/m^3, the strength level becomes lower, up to 9 kPa. However, the same order of magnitudes in the cohesive strength variation occurs in all cases within the possible density range between 250 to 500 kg/m^3. This level of variation seems to be significantly higher than other small bodies, usually less than 1 kPa [199, 200], which may indicate that Arrokoth could experience structure disturbances such as neck breakup or shape configurations in the past. However, the current result cannot reject other possible scenarios, such that Arrokoth might have high cohesive strength or Arrokoth might protect itself from impacts due to the possible compaction effect from its highly porous structure. Further analysis of Arrokoth's LORRI image to look at any signs of shape configurations or structure disturbances can be future work to explore this question further.

Chapter 4

Conclusion and future works

This dissertation described case studies showing the process of how the science questions on small bodies can be investigated numerically using the currently available data. The numerical models were developed to characterize small bodies' properties on the surface and structure based on their complex dynamics. The selected small bodies were a group of NEAs, MBAs, comets, and KBOs. We note that the current numerical models still further need to validate the obtained results. Also, the selected objects in some of the projects are targets of the upcoming space missions, and thus advancing the current numerical models to connect with the potential data from the missions needs to be considered. The listed below describes the summary of each case study and potential approaches to either use mission data or observation data, which can provide better analysis and support the model validation.

- Section 2.1 showed the case study, which investigates how an asteroid's elongation controls the sensitivity of its surface to tidal effects during a distant planetary encounter beyond the Roche limit. We analyze the surface slope and its variation by considering the shape elongation, as well as the spin period and orbital conditions. The main result shows that a more elongated asteroid tends to have a higher slope variation, while there may not be a monotonic increase in the total area having such a variation. To explore whether our conclusion is observable in reality, we can consider the actual S- and Q-type asteroids and compare the measured surface sensitivity depending on their shape elongation. The concern is that the currently available shape models of the S- and Q-types are

still limited [1], and thus it might not be reasonable to do a general analysis on correlation between shape and albedo of S- and Q-types.

- Section 2.2 showed the case study in which we adopted the dynamics model to investigate the surface sensitivity of NEAs during a close planetary encounter to the Apophis 2029 Earth encounter event. We implemented a tidal resurfacing model with two stages: dynamics modeling of the entire body to determine time-varying accelerations and surface slope profiles felt by each surface patch during the 6-h-long closest encounter, and DEM modeling to track motions of surface grains in localized patches [2]. Our simulation results indicate that tidal resurfacing, limited to certain localized regions, will likely occur half an hour before perigee and on the scale of 1 per cent of Apophis's entire surface area. This work also indicates that the most likely locations to detect tidal resurfacing are: initially high-sloped regions ($> 30°$) regardless of the encounter orientation of Apophis, and mid-sloped regions ($15°$–$30°$) that experience a significant positive slope variation ($> 0.5°$), which is mainly controlled by the encounter orientation. When we predict the encounter orientation more precisely, the current tidal resurfacing model can provide better predictions on the locations that can actually show strong signals for tidal resurfacing. It is theoretically possible to change Apophis' surface albedos if the tidally induced grain motions indeed occur during the 2029 Earth encounter. Therefore, investigating albedo changes will be crucial to support the tidal resurfacing scenario. Furthermore, images taken by in-situ mission (i.e., OSIRIS-APEX) will provide more detailed information on Apophis' surface properties which can be implemented in our numerical model for better prediction.

- Section 3.3 showed the case study, which numerically investigated the interior layout when the structure of Psyche consists of a spherical iron core and two types of the silicate-rich layers (compressed and uncompressed ones) resulting from the compaction process. The original FEM was extended to be implemented in an inverse problem algorithm to

[1] The currently available asteroid shape models can be checked in these websites (i.e., 3D Asteroid Catalogue, PDS Small Bodies Node, etc.)

[2] As mentioned in the previous sections, the DEM modeling was done by Joe DeMartini at the University of Maryland.

determine the layout distribution by combining a Finite Element Model (FEM) approach that accounts for density variations and constrains pressure-based crushing conditions. The key results addressed that the core size ranged between 78 - 83 km in radius can be compatible with the scenario that the impact cratering process might cause the localized metal concentration at the crater-like region detected in the recent radar observation. This study also indicated that the ferrovolcanic surface eruptions could still be a source of metal-rich materials, given the measured thickness of the silicate-rich layer. We expect the upcoming NASA Psyche mission to obtain detailed data on the gravity field using its loaded X-band radio system. We can consider implementing this data in our advanced model, allowing for more detailed settings on the density distribution of the object. Also, we can use the detailed surface map to better constrain the metal-concentrated regions to explore whether the impact cratering process could be one of contributors to explain metals on the surface.

- Section 3.4 showed the case study, which explored how the bilobated Arrokoth responded to the structural disturbances generated by the sky crater impact and mainly focused on the change in the cohesive strength regime required to keep the current shape under the influence of the sky impact. The original FEM was extended to calculate the time-varying cohesive strength based on viscoelastic deformation. The initial condition of the FEM was given by the impact scaling model that characterized the linear momentum imparted to the small lobe due to the sky impact. The key result of this study is the minimum cohesive strength variation required for Arrokoth to keep the current shape from the sky impact reaches up to sim 15 kPa at the neck in the defined parameter space. This strength variation changes depending on the impact speed or Arrokoth's bulk density, but all simulated cases showed a few kilopascals strength variations. This level of variation seems to be significantly higher than other small bodies, usually less than 1 kPa [200, 199]. This result might indicate that Arrokoth could experience structure disturbances such as the neck breakup in the past. However, it is not rejected that KBOs might have a higher strength regime than other small bodies. The LORRI image is the only available

data to analyze the Arrokoth's surface because no future mission is currently targeting this object. If the Arrokoth's neck was subject to strong structural disruptions, we might find any remaining features on the surface, although it is uncertain to be detectable in the image. Therefore, surface analysis using the Arrokoth LORRI image can be proposed to explore the neck breakup scenario. One noticeable feature in Arrokoth's structure is that the principal axis of the two lobes is slightly misaligned. This feature might also be explainable if the two lobes were previously departed and reattached. By simulating how the two lobes were dynamically locked after the sky impact, we can visit the question of whether the structural disruption due to the sky impact might cause the misaligned feature.

References

[1] Marina Brozović, Lance AM Benner, Joseph G McMichael, Jon D Giorgini, Petr Pravec, Petr Scheirich, Christopher Magri, Michael W Busch, Joseph S Jao, Clement G Lee, et al. Goldstone and arecibo radar observations of (99942) apophis in 2012–2013. *Icarus*, 300:115–128, 2018. 10.1016/j.icarus.2017.08.032.

[2] Ryota Nakano and Masatoshi Hirabayashi. Mass-shedding activities of asteroid (3200) phaethon enhanced by its rotation. *The Astrophysical Journal Letters*, 892(2):L22, 2020.

[3] Steven J Ostro, Petr Pravec, Lance AM Benner, R Scott Hudson, Lenka Sarounova, Michael D Hicks, David L Rabinowitz, James V Scotti, David J Tholen, Marek Wolf, et al. Radar and optical observations of asteroid 1998 ky26. *Science*, 285(5427):557–559, 1999.

[4] Michael K Shepard, Katherine de Kleer, Saverio Cambioni, Patrick A Taylor, Anne K Virkki, Edgard G Rívera-Valentin, Carolina Rodriguez Sanchez-Vahamonde, Luisa Fernanda Zambrano-Marin, Christopher Magri, David Dunham, et al. Asteroid 16 psyche: Shape, features, and global map. *The Planetary Science Journal*, 2(4):125, 2021.

[5] James Baer and Steven R Chesley. Simultaneous mass determination for gravitationally coupled asteroids. *The Astronomical Journal*, 154(2):76, 2017.

[6] LT Elkins-Tanton, E Asphaug, JF Bell III, H Bercovici, B Bills, R Binzel, WF Bottke, S Dibb, DJ Lawrence, S Marchi, et al. Observations, meteorites, and models: a preflight assessment of the composition and formation of (16) psyche. *Journal of Geophysical Research: Planets*, 125(3):e2019JE006296, 2020.

[7] Keith A Holsapple. The scaling of impact processes in planetary sciences. *Annual review of earth and planetary sciences*, 21(1):333–373, 1993.

[8] Masatoshi Hirabayashi, Alexander J Trowbridge, and Dennis Bodewits. The mysterious location of maryland on 2014 mu69 and the reconfiguration of its bilobate shape. *The Astrophysical Journal Letters*, 891(1):L12, 2020.

[9] S Alan Stern, Brian Keeney, Kelsi N Singer, Oliver White, Jason D Hofgartner, Will Grundy, New Horizons Team, et al. Some new results and perspectives regarding the kuiper belt object arrokoth's remarkable, bright neck. *The Planetary Science Journal*, 2(3):87, 2021.

[10] Richard P Binzel, Alessandro Morbidelli, Sihane Merouane, Francesca E DeMeo, Mirel Birlan, Pierre Vernazza, Cristina A Thomas, Andrew S Rivkin, Schelte J Bus, and Alan T Tokunaga. Earth encounters as the origin of fresh surfaces on near-earth asteroids. *Nature*, 463(7279):331, 2010. 10.1038/nature08709.

[11] Clark R Chapman. Space weathering of asteroid surfaces. *Annu. Rev. Earth Planet. Sci.*, 32:539–567, 2004. 10.1146/annurev.earth.32.101802.120453.

[12] Carlé M Pieters, Larry A Taylor, Sarah K Noble, Lindsay P Keller, Bruce Hapke, Richard V Morris, Carl C Allen, David S McKAY, and Susan Wentworth. Space weathering on airless bodies: Resolving a mystery with lunar samples. *Meteoritics & Planetary Science*, 35(5):1101–1107, 2000.

[13] P Vernazza, RP Binzel, CA Thomas, FE DeMeo, SJ Bus, AS Rivkin, and AT Tokunaga. Compositional differences between meteorites and near-earth asteroids. *Nature*, 454(7206):858, 2008. 10.1038/nature07154.

[14] Sho Sasaki, Keiko Nakamura, Yoshimi Hamabe, Erika Kurahashi, and Takahiro Hiroi. Production of iron nanoparticles by laser irradiation in a simulation of lunar-like space weathering. *Nature*, 410(6828):555, 2001. 10.1038/35069013.

[15] Bruce Hapke. Space weathering from mercury to the asteroid belt. *Journal of Geophysical Research: Planets*, 106(E5):10039–10073, 2001. 10.1029/2000JE001338.

[16] Gianni Strazzulla, E Dotto, R Binzel, R Brunetto, MA Barucci, A Blanco, and V Orofino. Spectral alteration of the meteorite epinal (h5) induced by heavy ion irradiation: A simulation of space weathering effects on near-earth asteroids. *Icarus*, 174(1):31–35, 2005. 10.1016/j.icarus.2004.09.013.

[17] William Frederick Bottke. *Asteroids III*. University of Arizona Press, 2002.

[18] David Nesvornỳ, William F Bottke, David Vokrouhlickỳ, Clark R Chapman, and Scot Rafkin. Do planetary encounters reset surfaces of near earth asteroids? *Icarus*, 209(2):510–519, 2010. 10.1016/j.icarus.2010.05.003.

[19] Benoit Carry, Enrique Solano, Siegfried Eggl, and Francesca E DeMeo. Spectral properties of near-earth and mars-crossing asteroids using sloan photometry. *Icarus*, 268:340–354, 2016. 10.1016/j.icarus.2015.12.047.

[20] Francesca E DeMeo, Richard P Binzel, and Matthew Lockhart. Mars encounters cause fresh surfaces on some near-earth asteroids. *Icarus*, 227:112–122, 2014. 10.1016/j.icarus.2013.09.014.

[21] S Marchi, S Magrin, D Nesvornỳ, Paolo Paolicchi, and M Lazzarin. A spectral slope versus perihelion distance correlation for planet-crossing asteroids. *Monthly Notices of the Royal Astronomical Society: Letters*, 368(1):L39–L42, 2006. 10.1111/j.1745-3933.2006.00152.x.

[22] David Nesvornỳ, Robert Jedicke, Robert J Whiteley, and Željko Ivezić. Evidence for asteroid space weathering from the sloan digital sky survey. *Icarus*, 173(1):132–152, 2005. 10.1016/j.icarus.2004.07.026.

[23] Marco Delbo, Guy Libourel, Justin Wilkerson, Naomi Murdoch, Patrick Michel, KT Ramesh, Clément Ganino, Chrystele Verati, and Simone Marchi. Thermal fatigue

as the origin of regolith on small asteroids. *Nature*, 508(7495):233, 2014. 10.1038/nature13153.

[24] Jamie L Molaro, Shane Byrne, and Stephen A Langer. Grain-scale thermoelastic stresses and spatiotemporal temperature gradients on airless bodies, implications for rock breakdown. *Journal of Geophysical Research: Planets*, 120(2):255–277, 2015. 10.1002/2014JE004729.

[25] Jamie L Molaro, Shane Byrne, and J-L Le. Thermally induced stresses in boulders on airless body surfaces, and implications for rock breakdown. *Icarus*, 294:247–261, 2017. 10.1016/j.icarus.2017.03.008.

[26] Kevin J Graves, David A Minton, Masatoshi Hirabayashi, Francesca E DeMeo, and Benoit Carry. Resurfacing asteroids from yorp spin-up and failure. *Icarus*, 304:162–171, 2018. 10.1016/j.icarus.2017.08.025.

[27] Anthony R Dobrovolskis. Tidal disruption of solid bodies. *Icarus*, 88(1):24–38, 1990. 10.1016/0019-1035(90)90175-9.

[28] Derek C Richardson, William F Bottke Jr, and Stanley G Love. Tidal distortion and disruption of earth-crossing asteroids. *Icarus*, 134(1):47–76, 1998. 10.1006/icar.1998.5954.

[29] Ishan Sharma, James T Jenkins, and Joseph A Burns. Tidal encounters of ellipsoidal granular asteroids with planets. *Icarus*, 183(2):312–330, 2006. 10.1016/j.icarus.2006.03.006.

[30] S Sridhar and S Tremaine. Tidal disruption of viscous bodies. *Icarus*, 95(1):86–99, 1992. 0.1016/0019-1035(92)90193-B.

[31] Zdenek Sekanina, Paul W Chodas, and Donald K Yeomans. Tidal disruption and the appearance of periodic comet shoemaker-levy 9. *Astronomy and Astrophysics*, 289:607–636, 1994.

[32] JV Scotti and HJ Melosh. Estimate of the size of comet shoemaker-levy 9 from a tidal breakup model. *Nature*, 365(6448):733, 1993. 10.1038/365733a0.

[33] E. Asphaug and W. Benz. Density of comet Shoemaker–Levy 9 deduced by modelling breakup of the parent 'rubble pile'. *Nature*, 370(6485):120–124, 1994. 10.1038/370120a0.

[34] James T Keane and Isamu Matsuyama. Rejuvenating neos: the efficiency of asteroid resurfacing via planetary flybys. In *AAS/Division for Planetary Sciences Meeting Abstracts# 46*, volume 46, 2014.

[35] J. T. Keane and I. Matsuyama. Rejuvenating asteroids during planetary flybys: Applications to (99942) apophis and other near-earth asteroids. In *46th Lunar and Planetary Science Conference*, page Abstract #2996, Houston, 2015. Lunar and Planetary Institute.

[36] Joseph V DeMartini, Derek C Richardson, Olivier S Barnouin, Nicholas C Schmerr, Jeffrey B Plescia, Petr Scheirich, and Petr Pravec. Using a discrete element method to investigate seismic response and spin change of 99942 apophis during its 2029 tidal encounter with earth. *Icarus*, 328:93–103, 2019. 10.1016/j.icarus.2019.03.015.

[37] DJ Scheeres, LAM Benner, SJ Ostro, A Rossi, F Marzari, and P Washabaugh. Abrupt alteration of asteroid 2004 mn4's spin state during its 2029 earth flyby. *Icarus*, 178(1):281–283, 2005. 10.1016/j.icarus.2005.06.002.

[38] Yang Yu, Derek C Richardson, Patrick Michel, Stephen R Schwartz, and Ronald-Louis Ballouz. Numerical predictions of surface effects during the 2029 close approach of asteroid 99942 apophis. *Icarus*, 242:82–96, 2014. 10.1016/j.icarus.2014.07.027.

[39] Takaaki Noguchi, T Nakamura, M Kimura, ME Zolensky, M Tanaka, T Hashimoto, M Konno, A Nakato, T Ogami, A Fujimura, et al. Incipient space weathering observed on the surface of itokawa dust particles. *Science*, 333(6046):1121–1125, 2011. 10.1126/science.1207794.

[40] Takaaki Noguchi, Makoto Kimura, Takahito Hashimoto, Mitsuru Konno, Tomoki Nakamura, Michael E Zolensky, Ryuji Okazaki, Masahiko Tanaka, Akira Tsuchiyama, Aiko Nakato, et al. Space weathered rims found on the surfaces of the itokawa dust particles. *Meteoritics & Planetary Science*, 49(2):188–214, 2014. 10.1111/maps.12111.

[41] Satoshi Sugita, Rie Honda, Tomokatsu Morota, Shingo Kameda, Hirotaka Sawada, Eisuke Tatsumi, Matsuichi Yamada, Chikatoshi Honda, Yasuhiro Yokota, Toru Kouyama, et al. The geomorphology, color, and thermal properties of ryugu: Implications for parent-body processes. *Science*, 364(6437), 2019.

[42] T Morota, S Sugita, Y Cho, M Kanamaru, E Tatsumi, N Sakatani, R Honda, N Hirata, H Kikuchi, M Yamada, et al. Sample collection from asteroid (162173) ryugu by hayabusa2: Implications for surface evolution. *Science*, 368(6491):654–659, 2020.

[43] C Lantz, RP Binzel, and FE DeMeo. Space weathering trends on carbonaceous asteroids: A possible explanation for bennu's blue slope? *Icarus*, 302:10–17, 2018. 10.1016/j.icarus.2017.11.010.

[44] T William Lambe and Robert V Whitman. *Soil mechanics*. Wiley, New York (553 pp.), 1969. 10.1016/S1631-0748(02)01436-4.

[45] WEH Culling. Analytical theory of erosion. *The Journal of Geology*, 68(3):336–344, 1960. 10.1086/626663.

[46] Joshua J Roering, James W Kirchner, and William E Dietrich. Evidence for nonlinear, diffusive sediment transport on hillslopes and implications for landscape morphology. *Water Resources Research*, 35(3):853–870, 1999. 10.1029/1998WR900090.

[47] Ronald-Louis Ballouz, Nicola Baresi, Sarah T Crites, Yasuhiro Kawakatsu, and Masaki Fujimoto. Surface refreshing of martian moon phobos by orbital eccentricity-driven grain motion. *Nature Geoscience*, 12(4):229, 2019. 10.1038/s41561-019-0323-9.

[48] Christine M Hartzell. Dynamics of 2d electrostatic dust levitation at asteroids. *Icarus*, 333:234–242, 2019. 10.1016/j.icarus.2019.05.013.

[49] Jamie L Molaro, Carl W Hergenrother, Steven Chesley, Romy D Hanna, Christopher W Haberle, Ronald-Louis Ballouz, Stephen R Schwartz, William Bottke, Kevin John Walsh, Humberto Campins, and Dante Lauretta. Thermal fatigue as a driving mechanism for activity on asteroid bennu. *Earth and Space Science Open Archive*, 2019. 10.1002/essoar.10501385.1.

[50] G Tancredi, A Maciel, L Heredia, P Richeri, and S Nesmachnow. Granular physics in low-gravity environments using discrete element method. *Monthly Notices of the Royal Astronomical Society*, 420(4):3368–3380, 2012. 10.1111/j.1365-2966.2011.20259.x.

[51] Tomoya M Yamada and Hiroaki Katsuragi. Scaling of convective velocity in a vertically vibrated granular bed. *Planetary and Space Science*, 100:79–86, 2014. 10.1016/j.pss.2014.05.019.

[52] James E Richardson Jr, H Jay Melosh, Richard J Greenberg, and David P O'Brien. The global effects of impact-induced seismic activity on fractured asteroid surface morphology. *Icarus*, 179(2):325–349, 2005. 10.1016/j.icarus.2005.07.005.

[53] Minami Yasui, Eri Matsumoto, and Masahiko Arakawa. Experimental study on impact-induced seismic wave propagation through granular materials. *Icarus*, 260:320–331, 2015. 10.1016/j.icarus.2015.07.032.

[54] KA Holsapple. Equilibrium configurations of solid cohesionless bodies. *Icarus*, 154(2):432–448, 2001.

[55] Anthony R Dobrovolskis. Inertia of any polyhedron. *Icarus*, 124(2):698–704, 1996. 10.1006/icar.1996.0243.

[56] Akira Fujiwara, J Kawaguchi, DK Yeomans, M Abe, T Mukai, T Okada, J Saito, H Yano, M Yoshikawa, DJ Scheeres, et al. The rubble-pile asteroid itokawa as observed by hayabusa. *Science*, 312(5778):1330–1334, 2006. 10.1126/science.1125841.

[57] WF Bottke, Michael C Nolan, Richard Greenberg, and Robert A Kolvoord. Collisional lifetimes and impact statistics of near-earth asteroids. *Hazards due to comets and asteroids*, 337, 1994.

[58] Petr Pravec, Alan W Harris, and BD Warner. Nea rotations and binaries. *Proceedings of the International Astronomical Union*, 2(S236):167–176, 2006.

[59] Andrew McNeill, Joseph L Hora, Annika Gustafsson, David E Trilling, and Michael Mommert. Constraining the shape distribution of near-earth objects from partial light curves. *The Astronomical Journal*, 157(4):164, 2019.

[60] Konrad Willner, Xian Shi, and Juergen Oberst. Phobos' shape and topography models. *Planetary and Space Science*, 102:51–59, 2014. 10.1016/j.pss.2013.12.006.

[61] DJ Scheeres. Changes in rotational angular momentum due to gravitational interactions between two finite bodies. *Celestial Mechanics and Dynamical Astronomy*, 81(1-2):39–44, 2001. 10.1023/A:1013350918651.

[62] Richard P Binzel, Brent Barbee, Olivier Barnouin, James Bell, Mirel Birlan, Aaron Boley, William Bottke, Marina Brozovic, Joshua Cahill, Humberto Campins, et al. Apophis 2029: Decadal opportunity for the science of planetary defense. *White paper submitted to The Planetary Science and Astrobiology Decadal Survey*, pages 2023–2032, 2020.

[63] D DellaGiustina, DR Golish, S Guzewich, M Moreau, MC Nolan, AT Polit, and AA Simon. Osiris-apex: A proposed osiris-rex extended mission to apophis. In *Apophis T-7 Years: Knowledge Opportunities for the Science of Planetary Defense*, volume 2681 of *LPI Contributions*, page 2011, 2022.

[64] Shinsuke Abe, Tadashi Mukai, Naru Hirata, Olivier S Barnouin-Jha, Andrew F Cheng, Hirohide Demura, Robert W Gaskell, Tatsuaki Hashimoto, Kensuke Hiraoka, Takayuki Honda, et al. Mass and local topography measurements of itokawa by hayabusa. *Science*, 312(5778):1344–1347, 2006.

[65] Yun Zhang and Patrick Michel. Tidal distortion and disruption of rubble-pile bodies revisited-soft-sphere discrete element analyses. *Astronomy & Astrophysics*, 640:A102, 2020.

[66] Richard P Binzel, Andrew S Rivkin, Cristina A Thomas, Pierre Vernazza, Thomas H Burbine, Francesca E DeMeo, Schelte J Bus, Alan T Tokunaga, and Mirel Birlan. Spectral properties and composition of potentially hazardous asteroid (99942) apophis. *Icarus*, 200(2):480–485, 2009.

[67] Davide Farnocchia, Steven R Chesley, Paul W Chodas, M Micheli, DJ Tholen, A Milani, GT Elliott, and F Bernardi. Yarkovsky-driven impact risk analysis for asteroid (99942) apophis. *Icarus*, 224(1):192–200, 2013.

[68] J Souchay, D Souami, C Lhotka, V Puente, and Marta Folgueira. Rotational changes of the asteroid 99942 apophis during the 2029 close encounter with earth. *Astronomy & Astrophysics*, 563:A24, 2014.

[69] Jean Souchay, Ch Lhotka, G Heron, Yann Herve, V Puente, and M Folgueira Lopez. Changes of spin axis and rate of the asteroid (99942) apophis during the 2029 close encounter with earth: A constrained model. *Astronomy & Astrophysics*, 617:A74, 2018.

[70] Conor J Benson, Daniel J Scheeres, Marina Brozović, Steven Chesley, Petr Pravec, and Petr Scheirich. Spin state evolution of (99942) apophis during its 2029 earth encounter. *Icarus*, page 115324, 2022.

[71] Joseph DeMartini and Yaeji Kim. Tidal resurfacing model for (99942) apophis during the 2029 close approach with earth. *AAS/Division for Planetary Sciences Meeting Abstracts*, 53(7):107–04, 2021.

[72] M Hirabayashi, Y Kim, and M Brozović. Finite element modeling to characterize the stress evolution in asteroid (99942) apophis during the 2029 earth encounter. *Icarus*, page 114493, 2021.

[73] Carle M Pieters and Sarah K Noble. Space weathering on airless bodies. *Journal of Geophysical Research: Planets*, 121(10):1865–1884, 2016.

[74] Michelle Thompson, Jessica Barnes, David Blewett, Joshua Cahill, Brett Denevi, Kerri Donaldson Hanna, Jeff Gillis-Davis, Tim Glotch, Devanshu Jha, Georgiana Kramer, et al. Space weathering across the solar system: Lessons from the moon and outstanding questions. *Bulletin of the American Astronomical Society*, 53(4):172, 2021.

[75] Hideaki Miyamoto, Hajime Yano, Daniel J Scheeres, Shinsuke Abe, Olivier Barnouin-Jha, Andrew F Cheng, Hirohide Demura, Robert W Gaskell, Naru Hirata, Masateru Ishiguro, et al. Regolith migration and sorting on asteroid itokawa. *Science*, 316(5827):1011–1014, 2007. 10.1126/science.1134390.

[76] Sunho Jin and Masateru Ishiguro. Estimation of the space weathering timescale on (25143) itokawa: Implications on its rejuvenation process. *Astronomy & Astrophysics*, 667:A93, 2022.

[77] AA Fraeman, SL Murchie, RE Arvidson, RN Clark, RV Morris, AS Rivkin, and F Vilas. Spectral absorptions on phobos and deimos in the visible/near infrared wavelengths and their compositional constraints. *Icarus*, 229:196–205, 2014.

[78] Tomoya M Yamada, Kousuke Ando, Tomokatsu Morota, and Hiroaki Katsuragi. Timescale of asteroid resurfacing by regolith convection resulting from the impact-induced global seismic shaking. *Icarus*, 272:165–177, 2016.

[79] Clark R Chapman. S-type asteroids, ordinary chondrites, and space weathering: The evidence from galileo's fly-bys of gaspra and ida. *Meteoritics & Planetary Science*, 31(6):699–725, 1996.

[80] Yaeji Kim, Masatoshi Hirabayashi, Richard P Binzel, Marina Brozović, Daniel J Scheeres, and Derek C Richardson. The surface sensitivity of rubble-pile asteroids during a distant planetary encounter: Influence of asteroid shape elongation. *Icarus*, 358:114205, 2021.

[81] Clark R Chapman. Near earth asteroid rendezvous: Eros as the key to the s-type conundrum. In *26th Lunar and Planetary Science Conference*, volume 26 of *LPI Contributions*, page 229, 1995.

[82] P Pravec, P Scheirich, J Ďurech, J Pollock, P Kušnirák, K Hornoch, A Galád, D Vokrouhlickỳ, AW Harris, Emmanuel Jehin, et al. The tumbling spin state of (99942) apophis. *Icarus*, 233:48–60, 2014. 10.1016/j.icarus.2014.01.026.

[83] H-J Lee, M-J Kim, A Marciniak, D-H Kim, H-K Moon, Y-J Choi, S Zoła, J Chatelain, TA Lister, E Gomez, et al. Refinement of the convex shape model and tumbling spin state of (99942) apophis using the 2020–2021 apparition data. *Astronomy & Astrophysics*, 661:L3, 2022.

[84] Charles H Acton Jr. Ancillary data services of nasa's navigation and ancillary information facility. *Planetary and Space Science*, 44(1):65–70, 1996.

[85] Charles Acton, Nathaniel Bachman, Boris Semenov, and Edward Wright. A look towards the future in the handling of space science mission geometry. *Planetary and Space Science*, 150:9–12, 2018.

[86] Derek C. Richardson, Thomas Quinn, Joachim Stadel, and George Lake. Direct Large-Scale N-Body Simulations of Planetesimal Dynamics. *Icarus*, 143(1):45–59, 2000.

[87] Joachim Gerhard Stadel. *Cosmological N-body simulations and their analysis*. PhD thesis, University of Washington, Seattle, January 2001.

[88] S. R. Schwartz, D. C. Richardson, and P. Michel. An implementation of the soft-sphere discrete element method in a high-performance parallel gravity tree code. *Granular Matter*, 14:363–380, 2012.

[89] Paul Sánchez and Daniel J. Scheeres. Simulating Asteroid Rubble Piles with A Self-gravitating Soft-sphere Distinct Element Method Model. *The Astrophysical Journal*, 727(2):120, February 2011.

[90] Yun Zhang, Derek C. Richardson, Olivier S. Barnouin, Clara Maurel, Patrick Michel, Stephen R. Schwartz, Ronald-Louis Ballouz, Lance A. M. Benner, Shantanu P. Naidu, and Junfeng Li. Creep stability of the proposed AIDA mission target 65803 Didymos: I. Discrete cohesionless granular physics model. *Icarus*, 294:98–123, September 2017.

[91] Steven Ross Schwartz. *The development and Implementation of numerical tools for investigation into the granular dynamics of solid solar system bodies*. PhD thesis, University of Maryland, College Park, January 2013.

[92] Kevin J Walsh, Ronald-Louis Ballouz, Erica R Jawin, Chrysa Avdellidou, Olivier S Barnouin, Carina A Bennett, Edward B Bierhaus, Brent J Bos, Saverio Cambioni, Harold C Connolly, Marco Delbo, Daniella N DellaGiustina, Joseph DeMartini, Joshua P Emery, Dathon R Golish, Patrick C Haas, Carl W Hergenrother, Huikang Ma, Patrick Michel, Michael C Nolan, Ryan Olds, Benjamin Rozitis, Derek C Richardson, Bashar Rizk, Andrew J Ryan, Paul Sánchez, Daniel J Scheeres, Stephen R Schwartz, Sanford H Selznick, Yun Zhang, and Dante S Lauretta. Near-zero cohesion and loose packing of Bennu’s near subsurface revealed by spacecraft contact. *Science Advances*, 8(27), 2022.

[93] Tatsuhiro Michikami, Akiko M. Nakamura, Naru Hirata, Robert W. Gaskell, Ryosuke Nakamura, Takayuki Honda, Chikatoshi Honda, Kensuke Hiraoka, Jun Saito, Hirohide Demura, Masateru Ishiguro, and Hideaki Miyamoto. Size-frequency statistics of boulders on global surface of asteroid 25143 Itokawa. *Earth, Planets and Space*, 60:13–20, January 2008.

[94] S. Mazrouei, M. G. Daly, O. S. Barnouin, C. M. Ernst, and I. DeSouza. Block distributions on Itokawa. *Icarus*, 229:181–189, February 2014.

[95] James E Richardson and Timothy J Bowling. Investigating the combined effects of shape, density, and rotation on small body surface slopes and erosion rates. *Icarus*, 234:53–65, 2014.

[96] RW Gaskell, OS Barnouin-Jha, Daniel J Scheeres, AS Konopliv, T Mukai, Shinsuke Abe, J Saito, M Ishiguro, Takashi Kubota, T Hashimoto, et al. Characterizing and navigating small bodies with imaging data. *Meteoritics & Planetary Science*, 43(6):1049–1061, 2008.

[97] M Brozović, LAM Benner, SP Naidu, MW Busch, JD Giorgini, J Lazio, and T Hall. Radar observations of 99942 apophis in 2021 and plans for 2029. In *Apophis T-7 Years: Knowledge Opportunities for the Science of Planetary Defense*, volume 2681 of *LPI Contributions*, page 2023, 2022.

[98] Agustín Vallejo, Jorge I Zuluaga, and Germán Chaparro. Conditions for high-resolution bistatic radar observations of apophis in 2029. *Monthly Notices of the Royal Astronomical Society*, 518(3):4438–4448, 2022.

[99] MC Nolan, DR Golish, MC Moreau, AT Polit, EG Rivera-Valentín, AA Simon, and D DellaGiustina. Osiris-apex coordination with observers and missions. In *Apophis T-7 Years: Knowledge Opportunities for the Science of Planetary Defense*, volume 2681 of *LPI Contributions*, page 2004, 2022.

[100] D. S. Lauretta, D. N. Dellagiustina, C. A. Bennett, D. R. Golish, K. J. Becker, S. S. Balram-Knutson, O. S. Barnouin, T. L. Becker, W. F. Bottke, W. V. Boynton, H. Campins, B. E. Clark, H. C. Connolly, C. Y. Drouet D'Aubigny, J. P. Dworkin, J. P. Emery, H. L. Enos, V. E. Hamilton, C. W. Hergenrother, E. S. Howell, M. R. M. Izawa, H. H. Kaplan, M. C. Nolan, B. Rizk, H. L. Roper, D. J. Scheeres, P. H. Smith, K. J. Walsh, C. W. V. Wolner, and Osiris-Rex Team. The unexpected surface of asteroid (101955) Bennu. *Nature*, 568(7750):55–60, March 2019.

[101] Seiichiro Watanabe, M Hirabayashi, N Hirata, Na Hirata, R Noguchi, Y Shimaki, H Ikeda, E Tatsumi, M Yoshikawa, S Kikuchi, et al. Hayabusa2 arrives at the carbonaceous asteroid 162173 ryugu—a spinning top–shaped rubble pile. *Science*, 364(6437):268–272, 2019.

[102] Joseph DeMartini and Derek Richardson. Modeling High-Porosity Regolith on Low-Gravity Planetary Surfaces. In *European Planetary Science Congress*, pages EPSC2022–560, September 2022.

[103] J. C. Marohnic, J. V. DeMartini, and D. C. Richardson. A Numerical Approach to Studying the Effects of Particle Shape on Rubble-Pile Dynamics. In *53rd Lunar and Planetary Science Conference*, volume 2678 of *LPI Contributions*, page 2729, March 2022.

[104] Olivier S. Barnouin-Jha, Andrew F. Cheng, Tadashi Mukai, Shinsuke Abe, Naru Hirata, Ryosuke Nakamura, Robert W. Gaskell, Jun Saito, and Beth E. Clark. Small-scale topography of 25143 Itokawa from the Hayabusa laser altimeter. *Icarus*, 198(1):108–124, November 2008.

[105] Andrew F. Cheng, O. Barnouin-Jha, L. Prockter, M. T. Zuber, G. Neumann, D. E. Smith, J. Garvin, M. Robinson, J. Veverka, and P. Thomas. Small-Scale Topography of 433 Eros from Laser Altimetry and Imaging. *Icarus*, 155(1):51–74, January 2002.

[106] OS Barnouin, ER Jawin, RT Daly, R-L Ballouz, MG Daly, JA Seabrook, P Michel, Y Zhang, CL Johnson, KJ Walsh, et al. Geologic context of the osiris-rex sample site from high-resolution topography and imaging. *The Planetary Science Journal*, 3(4):75, 2022.

[107] Paul Sánchez and Daniel J Scheeres. The strength of regolith and rubble pile asteroids. *Meteoritics & Planetary Science*, 49(5):788–811, 2014.

[108] Thomas JR Hughes. *The finite element method: linear static and dynamic finite element analysis*. Courier Corporation, 2012.

[109] John Tinsley Oden and Junuthula Narasimha Reddy. *An introduction to the mathematical theory of finite elements*. Courier Corporation, 2012.

[110] Claes Johnson. *Numerical solution of partial differential equations by the finite element method*. Courier Corporation, 2012.

[111] Magnus Hestenes and Eduard Stiefel. *Methods of conjugate gradients for solving linear systems*. NBS Washington, DC, 1952.

[112] M Hirabayashi, Y Mimasu, N Sakatani, S Watanabe, Y Tsuda, T Saiki, S Kikuchi, T Kouyama, M Yoshikawa, S Tanaka, et al. Hayabusa2 extended mission: New voyage to rendezvous with a small asteroid rotating with a short period. *Advances in Space Research*, 68(3):1533–1555, 2021.

[113] OS Barnouin, MG Daly, EE Palmer, RW Gaskell, JR Weirich, CL Johnson, MM Al Asad, JH Roberts, ME Perry, HCM Susorney, et al. Shape of (101955) bennu indicative of a rubble pile with internal stiffness. *Nature geoscience*, 12(4):247–252, 2019.

[114] Christophe Geuzaine and Jean-François Remacle. A three-dimensional finite element mesh generator with built-in pre-and post-processing facilities. *International Journal for Numerical Methods in Engineering*, 11:79, 2020.

[115] Wai-Fah Chen and Da-Jian Han. *Plasticity for Structural Engineers (2007, J. Ross Publishing)*. Springer-Verlag, 1988.

[116] William Lambe and Robert Whitman. *Soil Mechanics By Lambe and Whitman.pdf*. Wiley, 1969.

[117] Masatoshi Hirabayashi and Daniel J Scheeres. Rotationally induced failure of irregularly shaped asteroids. *Icarus*, 317:354–364, 2019.

[118] David Polishook, N Moskovitz, Richard P Binzel, B Burt, Francesca E DeMeo, Mary L Hinkle, Matthew Lockhart, Michael Mommert, Michael Person, Audrey Thirouin, et al. A 2 km-size asteroid challenging the rubble-pile spin barrier–a case for cohesion. *Icarus*, 267:243–254, 2016.

[119] Masatoshi Hirabayashi. Failure modes and conditions of a cohesive, spherical body due to yorp spin-up. *Monthly Notices of the Royal Astronomical Society*, 454(2):2249–2257, 2015.

[120] B Zellner, DJ Tholen, and EF Tedesco. The eight-color asteroid survey: Results for 589 minor planets. *Icarus*, 61(3):355–416, 1985.

[121] CR Chapman and MJ Gaffey. Reflectance spectra for 277 asteroids. *Asteroids*, pages 655–687, 1979.

[122] Michael J Gaffey, Jeffrey F Bell, and Dale P Cruikshank. Reflectance spectroscopy and asteroid surface mineralogy. *Journal of Environmental Sciences (China) English Ed*, pages 98–127, 1989.

[123] Michael J Gaffey, Thomas H Burbine, and Richard P Binzel. Asteroid spectroscopy: Progress and perspectives. *Meteoritics*, 28(2):161–187, 1993.

[124] Richard P Binzel, Schelte J Bus, Shui Xu, Jessica Sunshine, Thomas H Burbine, A William Neely, and Robert W Brown. Rotationally resolved spectra of asteroid 16 psyche. *Icarus*, 117(2):443–445, 1995.

[125] David Y Oh, Dan M Goebel, Linda Elkins-Tanton, Carol Polanskey, Peter Lord, Scott Tilley, John S Snyder, Greg Carr, Steve Collins, Gregory Lantoine, et al. Psyche: Journey to a metal world. In *52nd AIAA/SAE/ASEE Joint Propulsion Conference*, page 4541, 2016.

[126] Jijin Yang, Joseph I Goldstein, and Edward RD Scott. Iron meteorite evidence for early formation and catastrophic disruption of protoplanets. *Nature*, 446(7138):888–891, 2007.

[127] Brandon C Johnson, Michael M Sori, and Alexander J Evans. Ferrovolcanism on metal worlds and the origin of pallasites. *Nature Astronomy*, 4(1):41–44, 2020.

[128] Steven J Ostro, Donald B Campbell, and Irwin I Shapiro. Mainbelt asteroids: Dual-polarization radar observations. *Science*, 229(4712):442–446, 1985.

[129] Michael K Shepard, Beth Ellen Clark, Maureen Ockert-Bell, Michael C Nolan, Ellen S Howell, Christopher Magri, Jon D Giorgini, Lance AM Benner, Steven J Ostro, Alan W

Harris, et al. A radar survey of m-and x-class asteroids ii. summary and synthesis. *Icarus*, 208(1):221–237, 2010.

[130] Christopher Magri, Michael C Nolan, Steven J Ostro, and Jon D Giorgini. A radar survey of main-belt asteroids: Arecibo observations of 55 objects during 1999–2003. *Icarus*, 186(1):126–151, 2007.

[131] Joseph R Smyth and Tamsin C Mccormick. Crystallographic data for minerals. *Mineral Physics & Crystallography: A Handbook of Physical Constants*, 2:1–17, 1995.

[132] Benoit Carry. Density of asteroids. *Planetary and Space Science*, 73(1):98–118, 2012.

[133] J Hanuš, Matti Viikinkoski, Franck Marchis, J Ďurech, Mikko Kaasalainen, Marco Delbo, David Herald, Eric Frappa, Tsutomu Hayamizu, S Kerr, et al. Volumes and bulk densities of forty asteroids from adam shape modeling. *Astronomy & Astrophysics*, 601:A114, 2017.

[134] Jack D Drummond, William J Merline, Benoit Carry, Al Conrad, Vishnu Reddy, Peter Tamblyn, Clark R Chapman, Brian L Enke, Imke De Pater, Katherine De Kleer, et al. The triaxial ellipsoid size, density, and rotational pole of asteroid (16) psyche from keck and gemini ao observations 2004–2015. *Icarus*, 305:174–185, 2018.

[135] Matti Viikinkoski, Pierre Vernazza, Josef Hanuš, Hervé Le Coroller, K Tazhenova, Benoît Carry, Michael Marsset, Alexis Drouard, Franck Marchis, Romain Fetick, et al. (16) psyche: A mesosiderite-like asteroid? *Astronomy & Astrophysics*, 619:L3, 2018.

[136] Lauri Siltala and Mikael Granvik. Mass and density of asteroid (16) psyche. *The Astrophysical Journal Letters*, 909(1):L14, 2021.

[137] Fiona Nichols-Fleming, Alexander J Evans, Brandon C Johnson, and Michael M Sori. Porosity evolution in metallic asteroids: Implications for the origin and thermal history of asteroid 16 psyche. *Journal of Geophysical Research: Planets*, page e2021JE007063, 2022.

[138] Erik Asphaug, Craig B Agnor, and Quentin Williams. Hit-and-run planetary collisions. *Nature*, 439(7073):155–160, 2006.

[139] JE Chambers. Late-stage planetary accretion including hit-and-run collisions and fragmentation. *Icarus*, 224(1):43–56, 2013.

[140] Alexandre Emsenhuber, Saverio Cambioni, Erik Asphaug, Travis SJ Gabriel, Stephen R Schwartz, and Roberto Furfaro. Realistic on-the-fly outcomes of planetary collisions. ii. bringing machine learning to n-body simulations. *The Astrophysical Journal*, 891(1):6, 2020.

[141] Michael K Shepard, James Richardson, Patrick A Taylor, Linda A Rodriguez-Ford, Al Conrad, Imke de Pater, Mate Adamkovics, Katherine de Kleer, Jared R Males, Katie M Morzinski, et al. Radar observations and shape model of asteroid 16 psyche. *Icarus*, 281:388–403, 2017.

[142] Marin Ferrais, Pierre Vernazza, Laurent Jorda, Nicolas Rambaux, Josef Hanuš, Benoît Carry, Franck Marchis, Michaël Marsset, Matti Viikinkoski, Miroslav Brož, et al. Asteroid (16) psyche's primordial shape: A possible jacobi ellipsoid. *Astronomy & Astrophysics*, 638:L15, 2020.

[143] Juan A Sanchez, Vishnu Reddy, Michael K Shepard, Cristina Thomas, Edward A Cloutis, Driss Takir, Albert Conrad, Cain Kiddell, and Daniel Applin. Detection of rotational spectral variation on the m-type asteroid (16) psyche. *The Astronomical Journal*, 153(1):29, 2016.

[144] Driss Takir, Vishnu Reddy, Juan A Sanchez, Michael K Shepard, and Joshua P Emery. Detection of water and/or hydroxyl on asteroid (16) psyche. *The Astronomical Journal*, 153(1):31, 2016.

[145] Alexis Matter, Marco Delbo, Benoit Carry, and Sebastiano Ligori. Evidence of a metal-rich surface for the asteroid (16) psyche from interferometric observations in the thermal infrared. *Icarus*, 226(1):419–427, 2013.

[146] Zoe A Landsman, Joshua P Emery, Humberto Campins, Josef Hanuš, Lucy F Lim, and Dale P Cruikshank. Asteroid (16) psyche: Evidence for a silicate regolith from spitzer space telescope spectroscopy. *Icarus*, 304:58–73, 2018.

[147] Katherine de Kleer, Saverio Cambioni, and Michael Shepard. The surface of (16) psyche from thermal emission and polarization mapping. *arXiv preprint arXiv:2105.11372*, 2021.

[148] Donald R Davis, Paolo Farinella, and Francesco Marzari. The missing psyche family: Collisionally eroded or never formed? *Icarus*, 137(1):140–151, 1999.

[149] E Asphaug and A Reufer. Mercury and other iron-rich planetary bodies as relics of inefficient accretion. *Nature Geoscience*, 7(8):564–568, 2014.

[150] Jacob NH Abrahams and Francis Nimmo. Ferrovolcanism: Iron volcanism on metallic asteroids. *Geophysical research letters*, 46(10):5055–5064, 2019.

[151] Paul S Hardersen, Edward A Cloutis, Vishnu Reddy, Thais MOTHÉ-DINIZ, and Joshua P Emery. The m-/x-asteroid menagerie: Results of an nir spectral survey of 45 main-belt asteroids. *Meteoritics & Planetary Science*, 46(12):1910–1938, 2011.

[152] DN DellaGiustina, JP Emery, DR Golish, Benjamin Rozitis, CA Bennett, KN Burke, R-L Ballouz, KJ Becker, PR Christensen, CY Drouet d'Aubigny, et al. Properties of rubble-pile asteroid (101955) bennu from osiris-rex imaging and thermal analysis. *Nature Astronomy*, 3(4):341–351, 2019.

[153] Klaus Keil. Geological history of asteroid 4 vesta: The "smallest terrestrial planet". *Asteroids iii*, 573, 2002.

[154] Dan T Britt, Don Yeomans, Kevin Housen, and G Consolmagno. Asteroid density, porosity, and structure. *Asteroids III*, pages 485–500, 2003.

[155] MM Hagerty, DR Hite, CR Ullrich, and DJ Hagerty. One-dimensional high-pressure compression of granular media. *Journal of Geotechnical Engineering*, 119(1):1–18, 1993.

[156] Jerry A Yamamuro, Paul A Bopp, and Poul V Lade. One-dimensional compression of sands at high pressures. *Journal of geotechnical engineering*, 122(2):147–154, 1996.

[157] Danda Shi, Lin Zheng, Jianfeng Xue, and Jing Sun. Dem modeling of particle breakage in silica sands under one-dimensional compression. *Acta Mechanica Solida Sinica*, 29(1):78–94, 2016.

[158] Yukio Nakata, Yoshinori Kato, Masayuki Hyodo, Adrian FL Hyde, and Hidekazu Murata. One-dimensional compression behaviour of uniformly graded sand related to single particle crushing strength. *Soils and foundations*, 41(2):39–51, 2001.

[159] John M De Souza. Compressibility of sand at high pressure. *MS thesis, Massachusetts Institute of Technology*, pages 63–64, 1958.

[160] Yukio Nakata, Masayuki Hyodo, Adrian FL Hyde, Yoshinori Kato, and Hidekazu Murata. Microscopic particle crushing of sand subjected to high pressure one-dimensional compression. *Soils and foundations*, 41(1):69–82, 2001.

[161] J Hanuš, F Marchis, and J Ďurech. Sizes of main-belt asteroids by combining shape models and keck adaptive optics observations. *Icarus*, 226(1):1045–1057, 2013.

[162] M Kaasalainen, J Torppa, and J Piironen. Models of twenty asteroids from photometric data. *Icarus*, 159(2):369–395, 2002.

[163] Masatoshi Hirabayashi, Bryan A Howl, Caleb I Fassett, Jason M Soderblom, David A Minton, and HJ Melosh. The role of breccia lenses in regolith generation from the formation of small, simple craters: Application to the apollo 15 landing site. *Journal of Geophysical Research: Planets*, 123(2):527–543, 2018.

[164] Josef Ďurech, Mikko Kaasalainen, David Herald, David Dunham, Brad Timerson, Josef Hanuš, Eric Frappa, John Talbot, Tsutomu Hayamizu, Brian D Warner, et al. Combining asteroid models derived by lightcurve inversion with asteroidal occultation silhouettes. *Icarus*, 214(2):652–670, 2011.

[165] Alan W Harris. Tumbling asteroids. *Icarus*, 107(1):209–211, 1994.

[166] Daniel T Britt and GJSJ Consolmagno. Stony meteorite porosities and densities: A review of the data through 2001. *Meteoritics & Planetary Science*, 38(8):1161–1180, 2003.

[167] GJ Consolmagno, DT Britt, and RJ Macke. The significance of meteorite density and porosity. *Geochemistry*, 68(1):1–29, 2008.

[168] Edward P Henderson and Stuart H Perry. A discussion of the densities of iron meteorites. *Geochimica et Cosmochimica Acta*, 6(5-6):221–240, 1954.

[169] Mark A Wieczorek, Gregory A Neumann, Francis Nimmo, Walter S Kiefer, G Jeffrey Taylor, H Jay Melosh, Roger J Phillips, Sean C Solomon, Jeffrey C Andrews-Hanna, Sami W Asmar, et al. The crust of the moon as seen by grail. *Science*, 339(6120):671–675, 2013.

[170] Sarah L Wilkison and Mark S Robinson. Bulk density of ordinary chondrite meteorites and implications for asteroidal internal structure. *Meteoritics & Planetary Science*, 35(6):1203–1213, 2000.

[171] A Scheinberg, LT Elkins-Tanton, G Schubert, and D Bercovici. Core solidification and dynamo evolution in a mantle-stripped planetesimal. *Journal of Geophysical Research: Planets*, 121(1):2–20, 2016.

[172] Joseph Veverka, M Robinson, P Thomas, S Murchie, JF Bell III, N Izenberg, C Chapman, A Harch, M Bell, B Carcich, et al. Near at eros: Imaging and spectral results. *Science*, 289(5487):2088–2097, 2000.

[173] Sarah L Wilkison, Mark S Robinson, Peter C Thomas, Joseph Veverka, Timothy J McCoy, Scott L Murchie, Louise M Prockter, and Donald K Yeomans. An estimate of eros's porosity and implications for internal structure. *Icarus*, 155(1):94–103, 2002.

[174] Shin-Chan Han, Nicholas Schmerr, Gregory Neumann, and Simon Holmes. Global characteristics of porosity and density stratification within the lunar crust from grail

gravity and lunar orbiter laser altimeter topography data. *Geophysical Research Letters*, 41(6):1882–1889, 2014.

[175] Hang Si. Tetgen, a delaunay-based quality tetrahedral mesh generator. *ACM Trans. Math. Softw.*, 41(2), feb 2015.

[176] H Jay Melosh. Impact cratering: A geologic process. *icgp*, 1989.

[177] Robert J Macke, Guy J Consolmagno, Daniel T Britt, and Melinda L Hutson. Enstatite chondrite density, magnetic susceptibility, and porosity. *Meteoritics & Planetary Science*, 45(9):1513–1526, 2010.

[178] Bevan M French. *Traces of catastrophe: A handbook of shock-metamorphic effects in terrestrial meteorite impact structures*. Lunar and Planetary Institute, 1998.

[179] JA Jacobs. The earth's inner core. *Nature*, 172(4372):297–298, 1953.

[180] Henning Haack and Edward RD Scott. Asteroid core crystallization by inward dendritic growth. *Journal of Geophysical Research: Planets*, 97(E9):14727–14734, 1992.

[181] Jonathan Besserer, Francis Nimmo, Mark A Wieczorek, Renee C Weber, Walter S Kiefer, Patrick J McGovern, Jeffrey C Andrews-Hanna, David E Smith, and Maria T Zuber. Grail gravity constraints on the vertical and lateral density structure of the lunar crust. *Geophysical Research Letters*, 41(16):5771–5777, 2014.

[182] Konstantin Batygin, Michael E Brown, and Wesley C Fraser. Retention of a primordial cold classical kuiper belt in an instability-driven model of solar system formation. *The Astrophysical Journal*, 738(1):13, 2011.

[183] WB McKinnon, DC Richardson, JC Marohnic, JT Keane, WM Grundy, DP Hamilton, D Nesvornỳ, OM Umurhan, TR Lauer, KN Singer, et al. The solar nebula origin of (486958) arrokoth, a primordial contact binary in the kuiper belt. *Science*, 367(6481):eaay6620, 2020.

[184] JR Spencer, SA Stern, JM Moore, HA Weaver, KN Singer, CB Olkin, AJ Verbiscer, WB McKinnon, J Wm Parker, RA Beyer, et al. The geology and geophysics of kuiper belt object (486958) arrokoth. *Science*, 367(6481):eaay3999, 2020.

[185] WM Grundy, MK Bird, DT Britt, JC Cook, DP Cruikshank, CJA Howett, S Krijt, IR Linscott, CB Olkin, AH Parker, et al. Color, composition, and thermal environment of kuiper belt object (486958) arrokoth. *Science*, 367(6481):eaay3705, 2020.

[186] James T Keane, Simon B Porter, Ross A Beyer, Orkan M Umurhan, William B McKinnon, Jeffrey M Moore, John R Spencer, S Alan Stern, Carver J Bierson, Richard P Binzel, et al. The geophysical environment of (486958) arrokoth—a small kuiper belt object explored by new horizons. *Journal of Geophysical Research. Planets*, 127(6):Art–No, 2022.

[187] Julian C Marohnic, Derek C Richardson, William B McKinnon, Harrison F Agrusa, Joseph V DeMartini, Andrew F Cheng, S Alan Stern, Cathy B Olkin, Harold A Weaver, John R Spencer, et al. Constraining the final merger of contact binary (486958) arrokoth with soft-sphere discrete element simulations. *Icarus*, 356:113824, 2021.

[188] Paul Schenk, Kelsi Singer, Ross Beyer, Chloe Beddingfield, Stuart J Robbins, William B McKinnon, Tod R Lauer, Anne J Verbiscer, James T Keane, Rajani D Dhingra, et al. Origins of pits and troughs and degradation on a small primitive planetesimal in the kuiper belt: high-resolution topography of (486958) arrokoth (aka 2014 mu69) from new horizons. *Icarus*, 356:113834, 2021.

[189] Sarah Greenstreet, Brett Gladman, William B McKinnon, JJ Kavelaars, and Kelsi N Singer. Crater density predictions for new horizons flyby target 2014 mu69. *The Astrophysical Journal Letters*, 872(1):L5, 2019.

[190] William B McKinnon, Xiaochen Mao, PM Schenk, KN Singer, SJ Robbins, OL White, RA Beyer, SB Porter, JT Keane, DT Britt, et al. Snow crash: Compaction craters on (486958) arrokoth and other small kbos, with implications. *Geophysical Research Letters*, 49(13):e2022GL098406, 2022.

[191] Yaeji Kim and Masatoshi Hirabayashi. A numerical approach using a finite element model to constrain the possible interior layout of (16) psyche. *The Planetary Science Journal*, 3(5):122, 2022.

[192] Marc André Meyers and Krishan Kumar Chawla. *Mechanical behavior of materials*. Cambridge university press, 2008.

[193] Diedrich Möhlmann, Klaus J Seidensticker, Hans-Herbert Fischer, Claudia Faber, Alberto Flandes, Martin Knapmeyer, Harald Krüger, Reinhard Roll, Frank Scholten, Klaus Thiel, et al. Compressive strength and elastic modulus at agilkia on comet 67p/churyumov-gerasimenko derived from the sesame/casse touchdown signals. *Icarus*, 303:251–264, 2018.

[194] M Hirabayashi. Dynamics of a deforming planetary body. *Icarus*, 389:115258, 2023.

[195] Paul R Weissman, Anthony R Dobrovolskis, and S Alan Stern. Constraints on impact rates in the pluto-charon system and the population of the kuiper comet belt. *Geophysical Research Letters*, 16(11):1241–1244, 1989.

[196] SA Stern, HA Weaver, AJ Steffl, MJ Mutchler, WJ Merline, MW Buie, EF Young, LA Young, and JR Spencer. A giant impact origin for pluto's small moons and satellite multiplicity in the kuiper belt. *Nature*, 439(7079):946–948, 2006.

[197] Si Hang. Tetgen, a delaunay-based quality tetrahedral mesh generator. *ACM Trans. Math. Softw*, 41(2):11, 2015.

[198] Paolo Cignoni, Marco Callieri, Massimiliano Corsini, Matteo Dellepiane, Fabio Ganovelli, Guido Ranzuglia, et al. Meshlab: an open-source mesh processing tool. In *Eurographics Italian chapter conference*, volume 2008, pages 129–136. Salerno, Italy, 2008.

[199] Angela M Stickle, Mallory E DeCoster, Christoph Burger, Wendy K Caldwell, Dawn Graninger, Kathryn M Kumamoto, Robert Luther, Jens Ormö, Sabina Raducan, Emma Rainey, et al. Effects of impact and target parameters on the results of a kinetic impactor:

predictions for the double asteroid redirection test (dart) mission. *The Planetary Science Journal*, 3(11):248, 2022.

[200] Masahiko Arakawa, T Saiki, K Wada, K Ogawa, T Kadono, K Shirai, H Sawada, K Ishibashi, R Honda, N Sakatani, et al. An artificial impact on the asteroid (162173) ryugu formed a crater in the gravity-dominated regime. *Science*, 368(6486):67–71, 2020.